Large-Eddy Simulation of Premixed Turbulent Combustion Using Flame Surface Density Approach

by

Wen Lin

A thesis submitted in conformity with the requirements
for the degree of Doctor of Philosophy
Graduate Department of Aerospace Science and Engineering
University of Toronto

Abstract

Large-Eddy Simulation of Premixed Turbulent Combustion Using Flame Surface Density Approach

Wen Lin

Doctor of Philosophy

Graduate Department of Aerospace Science and Engineering

University of Toronto

2010

In the last 10-15 years, large-eddy simulation (LES) has become well established for non-reacting flows, and several successful models have been developed for the transfer of momentum and kinetic energy to the subfilter-scales (SFS). However, for reacting flows, LES is still undergoing significant development. In particular, for many premixed combustion applications, the chemical reactions are confined to propagating surfaces that are significantly thinner than the computational grids used in practical LES. In these situations, the chemical kinetics and its interaction with the turbulence are not resolved and must be entirely modelled. There is, therefore, a need for accurate and robust physical modelling of combustion at the subfilter-scales. In this thesis, modelled transport equations for progress variable and flame surface density (FSD) were implemented and coupled to the Favre-filtered Navier-Stokes equations for a compressible reactive thermally perfect mixture. In order to reduce the computational costs and increase the resolution of simulating combusting flows, a parallel adaptive mesh (AMR) refinement finite-volume algorithm was extended and used for the prediction of turbulent premixed flames. The proposed LES methodology was applied to the numerical solution of freely propagating flames in decaying isotropic turbulent flow and Bunsen-type flames. Results for both stoichiometric and lean flames are presented. Comparisons are made between turbulent flame structure predictions for methane, propane, hydrogen fuels, and other available numerical results and experimental data. Details of subfilter-scale modelling, numerical solution scheme, computational results, and capabilities of the methodology for predicting premixed combustion processes are included in the discussions. The current study

represents the first application of a full transport equation model for the FSD to LES of a laboratory-scale turbulent premixed flame. The comparisons of the LES results of this thesis to the experimental data provide strong support for the validity of the modelled transport equation for the FSD. While the LES predictions of turbulent burning rate are seemingly correct for flames lying within the wrinkled and corrugated flamelet regimes and for lower turbulence intensities, the findings cast doubt on the validity of the flamelet approximation for flames within the thin reaction zones regime.

Contents

List of Tables

List of Figures

List of Symbols

Alphanumeric

a	speed of sound
a_{m}	averaged speed of sound
A	cross section area
$A_{i,j}$	area of cell i, j
A_l	surface area of face l
A_{T}	total flame surface area
$A(\bar{c})$	flame zone area
$A(u, v, t)$	elemental area factor
A_Δ	total flame surface area in the given box size Δ
$\mathbf{A}_{\mathrm{I}}$	inviscid flux Jacobian matrix in x-direction
$\mathbf{A}_{\mathrm{V}}$	viscous flux Jacobian matrix in x-direction
$\mathbf{B}_{\mathrm{I}}$	inviscid flux Jacobian matrix in y-direction
$\mathbf{B}_{\mathrm{V}}$	viscous flux Jacobian matrix in y-direction
c	progress variable
c^*	progress variable defining flame surface
C_I	Yoshizawa constant
C_{p}	specific heat at constant pressure
C_s	Smagorinsky constant
C_{v}	specific heat at constant volume
C_ϵ	dissipation constant for one-equation model

Alphanumeric

C_ν	model constant for subfilter-scale eddy viscosity based on subfilter kinetic energy
$\mathrm{C_{res}}$	resolved curvature
$\mathrm{C_{sfs}}$	subfilter-scale curvature
$\mathbf{C_I}$	inviscid flux Jacobian matrix in z-direction
$\mathbf{C_V}$	viscous flux Jacobian matrix in z-direction
d	nozzle diameter of Bunsen-type burner
D	molecule diffusivity
Da	Damköhler number
D_n	molecular diffusivity of species n
e	Favre-averaged total specific mixture energy
E_F	efficiency factor
$\mathbf{f}$	numerical flux
f_a	scaling factor
F	thickening factor
Δ	LES filter
$\mathbf{e}_s$	unity vector
$\mathbf{F}$	spatial filter function
$\mathbf{F_I}$	inviscid x flux in vector notation in three-dimensional coordinate system
$\vec{\mathbf{F}}$	flux dyad
$\mathbf{F_v}$	viscous x flux in vector notation in three-dimensional coordinate system
G	level surface of scalar field
G_0	iso-level surface of scalar field
$\mathbf{G_I}$	inviscid y flux in vector notation in three-dimensional coordinate system
$\mathbf{G_v}$	viscous y flux in vector notation in three-dimensional coordinate system
G_n	Gibbs free energy for species n
h	local curvature
h_n	absolute internal enthalpy for species n
h_s	sensible enthalpy
$\Delta h^o_{\mathrm{f},n}$	heat of formation
$\mathbf{H_I}$	inviscid z flux in vector notation in three-dimensional coordinate system
$\mathbf{H_v}$	viscous z flux in vector notation in three-dimensional coordinate system
I_0	stretch factor
$\mathcal{J}$	species diffusive flux

Alphanumeric

k	turbulent kinetic energy
Ka	Karlovitz number
K_p	coefficient for pressure diffusion term
K_u	coefficient for velocity diffusion term
K_Σ	algebraic model constant for FSD
L	computational domain size
$L(\bar{c})$	flame front length
$\mathrm{L_p}$	left primitive eigenvector matrix
$\mathcal{L}_{ij}$	Germano identity
m	degree of polynomial function
	number of conservation laws
$\dot{m}$	mass flux
M	Mach number
$\mathcal{M}$	split Mach number
M_0	reference Mach number
M_p	pressure diffusive term
M_x	cell number in x-direction
M_y	cell number in y-direction
M_z	cell number in z-direction
n	degree of polynomial function
$\mathbf{n}$	normal vector to the flame
$\vec{n}$	unit vector normal to the cell face or edge
n_{ij}	model for flamelet orientation tensor
N	flame normal in x-direction
N_i	local flame normal in i-direction
N_j	local flame normal in j-direction
N_k	local flame normal in k-direction
N_s	total number of species
N_f	number of cell faces
N	local flame normal direction
$\mathcal{N}_i$	molecular mass of species i
p	time-averaged mixture pressure
p_u	velocity diffusion term
$\mathcal{P}$	polynomial function
$\mathrm{P_{res}}$	resolved propagation term
$\mathrm{Pr_t}$	turbulent Prandtl number
$\mathrm{P_{sfs}}$	subfilter propagation term
q	molecular heat flux vector
q_t	turbulent heat flux vector
$\mathcal{Q}_{ij}$	test-filtered stresses

Alphanumeric

R	ideal gas constant
$\mathrm{R_c}$	right conservative eigenvector matrix
$\mathbf{R}$	discrete residual operator
$\mathcal{R}$	solution of the Riemann problem
$\mathrm{Re_{sfs}}$	subfilter Reynolds number
$\mathrm{Re_\Lambda}$	turbulent Reynolds number
s	flame contour length
s_L	laminar flame speed
s_T	turbulent burning rate
s_Tsfs	subfilter turbulent burning rate
$\check{S}_{ij}$	strain rate tensor
$\lvert\check{S}\rvert$	magnitude of strain rate
$\mathrm{S_{hr}}$	heat release term
$\mathrm{S_{res}}$	resolved strain term
$\mathrm{S_{sfs}}$	subfilter strain term
S_Σ	source terms in FSD transport equation
S_k	source terms in subfilter kinetic transport equation
$\mathbf{S}$	source term in vector notation
$\mathrm{Sc_t}$	turbulent Schmidt number
t	time
T	Favre-averaged temperature
T_ad	adiabatic temperature
T_b	products temperature
T_u	reactants temperature
u	Favre-averaged mixture velocity in x-direction
u'	root mean square velocity fluctuation
u_p	propagating speed
u'_sfs	subfilter fluctuation velocity
u_η	Kolmogorov velocity scale
U	mean flow velocity
$\mathbf{U}$	flow conservative solution variables in vector notation
v	Favre-averaged mixture velocity in y-direction
V	control volume
$V_\mathrm{i,j,k}$	volume of cell i, j, k
w	Favre-averaged mixture velocity in z-direction
$\dot{w}$	mean reaction rate
$\mathbf{W}$	flow primitive solution variables in vector notation
$\mathrm{X}[u, v, t]$	flame surface point
x, y, z	rectangular Cartesian coordinates
x^*	position coordinate

Alphanumeric

Y_{F}	local fuel mass fractions
$Y_{\mathrm{F}}^{\mathrm{b}}$	burnt fuel mass fractions
$Y_{\mathrm{F}}^{\mathrm{u}}$	unburnt fuel mass fractions
Y_n	species mass fraction

Greek

α	model constant
	flame orientation or resolution factor in FSD model
	AUSM scheme parameter
	weighting factor
	scaling factor
α_i	wave-strengths
α_{T}	flame stretch due to fluid flow
β	model constant in FSD model
	AUSM scheme parameter
	scaling factor
δ_{L}	laminar flame thickness
δ, δ_{ij}	Kronecker Delta
Δ	filter width
η	Kolmogorov length scale
	computational coordinate
ϵ	dissipation rate
	refinement criteria
γ	heat capacity ratio
Γ	efficiency function
Γ_{k}	ITNFS model efficiency function
λ	Taylor micro length scale
λ_i	eigenvalue
$\lvert\lambda_k\rvert$	averaged eigenvalue
κ	mixture thermal conductivity
μ	mixture dynamic viscosity
Ω_{ij}	vorticity tensor
ν	mixture kinematic viscosity
ν_{t}	turbulence eddy viscosity
ϕ	equivalence ratio
Ψ	state vector
Φ	vector of slope limiter
$\mathbf{\Phi}$	state vector

Greek

ρ	time-averaged mixture density
ρ_r	reactants density
ρ_u	unburnt mixture density
σ_{ij}	subfilter stresses
σ_p	AUSM scheme parameter
Σ	flame surface density
Σ_sfs	subfilter flame surface density
τ	heat release parameter
τ_c	chemical time scale
τ_{ij}	viscous stress tensor
τ_t	turbulent time scale
τ_η	Kolmogorov time scale
φ	quantity variable
ϑ	heat flux
ξ, η, ζ	computational coordinates
Λ	integral length scale
Ξ	wrinkling factor
Ξ_sfs	subfilter wrinkling factor

Accents

$\bar{x}$	LES filtered value of x
x'	subfiltered fluctuation of x, or root mean square fluctutation
$\tilde{x}$	Favre-filtered LES value of x
$\hat{x}$	test-level filtered value of x, or Roe's approximation variable and function
$\check{x}$	evaluated value of x from resolved and filtered variables
$\dot{x}$	derivative of x
X	vector
$\mathbf{X}$	mathematical vector
$\vec{\mathrm{X}}$	physical vector
$\vec{\mathbf{X}}$	dyad

Acronyms

AMR	Adaptive Mesh Refinement
AUSM$^+$-up	Advection Upstream Splitting Method
BML	Bray-Moss-Libby
CFD	Computational Fluid Dynamics

Acronyms

CFL	Courant-Friedrichs-Lewy
CFM	Coherent Flame Model
DES	Detached Eddy Simulation
DNS	Direct Numerical Simulation
EBU	Eddy Break-Up
FSD	Flame Surface Density
HLLE	Harten-Lax-van-Leer-Einfeldt
ITNFS	Intermittent Turbulence Net Flame Stretch
KPP	Kolmogorov-Petrovski-Piskunov
LEM	Linear Eddy Model
LES	Large Eddy Simulation
LHS	Left Hand Side
NGT	Non-Gradient-Transport
NKS	Newton-Krylov-Schwarz
ODE	Ordinary Differential Equation
PDF	Probability Density Function
RANS	Reynolds Averaged Navier-Stokes
RHS	Right Hand Side
SDS	Semi-Deterministic Simulation
SFS	Subfilter-Scale

Chapter 1

Introduction

In the field of combustion science and engineering, scientific computing is now truly competitive with experiment and theory as a research tool to produce detailed and multi-scale information about combustion processes that is not readily available by using the other techniques. In particular, combustion modelling is an essential tool for providing a better understanding of the physical mechanisms which are key to improving the performance and reducing the environmental impact of combustion systems, such as engines and power plants.

In technical processes, combustion usually takes place within the turbulent rather than the laminar flow regime, as the turbulence increases the mixing processes in non-premixed systems and the surface area in premixed systems leading to enhanced combustion. Moreover, combustion releases heat and generates flow instability, which enhances the transition to fully turbulent flow. In order to simulate turbulent combustion processes, the various coupling mechanisms that exist between the turbulence and the chemical kinetics must be investigated and correctly modelled. Turbulent combustion modelling is a growing field of importance bringing important improvements to our understanding of combustion, and the development of combustion models is a pacing item in this regard.

This chapter begins by first giving an overview of turbulent combustion modelling, followed by a description of the flamelet regime in premixed turbulent combustion. Section 1.1.5 provides a brief overview of different numerical approaches for predicting

turbulent combusting flows as well as a more detailed discussion of large-eddy simulation of premixed turbulent combustion. The final sections of this chapter provide statements of the motivation, the objectives, and an outline of the thesis.

1.1 Turbulent Combustion Modelling

1.1.1 Overview of Turbulent Combustion Modelling

Combustion generally involves the burning of a fuel and oxidizer to produce heat. Flames can be classified depending on the way the reactants are introduced in the combustion zone. The two limiting cases are perfectly premixed and non-premixed flames. In premixed combustion, the reactants (fuel and oxidizer) are perfectly mixed at the molecular level before entering the reaction zone. Since there is no more mixing required, this situation is favorable in terms of burning efficiency, but on the other hand, there is a risk that the flames will propagate in the premixed reactants upstream of the burner and cause damage to the combustor and/or engine. Flame stability, extinction, and flash back are issues of concern.

In non-premixed combustion, the reactants are introduced separately into the combustion chamber and the mixing of the reactants, controlled by convection, molecular diffusion and turbulent transport, limits the reaction rate. Because of the different characteristics of these flames, most models for describing turbulent combustion have been developed specifically for one of these two limiting cases. Fewer others can describe both as well as the intermediate situation of partially premixed combustion. In the present work, premixed combustion is of primary interest and is investigated by numerical methods.

1.1.2 Laminar Premixed Flame Structure

In order to fully understand the possible flow regimes for premixed combustion which will be discussed in more detail in the sections to follows, it is important to first briefly review the structure of premixed laminar flames. The structure of

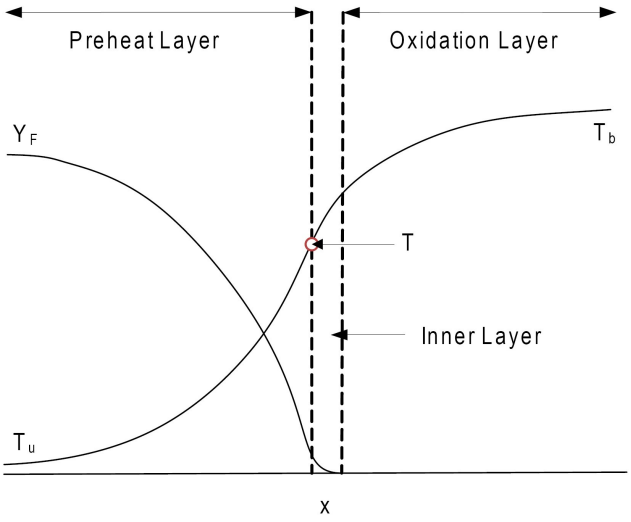

Figure 1.1: Illustration of the structure of a premixed laminar flame as proposed by Peters [1].

laminar premixed flame fronts as first proposed by Mallard and Le Chatelier and later developed by Peters [1] is shown in Figure 1.1. It consists of three rather distinct and different layers: (i) a preheat layer in which the reaction rates are relatively low; (ii) an inner layer with significant on-going chemical reactions and heat release; and finally (iii) an oxidation layer in which the oxidation of radicals formed in the inner layer is completed [1,7]. The flame front has finite thickness and speed and separates the unburnt fresh gases (a mixture of fuel and oxidizer) from the burnt hot gases (a mixture of the hot products of the chemical reactions). The temperature of the gaseous mixture increases across the flame front while the mixture density decreases such that the pressure of the mixture remains nearly constant across the flame. The laminar flame thickness and propagation speed of the flame front are generally defined by the reaction rates and coefficients of thermal and mass diffusion.

1.1.3 Flamelet Regime in Premixed Turbulent Combustion

The different regimes of turbulent combustion can be summarized on a phase diagram as a function of several key non-dimensional parameters. Diagrams defining combustion regimes in terms of the representative length and velocity scales have been

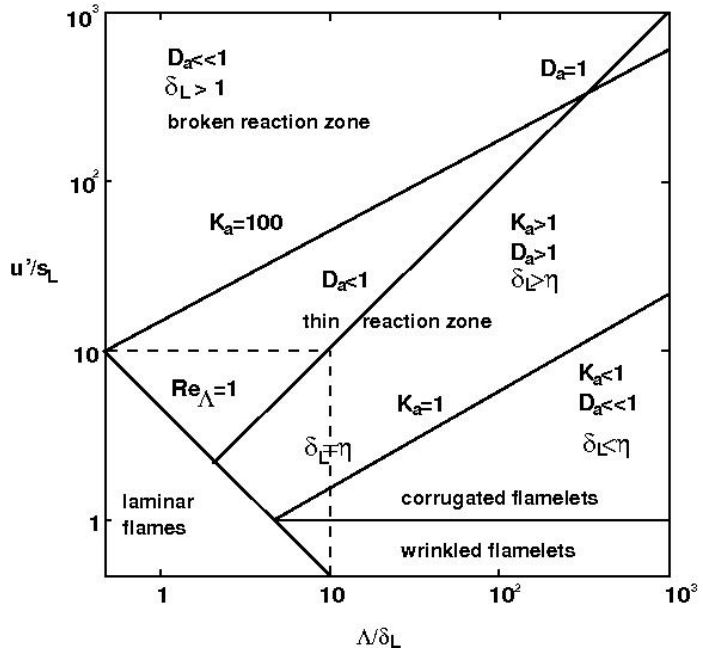

Figure 1.2: Regime diagram for premixed turbulent combustion as proposed by Peters [1].

proposed by Barrère [8], Bray [9], Borghi [2], Peters [10], Williams [11], Abdel-Gayed and Bradley [12], Borghi and Destraiu [2], Peters [13], Pitsch and Duchamp [14], and Düsing *et al.* [15]. For the purpose of this discussion, the modified diagram proposed by Peters [1] will be considered as shown in Figure 1.2.

The nature of the premixed combustion process strongly depends on the length and time scales in the flame front and in the turbulent flow field. The turbulent and chemical time scales can be defined as follows:

$$\tau_\mathrm{t} \approx \frac{\Lambda}{u'}, \qquad \tau_\mathrm{c} \approx \frac{\delta_\mathrm{L}}{s_\mathrm{L}}, \tag{1.1}$$

where Λ, u', δ_L, and s_L are the integral length scale, the root mean square (RMS) velocity fluctuation, the laminar flame thickness, and the laminar flame speed. The root mean square velocity fluctuation, u', and integral length scale, Λ, can be related to the turbulent kinetic energy, k, and its dissipation rate, ϵ, in the following manner

$$u' \approx \sqrt{k}, \qquad \Lambda \approx \frac{u'^3}{\epsilon}, \tag{1.2}$$

with $\tau_t = k/\epsilon$. The Kolmogorov length, time, and velocity scales which represent the smallest scales in the turbulent flow are defined in terms of kinematic viscosity, ν, and turbulent dissipation rate, ϵ,

$$\eta \approx \left(\frac{\nu^3}{\epsilon}\right)^{1/4}, \qquad \tau_\eta \approx \left(\frac{\nu}{\epsilon}\right)^{1/2}, \qquad u_\eta \approx (\nu\epsilon)^{1/4}. \tag{1.3}$$

The thickness of a laminar premixed flame depends on the ratio of the diffusivity D to the laminar flame speed s_L, $\delta_L \approx D/s_L$, under the assumption that the Schmidt number has a value of unity, $\mathrm{Sc} = \nu/D = 1$, the turbulent Reynolds number, which compares the turbulent transport with viscous forces, can be written as

$$\mathrm{Re}_\Lambda = \frac{u'\Lambda}{\nu} = \frac{u'\Lambda}{s_L\delta_L}. \tag{1.4}$$

Classical scaling arguments introduce two-dimensionless numbers corresponding to the limiting values of the turbulence eddies size (from integral length scale Λ to Kolmogorov scale η). They are:

- The Damköhler number, Da, is defined in terms of the largest eddies and corresponds to the ratio of the turbulence time scale, τ_t, to the chemical time scale, τ_c, and given by
$$\mathrm{Da} = \frac{\tau_t}{\tau_c} \approx \frac{\Lambda/u'}{\delta_L/s_L}. \tag{1.5}$$
- The Karlovitz number, Ka, is defined in terms of the smallest eddies of Kolmogorov scale and is the ratio of the chemical time scale to Kolmogorov time scale given by
$$\mathrm{Ka} = \frac{\tau_c}{\tau_\eta} \approx \left(\frac{\delta_L}{\eta}\right)^2 \approx \left(\frac{u_\eta}{s_L}\right)^2, \tag{1.6}$$
with
$$\tau_\eta \approx \left(\frac{\eta}{\nu}\right)^2 \approx \sqrt{\frac{\nu}{\epsilon}}, \qquad s_L \approx \frac{\nu}{\delta_L}, \qquad u_\eta^2 \approx (\nu\epsilon)^{1/2}.$$

The Kolmogorov scale, rather than the integral length scale, is the key length scale because the interaction between chemistry and turbulence occurs mainly at the smallest scales.

The turbulent regime diagram can be plotted as a function of the length, Λ/δ_L, and velocity, u'/s_L, ratios using logarithmic scales for each axes as shown in Figure 1.2.

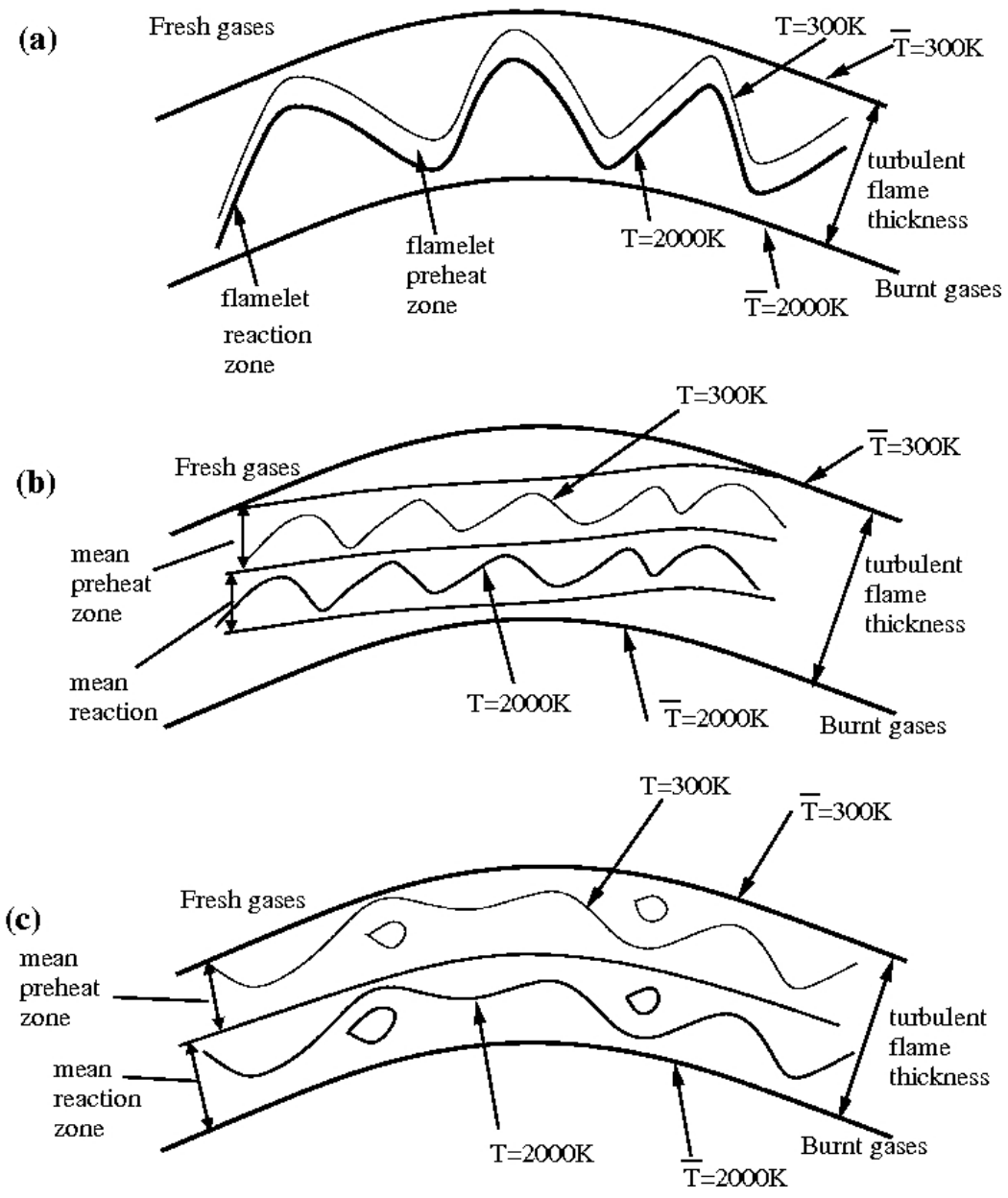

Figure 1.3: Turbulent premixed combustion regimes proposed by Borghi and Destriau [2] illustrated in a case where the fresh and burnt gas temperature are 300K and 2000K, respectively: (a) wrinkled flamelet, (b) thin reaction zone, (c) broken reaction zone, T denotes the instantaneous temperature and $\bar{T}$ denotes the mean temperature.

The lines of constant Reynolds, Damköhler and Karlovitz numbers can be easily constructed in the diagram based on the following relations between the characteristic scales:

$$\frac{u'}{s_{\mathrm{L}}} = \mathrm{Ka}^{2/3}\Big(\frac{\Lambda}{\delta_{\mathrm{L}}}\Big)^{1/3} = \mathrm{Re}_{\Lambda}\Big(\frac{\Lambda}{\delta_{\mathrm{L}}}\Big)^{-1} = \mathrm{Da}^{-1}\Big(\frac{\Lambda}{\delta_{\mathrm{L}}}\Big). \tag{1.7}$$

Five different combustion regimes may be identified in terms of the length scale ratio, $\Lambda/\delta_{\mathrm{L}}$, and velocity scale ratio, u'/s_{L}. They are as follows:

- Laminar flame regime: $\mathrm{Re}_{\Lambda} < 1$. The line $\mathrm{Re}_{\Lambda} = 1$ separates the laminar flame regime from the turbulent combustion regime ($\mathrm{Re}_{\Lambda} > 1$). As noted previously, most practical combustion systems operate in the turbulent regime.

- Corrugated and wrinkled flamelet regimes: $\mathrm{Re}_{\Lambda} > 1$ and $\mathrm{Ka} < 1$. The line $\mathrm{Ka} = 1$ at which chemical time scale is equal to the Kolmogorov scale (Klimov-Williams criterion), separates the flamelet regime from the thin reaction zones regime. In these two regimes, the smallest spatial scales of the turbulence, η, are larger than the flame front thickness, δ_{L}, such that the flame front is embedded in the smallest eddies with its laminar structure intact and unaffected by the turbulence (see Figure 1.3(a)). the distinctions between the two flamelet regimes can be summarized as follows:

  - Wrinkled flamelet regime: $u' < s_{\mathrm{L}}$. In this regime, the laminar propagation is dominant and the interaction between turbulence and combustion remain limited. The speed of the larger turbulent motions is too low to wrinkle the flame front up to flame interactions [16].

  - Corrugated flamelet regime: $u' > s_{\mathrm{L}}$. In this regime, the larger turbulent motions are able to induce flame front interactions leading to the formations of pockets of fresh and burnt gases. Flame topology changes occur in the corrugated flamelet regime.

- Thin reaction zone regime: $1 < \mathrm{Ka} < 100$. In this regime, the turbulent integral time scale is still larger than the chemical time scale but the Kolmogorov scales are smaller than the flame thickness but larger than the reaction zone and are

able to modify the inner flame structure [16] as shown in Figure 1.3(b). The flame can no longer be identified as a laminar flame front but is still very much a wrinkled flame.

- Broken reaction zone regime: Ka > 100. In this regime, turbulent motions have shorter characteristic times than the chemical reaction time. Mixing is fast and the overall reaction rate is limited by chemistry [16]. The system is intensively disturbed by the small flow structure so that the reaction may take place in regions instead of layers as shown in Figure 1.3(c).

The original Klimov-Williams criterion states that laminar flamelets can not be observed in a reacting flow if the Kolmogorov scale, η, is smaller than the flame thickness, δ_{L}. Recent direct numerical simulation studies by Poinsot *et al.* [17] suggest that the flamelet regime can be extended to accommodate flames whose internal structure may be somewhat altered by small scale turbulence without leading to quenching of the flamelets. This suggests that the validity of flamelet assumption can be extended beyond the wrinkled and corrugated flamelet zones and well on into the thin reaction regime. This hypothesis will be examined as part of this thesis work.

1.1.4 Flamelet Assumption in Premixed Turbulent Combustion

The flamelet concept in premixed turbulent flames has been reviewed extensively by Peters [10] and Libby and Williams [18]. In many premixed turbulent combustion applications, turbulent time and spatial scales are longer compared with the chemical time and spatial scales [9], which results in the chemical reaction generally being confined to thin propagating surfaces with a thickness between 0.1 mm to 1 mm. The reacting mixture tends to be composed of unburned reactants and burnt products, separated by thin reacting interfaces called flamelets that preserve their locally laminar structure. This is the basic premise of the flamelet assumption.

The flamelet assumption reduces the modelling of the entire turbulent combustion problem to a more tractable two-fluid problem. The problem is reduced to that

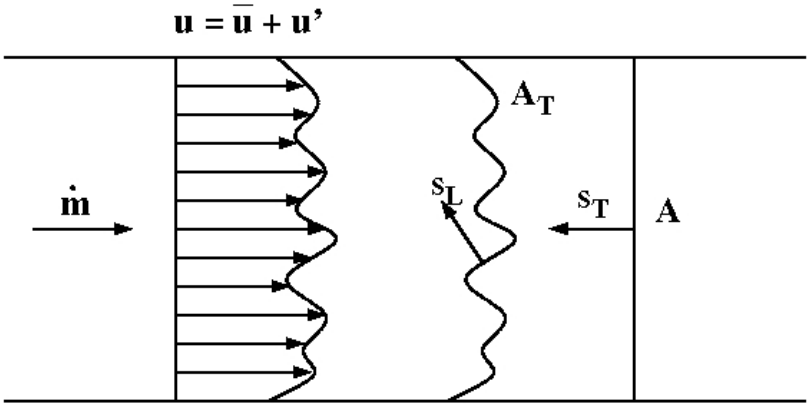

Figure 1.4: An idealized steady premixed flame in a duct.

of providing a description of the flow variables in the fresh and burnt gases, the motion and dynamics of the flame surface itself, and the local burning rate. Further simplifications can be made if it is assumed that the local structure of the reactive interfaces resembles a strained and curved laminar flame. In this situation, the local rate of reactant consumption can be approximated by that found for the planar laminar flame. This effectively decouples the effects of chemistry and turbulence. Chemical effects work to modify the local laminar flame speed, which may be obtained from separate laminar flame calculations [19]. The primary effect of the turbulence is to wrinkle and strain the embedded laminar flamelets. Damköhler [20] was the first to suggest that flame wrinkling is the main mechanism controlling turbulent flames and presenting theoretical expressions for the turbulent burning velocity [1]. In Figure 1.4, a schematic of a propagating premixed turbulent flame front is shown moving locally at the laminar flame speed, s_{L}, and the turbulent flame speed is defined as the speed the planar flame would have to move in order to consume the same amount of fresh gases. Conservation of mass flux, $\dot{m}$, yields

$$\dot{m} = \rho_{\mathrm{u}} s_{\mathrm{L}} A_{\mathrm{T}} = \bar{\rho}_{\mathrm{u}} s_{\mathrm{T}} A, \tag{1.8}$$

where $\bar{\rho}_{\mathrm{u}}$ is the mean unburnt mixture density, A is the cross-section area, and A_{T} is the total flame surface area. Ignoring the fluctuations of density, the increase in the turbulent flame speed compared to the laminar flame speed is due to the increase in the total flame surface, A_{T}, resulting from a higher fuel consumption rate for the

same cross-section area, A, and the relationship between s_{T} and s_{L} can be expressed as

$$\frac{s_{\mathrm{T}}}{s_{\mathrm{L}}} = \frac{A_{\mathrm{T}}}{A} = \Xi. \tag{1.9}$$

The ratio, Ξ, is the flame front wrinkling factor corresponding to the available flame surface divided by its projection in the mean propagation direction [16]. The wrinkling will depend on the turbulent Reynolds number and the fresh gas fluctuating velocity, u'.

One of the most widely used flamelet models of premixed turbulent combustion is the Bray-Moss-Libby model [21]. It applies a presumed probability density function (PDF) for the progress variable, c, which consists of two weighted delta functions at $c=0$ (unburnt gas) and $c=1$ (burnt gas). The model introduces the concept of a thin reacting surface embedded within the turbulent flow. The mean reaction rate, $\bar{\dot{\omega}}$, is modelled by Bray [22] using the local flame surface area to volume ratio, Σ, and may be written as

$$\bar{\dot{\omega}} = \rho_{\mathrm{u}} s_{\mathrm{L}} I_0 \Sigma, \tag{1.10}$$

where I_0 is a factor that accounts for the effects of flame curvature and strain on the laminar consumption rate.

Note that there are number of other approaches to the modelling of premixed turbulent combustion based on the flamelet concept. These include the G-equation formulation and the flame surface density. These models are discussed in greater detail in Chapter 3 of this thesis.

1.1.5 Numerical Approaches for Turbulent Combustion

The treatment of the turbulence is an important consideration in the modelling of turbulent combusting flows. Three different approaches are generally possible. They are: (i) Direct Numerical Simulation (DNS), (ii) Reynolds-Averaged Navier-Stokes (RANS), and (iii) Large-Eddy Simulation (LES). In comparison to one another, each of these methods possess various advantages and disadvantages [23, 24]. DNS is the most accurate method in which all scales of the turbulent flow field are resolved in the

computation and no turbulence model is required. It involves the solution of the conservation equations down to the smallest physical scales (i.e., the Kolmogorov scales). While modelling is avoided, this resolution requirement makes DNS computationally expensive and generally impractical for engineering problems. Note that the number of grid points required to simulate the full range of turbulence scales, even for somewhat simple flow geometries, may be estimated to be proportional to $\mathrm{Re}_\Lambda^{9/4}$ [25], where Re_Λ is the turbulence Reynolds number. For many practical applications, the turbulence Reynolds number is very large, making computational requirements for DNS enormous. DNS can be even more unfeasible for reacting flows and/or for flows having complex geometries. It should be pointed out, however, that DNS has its place in the numerical prediction of turbulent combustion. It has been applied with considerable success to low Reynolds number flows and effectively employed as a research tool for model development [18]. Some recent examples of the application of DNS techniques to problems in combustion are described by Vervisch [26].

RANS approaches introduce the notion of averages of flow variables, and the time averaged governing equations. This results in unclosed correlations which must be modelled. RANS methods do not resolve any part of the turbulent fluctuations and introduce some unclosed terms from the time-averaging procedure. The entire effect of the turbulent fluctuations and these unclosed terms on the mean flow must be modelled. In general, the complexity of turbulence makes it impossible for a single RANS model to represent all turbulent flows and thus some adjustment of model parameters is often required. Several models have been proposed in the past such as algebraic models by Baldwin-Lomax [27], one-equation models by Spalart-Allmaras [28], two-equation models (k-ε by Launder [29], k-ω by Wilcox [30]) and stress-transport models by Launder-Reece-Rodi [31]. A primary attraction of RANS approaches is that it is the least expensive approach of the possible methods in terms of computational effort.

LES represents a compromise between DNS and RANS approaches, where large structures are explicitly computed and small structures (smaller than the filter scale) are modelled by subfilter-scale (SFS) models [32]. Thus in LES, there is partial resolution of the turbulent fluctuations. This partial resolution increases the com-

putational cost but decreases the importance of modelling and effects of modelling uncertainty [33, 34].

Although not of primary concern here, it should be noted that other numerical approaches for the treatment of turbulence are possible. These include Hybrid RANS/LES, Semi-Deterministic Simulation (SDS), and Detached-Eddy Simulation (DES). Extensive reviews of these alternate approaches can be found in the review papers by Sagaut [35] and Wagner *et al.* [36].

1.1.6 Large-Eddy Simulation of Premixed Turbulent Combustion

For non-reacting flows, large-eddy simulation has become quite well established in recent years, and several successful models have been developed for the transfer of momentum and kinetic energy to the subfilter-scales [33]. However for reacting flows, while very promising, it is still in the early stages. In particular, for many premixed combustion applications, the chemical reactions are confined to propagating surfaces that are significantly thinner than the computational grids used in practical LES. In these situations, the chemical kinetics and its interaction with the turbulence are not resolved and must be entirely modelled. There is therefore a need for accurate and robust physical modelling of combustion at the subfilter-scales.

There has been considerable interest in LES of premixed combustion. Möller *et al.* [37] have applied a variety of LES combustion models to unsteady bluff body stabilized flames. Menon and Jou [38] and Kim *et al.* [39] have successfully applied LES based on flame front propagation to combustion in a gas turbine. Weller *et al.* [40] have used a flame wrinkling model in the context of a reacting shear layer. Angelberger *et al.* [41] and Veynante and Poinsot [42] used a thickened flame approach to study combustion instabilities of a turbulent premixed flame. Pitsch and Duchamp [14] applied a formulated G-equation concept for LES premixed turbulent combustion with complex methane chemistry. Hawkes [25] and Hawkes and Cant [43] proposed a transport equation model for flame surface density (FSD) and validated the model for flames propagating in homogeneous isotropic turbulence. Most of the

LES studies listed above, the subfilter-scale models for reaction rate modelling are largely based on the flamelet assumption discussed earlier in Subsection 1.1.4.

This research work considers the application of the FSD model of Hawkes [25] and Hawkes and Cant [43] with a full treatment for the energy equation to the LES of freely propagating flames and Bunsen type flames under various turbulent conditions. The FSD models provide a measure of the wrinkled flame area per unit volume on the subfilter-scale. The FSD approach for LES is based on filtering the governing equations with a filter width sufficiently larger than the grid spacing such that the thin turbulent dynamic premixed flame is smeared out and can be resolved on a LES grid [44]. A model is then required to account for the subfilter FSD and can be provided through either an algebraic expression or by solving a transport equation for the FSD [33]. As a viable new approach to LES of premixed combustion, the modelled FSD transport equation developed by Hawkes [25] and Hawkes and Cant [43] has advantages over other approaches in which the physical mechanisms of flame surface density production and destruction are represented directly by both resolved and unresolved terms in the transport equation.

1.2 Motivation and Objectives

The primary goal of this thesis was to apply the FSD model of Hawkes and Cant in an LES framework, Favre-filtered Navier-Stokes equations governing compressible flows of a thermally perfect reactive mixture of gases. The LES algorithm for the prediction of turbulent premixed flames was the focus of the research. The results were compared to available experimental data to investigate its effectiveness in the modelling of lean-premixed turbulent combustion.

A summary of the main objectives of this doctoral thesis is then as follows:

- to develop an LES framework with finite-volume formulation for predicting multi-species turbulent reacting flows applied to the compressible form of the governing equations;

- to assess subfilter-scale models for turbulent premixed combustion;

- to investigate the resolution requirement of FSD with an adaptive mesh refinement (AMR) scheme and the flame dynamics and stability of lean-premixed turbulent combustion; and
- to compare the LES numerical results to the available experimental data for stoichiometric and lean premixed turbulent Bunsen type flames.

1.3 Thesis Outline

Following this introduction, Chapter 2 of the thesis provides a summary of the Favre-filtered governing equations describing a compressible thermally perfect reactive mixture of gases. In Chapter 3, reaction rate modelling and details of the LES filtered transport equation for the flame surface density are presented. Chapter 4 discusses the main elements of the finite-volume scheme and parallel adaptive mesh refinement scheme developed for solving the governing flow and FSD model equations and performing the LES simulation. Chapter 5 presents two- and three-dimensional LES results for freely-propagating flames in decaying isotropic turbulence flows and Bunsen type premixed flames. Comparison is made between the numerical results and available experiment data. Model behavior is qualitatively examined and it is found that the model reproduces the behavior expected of the propagating flame in a turbulent field. Conclusions from the present work and suggestions for the future studies are described in Chapter 6.

Chapter 2

Filtered Equations for LES Turbulent Premixed Combustion

2.1 Favre-Filtered Navier-Stokes Equations

2.1.1 LES filtering

Large-eddy simulation is based on a filtering of the governing conservation equations. In LES, the relevant quantities, φ, may be filtered in the spectral space (components greater than a given cut-off frequency are suppressed) or in the physical space (weighted averaging for a given volume of physical space). Temporal filtering is also possible, however, we will only consider spatial filtering techniques in this research.

The spatial filtering operation for a solution quantity, φ, can be defined by [45]

$$\bar{\varphi}(\vec{x}) = \int_{-\infty}^{+\infty} \varphi(\vec{x}^*) F(\vec{x} - \vec{x}^*) \mathrm{d}\vec{x}^*, \tag{2.1}$$

where F is the LES filter. Standard spatial filters are the box filter in the physical space given by [45]

$$F(\vec{x}) = F(x_1, x_2, x_3) = \begin{cases} 1/\Delta^3, & \text{if } |x_i| \leq \Delta/2, i = 1, 2, 3, \\ 0, & \text{otherwise,} \end{cases} \tag{2.2}$$

where (x_1, x_2, x_3) are the spatial coordinates of the location $\vec{x}$ and Δ is the filter

width, and the Gaussian filter is given by

$$F(\vec{x}) = F(x_1, x_2, x_3) = \Big(\frac{6}{\pi\Delta^2}\Big)^{3/2} \exp\Big[-\frac{6}{\Delta^2}(x_1^2 + x_2^2 + x_3^2)\Big]. \tag{2.3}$$

Both of these filters are normalized such that

$$\int_{-\infty}^{+\infty}\int_{-\infty}^{+\infty}\int_{-\infty}^{+\infty} F(x_1, x_2, x_3)\mathrm{d}x_1\mathrm{d}x_2\mathrm{d}x_3 = 1. \tag{2.4}$$

For compressible combusting flows, a mass-weighted, Favre filtering procedure, is introduced as defined by

$$\bar{\rho}\tilde{\varphi}(\vec{x}) = \int_{-\infty}^{+\infty} \rho\varphi(\vec{x}^*)F(\vec{x} - \vec{x}^*)\mathrm{d}\vec{x}^*, \tag{2.5}$$

where ρ is the flow density. The Favre filtering has the advantage for compressible flows that the filtered continuity equation, Eq. 2.6, is closed exactly without the need for modelling of high-order filtered quantities.

The filtering operation most commonly used in LES is the implicit or Schumann filtering [46], in which the computational grid and the discretization operators are considered as the filter for the governing equations. In this case, the filter width is taken to be some multiple of the grid size and effective SFS models are generally dissipative and damp out solution content smaller than the filter width. Using explicit filtering, the filtering procedure is separated from the grid and discretization operators. Thus, a grid-independent LES solution can be expected by maintaining constant filter widths [47–49] and or using constant commutative filters. Nevertheless, as in most practical LES studies to date, an implicit filtering approach is used in this research.

2.1.2 Filtered Conservation Equations

The low-pass spatial filtering procedure defined above provides a separation of scales for the solution content. Solution content having scales larger than the filter size, Δ, is fully resolved, whereas solution of scales smaller than Δ must be modeled. The relevant quantities, φ, are filtered, Favre-filtered (mass-weighted filtering), or evaluated in terms of the filtered quantities to give $\bar{\varphi}$, $\tilde{\varphi}$, or $\check{\varphi}$, respectively. The

Navier-Stokes equations governing compressible flows of a thermally perfect reactive mixture of gases are used herein to describe and predict the time evolution of turbulent premixed combustion processes. Application of the spatial filtering procedure to this equation set results in the Favre-filtered form of the Navier-Stokes equations governing transport of the mixture mass, momentum, and energy as well as species mass transport. They are given by

$$\frac{\partial \bar{\rho}}{\partial t} + \frac{\partial (\bar{\rho}\tilde{u}_i)}{\partial x_i} = 0, \tag{2.6}$$

$$\frac{\partial (\bar{\rho}\tilde{u}_i)}{\partial t} + \frac{\partial (\bar{\rho}\tilde{u}_i\tilde{u}_j + \delta_{ij}\bar{p})}{\partial x_i} - \frac{\partial \check{\tau}_{ij}}{\partial x_i} = \underbrace{-\frac{\partial \sigma_{ij}}{\partial x_i}}_{\text{I}} + \underbrace{\frac{\partial (\bar{\tau}_{ij} - \check{\tau}_{ij})}{\partial x_i}}_{\text{II}}, \tag{2.7}$$

$$\begin{aligned}\frac{\partial (\bar{\rho}\tilde{E})}{\partial t} + \frac{\partial [(\bar{\rho}\tilde{E} + \bar{p})\tilde{u}_i]}{\partial x_i} - \frac{\partial (\check{\tau}_{ij}\tilde{u}_i)}{\partial x_i} + \frac{\partial \check{q}_i}{\partial x_i} = & \underbrace{-\frac{\partial [\bar{\rho}(\widetilde{h_{\text{s}}u_i} - \tilde{h}_{\text{s}}\tilde{u}_i)]}{\partial x_i}}_{\text{III}} \\ & \underbrace{-\frac{\partial [\sum_{n=1}^{N_s} \Delta h^0_{\text{f},n}\bar{\rho}(\widetilde{Y_n u_i} - \tilde{Y}_n\tilde{u}_i)]}{\partial x_i}}_{\text{IV}} \\ & \underbrace{-\frac{1}{2}\frac{\partial [\bar{\rho}(\widetilde{u_i u_j u_j} - \tilde{u}_i\widetilde{u_j u_j})]}{\partial x_i}}_{\text{V}} \\ & + \underbrace{\frac{\partial (\bar{\tau}_{ij}\tilde{u}_i - \check{\tau}_{ij}\tilde{u}_i)}{\partial x_i}}_{\text{VI}} + \underbrace{\frac{\partial (\overline{\tau_{ij}u_i} - \bar{\tau}_{ij}\tilde{u}_i)}{\partial x_i}}_{\text{VII}} \\ & \underbrace{-\frac{\partial (\check{q}_i - \bar{q}_i)}{\partial x_i}}_{\text{VIII}},\end{aligned} \tag{2.8}$$

$$\frac{\partial (\bar{\rho}\tilde{Y}_n)}{\partial t} + \frac{\partial (\bar{\rho}\tilde{Y}_n\tilde{u}_i)}{\partial x_i} + \frac{\partial \check{\mathcal{J}}_{n,i}}{\partial x_i} = \underbrace{-\frac{\partial [\bar{\rho}(\widetilde{Y_n u_i} - \tilde{Y}_n\tilde{u}_i)]}{\partial x_i}}_{\text{IX}} \underbrace{-\frac{\partial (\tilde{\mathcal{J}}_{n,i} - \check{\mathcal{J}}_{n,i})}{\partial x_i}}_{\text{X}} + \underbrace{\bar{\dot{\omega}}_n}_{\text{XI}}, \tag{2.9}$$

where

$$\bar{p} = \bar{\rho}R\widetilde{T} + \underbrace{\sum_{n=1}^{N_s} R_n\bar{\rho}(\widetilde{Y_n T} - \widetilde{Y}_n\widetilde{T})}_{\text{XII}}, \tag{2.10}$$

$$\tilde{E} = \check{h}_\mathrm{s} + \sum_{n=1}^{N_s} \tilde{Y}_n \Delta h^0_{\mathrm{f},n} - \frac{\bar{p}}{\bar{\rho}} + \frac{1}{2}\widetilde{u_j u_j}, \tag{2.11}$$

$$\check{\tau}_{ij} = 2\check{\mu}(\check{S}_{ij} - \frac{1}{3}\delta_{ij}\check{S}_{kk}), \tag{2.12}$$

$$\check{q}_i = -\check{\kappa}\frac{\partial \tilde{T}}{\partial x_i} - \bar{\rho}\sum_{n=1}^{N_s} \check{h}_n \check{D}_n \frac{\partial \tilde{Y}_n}{\partial x_i}. \tag{2.13}$$

$$\check{\mathcal{J}}_{n,i} = -\bar{\rho}\check{D}_n \frac{\partial \tilde{Y}_n}{\partial x_i} \tag{2.14}$$

Here, $\bar{\rho}$ is the filtered mixture density, $\tilde{u}_i$ is the Favre-filtered mixture velocity, $\bar{p}$ is the filtered mixture pressure (Eq. 2.10), $\tilde{E}$ is the Favre-filtered total mixture energy (including chemical energy) given by Eq. 2.11, $\check{h}_\mathrm{s}$ is the sensible enthalpy and $\Delta h^0_{\mathrm{f,n}}$ is the heat of formation for species n, $\tilde{Y}_n$ is the Favre-filtered mass fraction of species n, and $\overline{\dot{\omega}}$ is the filtered reaction rate. The resolved viscous stress tensor, $\check{\tau}_{ij}$, is evaluated in terms of the filtered quantities by Eq. 2.12, $\check{q}_i$ is the resolved total heat flux (Eq. 2.13), $\check{\mathcal{J}}_{n,i}$ is the resolved species diffusive fluxes (Eq. 2.14), $\tilde{T}$ is the mixture temperature, $\check{\mu}$ is the mixture viscosity, $\check{\kappa}$ is the mixture thermal conductivity, and $\check{D}_n$ is the diffusivity of species n with respect to the mixture. The strain rate tensor, $\check{S}_{ij}$, is given by

$$\check{S}_{ij} = \frac{1}{2}(\frac{\partial \tilde{u}_i}{\partial x_j} + \frac{\partial \tilde{u}_j}{\partial x_i}). \tag{2.15}$$

The terms on the right-hand side (RHS) are subfilter-scale terms, which represent the effect of the unresolved scales on the resolved solution content. Unlike the terms on the left-hand side (LHS) of the equations, these terms cannot be expressed directly in terms of the filtered flow variables and modelling is required for these terms. A summary of the subfilter-terms, introduced by the Favre-filtering of the governing equations, is as follows:

- Term I results from the non-linearity of the convective term and needs modelling.

- Term II results from the non-linearity of the viscous term and the fact that the Favre filtering procedure and partial differentiation do not commute. Term II is generally neglected under the assumption that $\bar{\tau}_{ij} - \check{\tau}_{ij} = 0$. A priori tests confirm that this term is an order of magnitude smaller than term I [50].

- Term III and IV are the sensible enthalpy and species heat formation subfilter terms which also require modelling.

- Term VI and VIII arise from the non-linearities of the viscous stresses and the heat flux, respectively. Using assumptions similar to those used as for term II, these terms can also generally be neglected.

- Term VII represents the SFS viscous diffusion and is generally much smaller than the other terms that require modelling, and is therefore generally neglected [51].

- Term V is the SFS turbulent diffusion and this term must be modelled.

- Terms IX and XII are similar in nature to term III, term X is similar to term VIII, and term XI is the filtered reaction rate term which has to be modelled.

As noted previously, there are no subfilter terms appearing in the continuity equation as a Favre-filtering procedure is applied here.

2.1.3 The Closure Problem

Based on the summary of the SFS terms appearing in the governing equations given above, the closure problem for LES therefore involves specification of the following quantities in terms of the resolved solution values:

- the subfilter-scale stresses, $\sigma_{ij} = \bar{\rho}(\widetilde{u_i u_j} - \tilde{u}_i \tilde{u}_j)$;

- the subfilter-scale turbulent transport, $(\widetilde{u_i u_j u_j} - \tilde{u}_i \widetilde{u_j u_j})/2$;

- the subfilter-scale enthalpy flux, $\bar{\rho}(\widetilde{h_\mathrm{s} u_i} - \tilde{h}_\mathrm{s} \tilde{u}_i)$;

- the subfilter-scale species flux, $\bar{\rho}(\widetilde{Y_n u_i} - \tilde{Y}_n \tilde{u}_i)$; and

- the filtered reaction rate, $\overline{\dot{\omega}}$.

The challenge is to construct robust models for these subfilter-scale terms that will provide statistically accurate and meaningful results for the large scale flow structures. In the following section, various closure strategies used herein, which have been employed in previous studies of compressible reactive flows for modelling the subfilter-scale terms, are summarized and discussed.

2.2 Subfilter-Scale Stresses

The SFS stress is represented by term I and given by

$$\sigma_{ij} = \bar{\rho}(\widetilde{u_i u_j} - \tilde{u}_i \tilde{u}_j). \tag{2.16}$$

The modelling of this term has attracted considerable attention to date for both non-reactive and reactive flows as it is primarily responsive for the mimicking of the turbulent energy cascade [52]. A brief overview of the several important modelling concepts for this SFS term now follows.

2.2.1 Smagorinsky Model

The earliest and simplest SFS stress model was proposed by Smagorinsky [53] in 1963. The so-called Smagorinsky model has been widely used for incompressible flow applications and models the SFS stress tensor in a similar way to the Boussinesq approximation and eddy-viscosity concept commonly used in RANS simulations. In the Smagorinsky model for incompressible flow, the SFS stresses are assumed to have the form

$$\sigma_{ij} - \frac{\delta_{ij}}{3}\sigma_{kk} = -\bar{\rho}\nu_{\mathrm{t}}\Big(\frac{\partial \tilde{u}_i}{\partial \tilde{x}_j} + \frac{\partial \tilde{u}_j}{\partial \tilde{x}_i}\Big) = -2\bar{\rho}\nu_{\mathrm{t}}\check{S}_{ij}, \tag{2.17}$$

where ν_{t} is the subfilter-scale turbulent viscosity. Smagorinsky postulated the following form for ν_{t} :

$$\nu_{\mathrm{t}} = (C_{\mathrm{s}}\Delta)^2|\check{S}|, \tag{2.18}$$

where $|\check{S}|$ is the magnitude of the filtered strain rate tensor given by

$$|\check{S}| = \sqrt{2\check{S}_{ij}\check{S}_{ij}}, \tag{2.19}$$

and C_s is the Smagorinsky coefficient, which can be determined from computations of isotropic turbulence decay, and has been found to lie in the range between 0.1 and 0.25. In Eq. 2.18, the factor Δ can be seen as the subfilter-scale mixing length and $(C_\mathrm{s}\Delta)^2|\check{S}|$ as the mixing velocity.

For variable density flows, the model must include the trace of the strain rate tensor in the Reynolds stress, then σ_{ij} is given by

$$\sigma_{ij} - \frac{\delta_{ij}}{3}\sigma_{kk} = -\bar{\rho}\nu_\mathrm{t}\Big(\frac{\partial\tilde{u}_i}{\partial\tilde{x}_j} + \frac{\partial\tilde{u}_j}{\partial\tilde{x}_i} - \frac{2}{3}\delta_{ij}\frac{\partial\tilde{u}_k}{\partial\tilde{x}_k}\Big) = -2\bar{\rho}\nu_\mathrm{t}\Big(\check{S}_{ij} - \frac{\delta_{ij}}{3}\check{S}_{kk}\Big). \tag{2.20}$$

The SFS stress for compressible flows is then given by

$$\sigma_{ij} = -2\bar{\rho}\nu_\mathrm{t}\left(\check{S}_{ij} - \frac{\delta_{ij}}{3}\check{S}_{kk}\right) + \frac{\delta_{ij}}{3}\sigma_{kk}. \tag{2.21}$$

The trace of the SFS stress tensor, σ_{kk}, can be modelled by using the following expression proposed by Yoshizawa [54]:

$$\sigma_{kk} = 2\bar{\rho}C_\mathbf{I}\Delta^2|\check{S}|^2, \tag{2.22}$$

where $C_\mathbf{I}$ is an additional closure coefficient that is generally quite small, lying somewhere between 0.005 to 0.0066.

In general, the Smagorinsky model is based on the assumption that the SFS stress tensor behaves similarly to the viscous stress tensor, which is proportional to the strain rate tensor. It assumes that the SFS turbulence is approximately in equilibrium with the energy cascaded down from the large or resolved scales. It may be expected that the energy exchange between resolved and subfilter-scale motion is associated with a length scale characteristic of the subfilter-scale motion, which is generally taken as the filter width, Δ.

The main limitation of this model is that it requires a priori specification of the Smagorinsky constant. Since the optimal value varies under different flow conditions, there is some variation in the value of C_s given in the literature. For instance for

channel flows, a value of $C_s = 0.2$ is known to give reasonable results in the center of the channel while it should be reduced to 0.06 close to the wall. Another drawback of this model is that it does not exhibit the correct limiting behavior near a wall. A damping function similar to that proposed by van Driest [55] can be used so that ν_t vanishes near the solid boundaries. Nevertheless, the Smagorinsky model seems to provide roughly the correct amount of dissipation to account for the energy cascade and the transfer of energy down to the subfilter-scale (Speziale [56]), and has been widely used and gives reasonable results, with some adjustment of the constant, for a variety of situations (Fureby *et al.* [57, 58], Ferziger [59]).

2.2.2 Dynamic Model

The dynamic model was originally developed by Germano *et al.* [60] and modified by Moin *et al.* [61] for the LES of compressible flows. Lilly [62] proposed a least squares technique to minimize the difference between the closure assumption and the resolved stresses. The objective of the dynamic model concept is to estimate the small scale dissipation, and hence solution dependent value of the closure coefficient, C_s, from the knowledge of the resolved scales by introducing a test filter with a filter width larger than the resolved grid filter, which generates a second filtered field with cut-off scales larger than the resolved field. Given any solution quantity, φ, the spatially test-filtered quantity is denoted here by $\hat{\varphi}$. For a test filter width, $\hat{\Delta}$, which is larger than the LES filter width, Δ, the test-filtered stresses can then be written as

$$\mathcal{Q}_{ij} = \widehat{\widetilde{u_i u_j}} - \widehat{\tilde{u}}_i \widehat{\tilde{u}}_j, \tag{2.23}$$

and the test-filtered SFS stresses are defined in a similar way as

$$\widehat{\sigma_{ij}} = \widehat{\widetilde{u_i u_j}} - \widehat{\tilde{u}_i \tilde{u}_j}. \tag{2.24}$$

The Germano identity involves the difference between the two relations above and is given by

$$\begin{aligned} \mathcal{L}_{ij} &= \mathcal{Q}_{ij} - \widehat{\sigma_{ij}} \\ &= (\widehat{\widetilde{u_i u_j}} - \widehat{\tilde{u}}_i \widehat{\tilde{u}}_j) - (\widehat{\widetilde{u_i u_j}} - \widehat{\tilde{u}_i \tilde{u}_j}) \\ &= \widehat{\tilde{u}_i \tilde{u}_j} - \widehat{\tilde{u}}_i \widehat{\tilde{u}}_j. \end{aligned} \tag{2.25}$$

It is clear from Eq. 2.25 above that the Germano identity, $\mathcal{L}_{ij}$, can be explicitly calculated from the resolved variables. By applying the test filter to the Smagorinsky modeled expression for σ_{ij}, the test-filtered values for $\widehat{\sigma_{ij}}$ may be written as

$$\widehat{\sigma_{ij}} - \frac{1}{3}\widehat{\sigma_{kk}}\delta_{ij} = -2\widehat{C_{\mathrm{s}}\alpha_{ij}}, \tag{2.26}$$

with α_{ij} given by

$$\alpha_{ij} = \bar{\rho}\Delta^2|\check{S}|(\check{S}_{ij} - \frac{1}{3}\check{S}_{kk}\delta_{ij}). \tag{2.27}$$

Approximating $\widehat{C_{\mathrm{s}}\alpha_{ij}} = C_{\mathrm{s}}\widehat{\alpha_{ij}}$, which is equivalent to assuming that C_{s} is constant over an interval at least equal to the test filter cutoff length, one obtains

$$\widehat{\sigma_{ij}} - \frac{1}{3}\widehat{\sigma_{kk}}\delta_{ij} = -2C_{\mathrm{s}}\widehat{\alpha_{ij}}. \tag{2.28}$$

The same model can also be used for the test field stresses as

$$\mathcal{Q}_{ij} - \frac{1}{3}\mathcal{Q}_{kk}\delta_{ij} = -2C_{\mathrm{s}}\beta_{ij} \tag{2.29}$$

with

$$\beta_{ij} = \hat{\bar{\rho}}\hat{\Delta}^2|\widehat{\check{S}}|(\widehat{\check{S}}_{ij} - \frac{1}{3}\widehat{\check{S}}_{kk}\delta_{ij}). \tag{2.30}$$

Now by inserting $\mathcal{Q}_{ij}$ from Eq. 2.29 and $\widehat{\sigma_{ij}}$ from Eq. 2.28 into Eq. 2.25, one has

$$\mathcal{L}_{ij} - \frac{1}{3}\mathcal{L}_{kk}\delta_{ij} = 2C_{\mathrm{s}}(\widehat{\alpha_{ij}} - \beta_{ij}) = 2C_{\mathrm{s}}M_{ij} \tag{2.31}$$

with $\mathcal{L}_{kk} = \mathcal{Q}_{kk} - \hat{\sigma}_{kk}$ and $M_{ij} = \widehat{\alpha_{ij}} - \beta_{ij}$.

To determine a single value for C_{s} at a given location in the flow field, Lilly [62] suggested minimizing the following square error measure:

$$E = (\mathcal{L}_{ij} - \frac{1}{3}\mathcal{L}_{kk}\delta_{ij} - 2C_{\mathrm{s}}M_{ij})^2. \tag{2.32}$$

Setting the first derivative of the square of the error, E, with respect to C_{s} equal to zero, $\mathrm{d}E/\mathrm{d}C_{\mathrm{s}} = 0$, and noting that the trace of the tensor M_{ij} is zero, the following expression for the Smagorinsky closure coefficient is obtained:

$$C_{\mathrm{s}} = \frac{\mathcal{L}_{ij}M_{ij}}{2M_{ij}M_{ij}}. \tag{2.33}$$

The model parameter C_s can be calculated dynamically as part of the solution, from Eq. 2.33 instead of adjusting its value via a tuning exercise as in the Smagorinsky model. However, this procedure may sometimes yield negative values of C_s which is inconsistent with the Smagorinsky model. It has been argued that negative values should be allowed to represent the phenomenon of energy backscatter [63], in which the energy is transferred from small scales to large scales. However, a negative value for C_s results in a negative eddy viscosity, ν_t, and this can destabilize the numerical simulation. The calculated value for C_s may also fluctuate strongly in both space and time which may also act to destabilize LES calculations.

2.2.3 Subfilter-Scale Kinetic Energy One-Equation Model

The one-equation model is an attempt to refine the subfilter-scale stress modelling of the momentum transport for the many situations in which the Smagorinsky model is not necessarily valid. It was proposed by Yoshizawa *et al.* [54], and improved by Menon *et al.* [39]. Many researchers, such as Schumann [64], Schmidt and Schumann [65], and Yoshizawa [66, 67], have employed this approach.

Defining the subfilter-scale kinetic energy, $\tilde{k}$, as

$$\tilde{k} = \frac{1}{2}\bar{\rho}\sigma_{kk} = \frac{1}{2}(\widetilde{u_k u_k} - \tilde{u}_k\tilde{u}_k), \tag{2.34}$$

the sub-filter stresses in the one-equation approach are modelled using a Boussinesq type assumption and given by

$$\sigma_{ij} = -2\bar{\rho}C_\nu\Delta\sqrt{\tilde{k}}\left(\check{S}_{ij} - \frac{\delta_{ij}}{3}\check{S}_{kk}\right) + \frac{2}{3}\bar{\rho}\tilde{k}\delta_{ij}, \tag{2.35}$$

where the SFS turbulent viscosity, ν_t, is prescribed using the SFS kinetic energy, $\tilde{k}$, and the filter width, Δ, as follows

$$\nu_t = C_\nu\Delta\sqrt{\tilde{k}}, \tag{2.36}$$

and where C_ν is the model constant.

An unclosed transport equation for the subfilter-scale kinetic energy, $\tilde{k}$, has been presented in previous work by Schumann [64] and Germano [68], respectively, and

there are various modelled transport equations having a similar form. In this thesis, a modelled scalar transport equation for the SFS kinetic energy is solved along with the Favre-filtered governing equations and the former is taken to have the form

$$\frac{\partial \overline{\rho k}}{\partial t} + \frac{\partial \bar{\rho} \tilde{u}_i \tilde{k}}{\partial x_i} = \frac{\partial}{\partial x_i} \left(\bar{\rho} (\frac{\nu_\mathrm{t}}{\mathrm{Pr}_\mathrm{t}} + \nu) \frac{\partial \tilde{k}}{\partial x_i} \right) - \sigma_{ij} \breve{S}_{ij} - C_\epsilon \frac{\bar{\rho} \tilde{k}^{3/2}}{\Delta}, \tag{2.37}$$

where Pr_t is the turbulent Prandtl number for the subfilter-scale turbulent transport of $\tilde{k}$. The RHS of Eq. 2.37 features diffusive transport of k by molecular collisions and SFS turbulence (turbulent transport), the production of the SFS turbulence by the resolved scales, and an approximation for the dissipation rate, $\epsilon = C_\epsilon \tilde{k}^{3/2} / \Delta$.

A number of previous studies have assessed the values of the model constants and turbulence Prantl number to be used in the preceding one-equation model. Schmidt and Schumann [65] used $C_\nu = 0.086$, $C_\epsilon = 0.845$, and $\mathrm{Pr}_\mathrm{t} = 0.25$. Yoshizawa [67] employed $C_\nu = 0.09$, $C_\epsilon = 1.0$, and $\mathrm{Pr}_\mathrm{t} = 1.0$. Ghosal *et al.* [69] and Kim and Menon [39] determined the model coefficients C_ν, C_ϵ, and Pr_t using a dynamic procedure.

The one-equation model offers the advantages that non-equilibrium effects at the subfilter-scale level are taken into account and that the subfilter-scale turbulent viscosity vanishes for fully resolved turbulent flow, i.e., $\tilde{k} \to 0$ as $\Delta \to 0$. In addition, it may be seen from Eq. 2.36 that, since $k \geq 0$, no backscatter of turbulent energy is allowed associated with negative values of the SFS viscosities. It also recovers a form of the k-ϵ model used in RANS model closure. Aside from these advantages, the one-equation model does have one main drawback and that is the need to solve one additional transport equation and its associated computational cost.

2.2.4 Other Models and Modelling Used Here

There are several other approaches to subfilter-scale stress modelling, such as two-point closures (Chollet and Lesieur [70]), scale similarity models (Bardina *et al.* [71]), and structure-function models (Métais and Lesieur [72]). In this research, the Smagorinsky and one-equation models have been implemented and are both used for modelling the SFS turbulent stresses.

2.3 Subfilter-Scale Scalar Transport

The subfilter-scale enthalpy flux, $\bar{\rho}(\widetilde{h_s u_i} - \tilde{h}_s \tilde{u}_i)$, and the subfilter-scale species flux, $\bar{\rho}(\widetilde{Y_n u_i} - \tilde{Y}_n \tilde{u}_i)$, are usually modelled using standard gradient assumptions and given by

$$\bar{\rho}(\widetilde{h_s u_i} - \tilde{h}_s \tilde{u}_i) = -C_p \frac{\bar{\rho}\nu_t}{\mathrm{Pr_t}} \frac{\partial \tilde{T}}{\partial x_i}, \tag{2.38}$$

and

$$\bar{\rho}(\widetilde{Y_n u_i} - \tilde{Y}_n \tilde{u}_i) = -\frac{\bar{\rho}\nu_t}{\mathrm{Sc_t}} \frac{\partial \tilde{Y}_n}{\partial x_i}, \tag{2.39}$$

where C_p is the heat capacity, $\mathrm{Sc_t}$ is the turbulent Schmidt number. Following a generalization of the Reynolds analogy concept, the turbulence scalar transport coefficients, $\bar{\rho}\nu_t/\mathrm{Pr_t}$ and $\bar{\rho}\nu_t/\mathrm{Sc_t}$, are products of the turbulence momentum transfer coefficient, $\bar{\rho}\nu_t$, and $1/\mathrm{Pr_t}$, and $1/\mathrm{Sc_t}$, respectively. The two gradient-based models given above are used in this thesis for the modelling of SFS scalar transport.

2.4 Subfilter-Scale Turbulent Transport

The subfilter-scale turbulent transport term, $(\widetilde{u_i u_j u_j} - \tilde{u}_i \widetilde{u_j u_j})/2$, arises from the filtering of convective term in energy equation. Knight *et al.* [73] proposed a model for this term that has a form that is similar to the subfilter-scale turbulence diffusion and is given by

$$\frac{1}{2}(\widetilde{u_i u_j u_j} - \tilde{u}_i \widetilde{u_j u_j}) = \sigma_{ij} \tilde{u}_i. \tag{2.40}$$

The Knight *et al.* [73] model is used here to model the SFS turbulent transport.

2.5 Reaction Rate Modelling

Last, but certainly not least, the modelling of the filtered reaction rates appearing in Eq. 2.9 is of particular interest to this thesis research and introduces a number of challenges when performing LES of reactive flows. This is due to the highly nonlinear dependence of the reaction rates on the temperature and species mass fractions. It is also particularly challenging for turbulent premixed combustion where the flame

thickness, δ, is 0.1–1.0 mm. This is, in many cases, considerably smaller than practical LES filter widths, Δ. To overcome this difficulty, a number of subfilter-scale models have been proposed for LES of premixed flames and modelling of flame front propagation. In the next chapter, Chapter 3, a review is given of three of the more common and/or popular models for determination of the subfilter-scale reaction rates: the thickened flame model [74], the G-equation model [1], and the flame surface density model [25], all of which are based to a large extent on the flamelet concept.

Chapter 3

Reaction Rate Modelling and Flame Surface Density Model

Modelling of the reaction rates presents difficulties, particularly for turbulent premixed combustion, due to the fact that the thermochemical variables vary very sharply through the flame profile, which is typically very thin. To overcome this difficulty, three main approaches based on the laminar flamelet assumption have been proposed: (i) simulation of an artificially thickened flame; (ii) use of a flame front tracking technique based on G-equation; and (iii) use of a filtered progress variable with a reaction rate that depends on the flame surface density [16]. In this chapter, an overview of the reaction rate modelling will be given for these three main flamelet subfilter-scale models. This is followed by details of flame surface density model, the model of primary interest here, including theory of flame surface density for LES in Section 3.2.3 and algebraic FSD modelling approaches in Section 3.2.4. The modelling of the transport equation of Hawkes and Cant for the LES using FSD model is addressed in Section 3.2.5.

3.1 Reaction Rate Modelling

3.1.1 Thickened Flame Model

The thickened flame model, originally developed by Butler and O'Rourke [75], is very attractive due to its inherent numerically stabilizing features. It has been applied to LES of premixed combustion by Thibaut and Candel [76] and Veynante and Poinsot [77]. In the thickened flame model, the computed flame front structure is artificially thickened locally while maintaining the same laminar flame speed so that the thickened flame front can be resolved on the LES mesh [78].

From the theory of laminar premixed flames, it is well established that the laminar flame speed, s_{L}, and the laminar flame thickness, δ_{L}, scale as

$$s_{\mathrm{L}} \propto \sqrt{D\dot{\omega}}\,, \tag{3.1}$$

and

$$\delta_{\mathrm{L}} \propto D/s_{\mathrm{L}}\,, \tag{3.2}$$

where D is the molecular diffusivity and $\dot{\omega}$ is the reaction rate. Thus, an increase in flame thickness by a factor, F, with a constant flame speed, can be achieved by multiplying the diffusivity, D, by F, and the reaction rate, $\dot{\omega}$, by $1/F$. An efficiency factor, E_{F}, is also introduced to account for the resulting decrease in the Damköhler number, Da, for the flame [74] and the influence of the subfilter-scale turbulence on the propagation of the flame. The resulting filtered balance equation for chemical species takes the modified form

$$\frac{\partial}{\partial t}\left(\bar{\rho}\tilde{Y}_n\right) + \frac{\partial}{\partial x_i}\left(\bar{\rho}\tilde{Y}_n\tilde{u}_i\right) = \frac{\partial}{\partial x_i}\left[E_{\mathrm{F}}F\bar{\rho}\left(\tilde{D}_n + \frac{\nu_{\mathrm{t}}}{\mathrm{Sc}_{\mathrm{t}}}\right)\frac{\partial\tilde{Y}_n}{\partial x_i}\right] + \frac{E_{\mathrm{F}}\overline{\dot{\omega}}_n}{F}\,, \tag{3.3}$$

where the filtered reaction rate, $\overline{\dot{\omega}}_n$, is now calculated directly using Arrhenius law reaction rates evaluated in terms of resolved or filtered quantities. Typically, the thickening factor, F, is in the range from 5 to 30 in the vicinity of the flame front and near unity far from the flame such that the thickened flame front may then be adequately resolved on the LES computational mesh.

As noted above, the consequence of thickening the flame is the reduction of the Damköhler number, altering the interaction between the turbulence and the chemistry. To counteract this reduction, the subfilter-scale flame surface wrinkling model has been introduced. In this case, the efficiency factor, E_{F}, defined above, can be evaluated using a power-law flame wrinkling model. Assuming that the internal structure of the flame is not significantly altered by the turbulence, as in the wrinkled flamelets, corrugated flamelets, and thin reaction zones premixed combustion regimes [1], and that the increased flame surface area due to the flame front wrinkling by the subfilter-scale turbulence leads to an increase in the flame speed, a power-law expression is used to evaluate E_{F} given by [79, 80]

$$\frac{s_{\mathrm{Tsfs}}}{s_{\mathrm{L}}} = \frac{A_{\Delta}}{\Delta^2} = \Xi_{\mathrm{sfs}} = \left(1 + \frac{\Delta}{\Delta_{\mathrm{i}}}\right)^{\beta} = E_{\mathrm{F}}\,, \tag{3.4}$$

where s_{Tsfs} is the subfilter turbulent flame speed, A_{Δ} is the total flame surface area in the given box of size Δ, Ξ_{sfs} is the subfilter wrinkling factor, Δ_{i} is the inner cutoff scale, and β is the exponent of the power law expression, which is taken to be 0.5 in [79].

The inner cutoff is associated with the maximum thickness of the laminar flame thickness and the mean curvature of the flame. It can be defined as the inverse mean curvature of the flame,

$$\Delta_{\mathrm{i}} = |\langle \nabla \cdot \mathrm{n} \rangle_{\mathrm{s}}|^{-1}\,, \tag{3.5}$$

where n is the normal vector to the flame and $\langle \cdot \rangle_{\mathrm{s}}$ denotes filtering along the flame surface. The mean curvature is estimated by assuming an equilibrium between production and destruction of flame surface as

$$|\langle \nabla \cdot \mathrm{n} \rangle_{\mathrm{s}}| = \Delta^{-1}(u'_{\mathrm{sfs}}/s_{\mathrm{L}})\Gamma(\Delta/\delta_{\mathrm{L}}, u'_{\mathrm{sfs}}/s_{\mathrm{L}}, \mathrm{Re}_{\mathrm{sfs}})\,, \tag{3.6}$$

where Γ is the efficiency function proposed by Charlette*et al.* [79] to account for the net straining of all relevant scales smaller than Δ and $\mathrm{Re}_{\mathrm{sfs}}$ is the subfilter Reynolds number based on the subfilter-scale fluctuating velocity u'_{sfs}.

The thickened flame model has its obvious advantages over the other models. It is simple to implement and, due to the Arrhenius law, it may be possible to deal with

more complicated chemical kinetics and some effects associated with ignition and flame-wall interaction processes. The approach models both the reaction rate and subfilter transport terms simultaneously. The primary disadvantages of this model is related to the generally increased insensitivity of the modelled flame to the turbulence motions due to the artificial thickening of the flame brush.

3.1.2 G-equation Approach

The G-equation first introduced by Markstein [81] is based on the assumption that the flame is a thin surface and can be represented by the level surface of a scalar field, G. Yakhot [82] later suggested that the equation could be used for LES of combustion. Afterwards, there has been considerable interest in LES using the G-equation model [14].

The G-equation formalism adopts a view which is opposite to the thickened flame approach: the flame thickness is set to zero and the flame front is described as a propagating infinitely thin surface or interface that is tracked using a field variable, $\tilde{G}$ [16]. The resolved flame brush is related to the iso-level $\tilde{G} = \bar{G}_0$ and the filtered G-equation for $\tilde{G}$ is given by [83]

$$\frac{\partial \tilde{G}}{\partial t} + \frac{\partial \tilde{u}_i \tilde{G}}{\partial x_i} = s_{\mathrm{T}} |\nabla \tilde{G}| \,. \tag{3.7}$$

The challenge is then to find a model for the turbulent flame speed s_{T}. A closure for this term is often based on the subfilter-scale turbulence level $\tilde{u}'$ and given by an algebraic relation of the form

$$\frac{s_{\mathrm{T}}}{s_{\mathrm{L}}} = 1 + \alpha \Big(\frac{\tilde{u}'}{s_{\mathrm{T}}} \Big)^n , \tag{3.8}$$

where the $\tilde{u}'$ may be estimated in terms of the strain rate tensor and given by

$$\tilde{u}' = \Delta |\tilde{S}| = \Delta \sqrt{2 \tilde{S}_{ij} \tilde{S}_{ij}} \,. \tag{3.9}$$

The constants in Eq. 3.8 above, α and n, have to be specified a priori or may be dynamically determined [84].

The G-equation model is based on a flame front tracking technique, where displacement of the flame front is evaluated in terms of the displacement speed s_{T}. Since the flame speed is explicitly included, this leads to an estimation of the volume of burnt gases produced along with the thermal heat release [85]. On the other hand, there is no a well-defined quantity for the turbulent flame speed and no universal model is available. The numerical solution of the G-equation can introduce computation difficulties and induce flame cusps, which can be generally avoided by adding a diffusive term in Eq. 3.7. Nevertheless, the model is widely used and has been successfully applied to several practical problems [86, 87].

3.1.3 Flame Surface Density Model

As a third alternative to the modelling of turbulence/chemistry interaction, the flamelet assumption can be used to relate turbulent burning rate to the flame area or surface density. The latter can be estimated either through an algebraic closure or a modelled transport equation. The modelled transport equation for flame surface density was first applied to non-premixed turbulent combustion based on Coherent Flame Model (CFM) by Marble and Broadwell [88]. More recent studies have led to an exact transport equation for the FSD developed by Pope [44] and Candel and Poinsot [89] which is based on theoretical considerations for a propagating surface. Various RANS models based on original CFM model have been devised by Cant *et al.* [90], Maistret *et al.* [91], Candel *et al.* [92], Cheng and Diringer [93], Prasad and Gore [94], and Mantel and Borghi [95]. There also have been several DNS studies related to the flame surface density balance equation, including Trouvé and Poinsot [96], Haworth and Poinsot [97], Trouvé [98], Poinsot *et al.* [99, 100], Bruneaux *et al.* [101], Kollmann and Chen [102], Yeung *et al.* [103], and Pope *et al.* [104]. Moreover, Veynante *et al.* [105, 106] have analyzed the flame surface density balance equation from an experimental perspective. There has also been some research related to the application of the flame surface density concept in the context of LES for non-premixed combustion. In particular, Tap *et al.* [107] have extended the flame surface density concept to non-infinitely thin flame surfaces and application to autoignition of

turbulent non-premixed flames by introducing a generalized flame surface density. Nevertheless, for LES of premixed combustion, it is still at an early stage.

Hawkes and Cant [25] have developed an FSD model for LES of turbulent premixed flames which has shown considerable promise. The modelled transport equation for the FSD in the Hawkes and Cant model is based on previous RANS models, however, some terms that have been previously neglected in RANS-based FSD models can be significant for LES, and other terms require modification to be consistent with the LES philosophy. The FSD model, and in particular, the model of Hawkes and Cant is the focus of this thesis and a complete description of this flamelet based model now follows below.

3.2 Flame Surface Density Model

3.2.1 Progress of Reaction and Modelled Transport Equation for Progress Variable

Turbulent premixed flames are generally very thin with a flame thickness in the range $\delta_{\mathrm{L}} = 0.1$ mm–1.0 mm, which is in many cases smaller than the filter width, Δ. In the LES context, one approach to modelling of the flame is to ignore for the most part of its internal structure and the detailed chemical kinetics and represent the combustion occurring at the flame front in terms of a progress variable, which varies from 0 (for all reactants) to 1 (for all products). One possible definition of the progress variable, c, is provided in terms of the reduced fuel mass fraction given by

$$c = \frac{Y_{\mathrm{F}} - Y_{\mathrm{F}}^{\mathrm{u}}}{Y_{\mathrm{F}}^{\mathrm{b}} - Y_{\mathrm{F}}^{\mathrm{u}}}\,, \tag{3.10}$$

where Y_{F}, $Y_{\mathrm{F}}^{\mathrm{u}}$ and $Y_{\mathrm{F}}^{\mathrm{b}}$ are respectively the local, unburnt and burnt fuel mass fractions. In this way, the composition of the mixture can be specified by the progress variable. The location of the flame surface is defined by $c = c^*$. c is the local progress variable and c^* is the progress variable which represents the flame surface. Note that other choices for the progress variable are possible, including the reduced temperature.

The unfiltered transport equation for progress variable can be represented as

$$\frac{\partial}{\partial t}(\rho c) + \frac{\partial}{\partial x_i}(\rho u_i c) = \dot{\omega} + \frac{\partial}{\partial x_i}\Big(\rho D \frac{\partial c}{\partial x_i}\Big) = u_{\mathrm{p}} |\nabla c| \,. \tag{3.11}$$

Here, u_{p} is the local propagation speed of a constant progress variable surface.

The Favre-filtered transport equation for progress variable $\tilde{c}$ may be written as

$$\frac{\partial}{\partial t}(\bar{\rho}\tilde{c}) + \frac{\partial}{\partial x_i}(\bar{\rho}\tilde{u}_i\tilde{c}) + \frac{\partial}{\partial x_i}[\bar{\rho}(\widetilde{u_i c} - \tilde{u}_i\tilde{c})] = \bar{\dot{\omega}} + \overline{\frac{\partial}{\partial x_i}\Big(\rho D \frac{\partial c}{\partial x_i}\Big)} \,. \tag{3.12}$$

If the subfilter scalar transport term is represented with a gradient based transport approach model as described in Chapter 2, then

$$\frac{\partial}{\partial x_i}[\bar{\rho}(\widetilde{u_i c} - \tilde{u}_i\tilde{c})] = \frac{\partial}{\partial x_i}\Big(\frac{\bar{\rho}\nu_{\mathrm{t}}}{\mathrm{Sc_t}} \frac{\partial \tilde{c}}{\partial x_i}\Big) \,, \tag{3.13}$$

and the unclosed reaction and diffusion terms can be combined and written as

$$\bar{\dot{\omega}} + \overline{\nabla(\rho D \nabla c)} = \overline{\rho u_{\mathrm{p}} |\nabla c|} = \int_0^1 \overline{(\rho u_{\mathrm{p}})_{\mathrm{s}}} \Sigma_{\mathrm{sfs}} \mathrm{d}c^* \,, \tag{3.14}$$

where Σ_{sfs} is filtered flame surface density which is essentially the flame surface area per unit volume contained within the LES filtering volume. The detailed theory and modelled transport equation for FSD will be given in sections 3.2.3, 3.2.4, and 3.2.5 of this chapter.

For very thin flames, $\overline{(\rho u_{\mathrm{p}})_{\mathrm{s}}}$ and Σ_{sfs} are independent of the choice of c^* and the following approximation can be made:

$$\int_0^1 \overline{(\rho u_{\mathrm{p}})_{\mathrm{s}}} \Sigma_{\mathrm{sfs}} \mathrm{d}c^* \approx \overline{(\rho u_{\mathrm{p}})_{\mathrm{s}}} \tilde{\Sigma} \approx \rho_{\mathrm{r}} s_{\mathrm{L}} \Sigma_{\mathrm{sfs}} \,, \tag{3.15}$$

where ρ_{r} is the reactants density. For practical purposes, $\overline{(\rho u_{\mathrm{p}})_{\mathrm{s}}}$ maybe approximated by $\rho_{\mathrm{r}} s_{\mathrm{L}}$. This is based on continuity considerations, assuming the flame front can be locally represented by a steady one-dimensional laminar flame. Boger *et al.* [108] presented a validation of the approximation $\rho_{\mathrm{r}} s_{\mathrm{L}}$, through LES filtering of results from a DNS simulation of premixed combustion. The results showed a good agreement between the filtered reaction-diffusion term, $\overline{\nabla \cdot (\rho D \nabla c) + \dot{\omega}}$, and the corresponding FSD model, $\rho_{\mathrm{r}} s_{\mathrm{L}} \Sigma_{\mathrm{sfs}}$.

To summarize, the modelled transport equation for filtered progress variable, $\tilde{c}$, can be expressed as

$$\frac{\partial}{\partial t}(\bar{\rho}\tilde{c}) + \frac{\partial}{\partial x_i}(\bar{\rho}\tilde{u}_i\tilde{c}) = \frac{\partial}{\partial x_i}\Big(\frac{\bar{\rho}\nu_\mathrm{t}}{\mathrm{Sc_t}}\frac{\partial \tilde{c}}{\partial x_i}\Big) + \rho_\mathrm{r} s_\mathrm{L}\Sigma_\mathrm{sfs}\,. \tag{3.16}$$

In order to determine Σ_sfs, two possible approaches include use of an algebraic model or the use of a transport equation. The details of these two approaches will be discussed in sections 3.2.4 and 3.2.5.

3.2.2 Reaction Scheme

In this thesis, the primary interest is in methane-air flames, which was used in the experimental research by Yuen and Gülder [4, 5]. The following stoichiometric equation is assumed to represent the overall reaction:

$$\mathrm{CH_4} + 2(\mathrm{O_2} + 3.76\mathrm{N_2}) \rightarrow \mathrm{CO_2} + 2\mathrm{H_2O} + 7.52\mathrm{N_2}\,. \tag{3.17}$$

The five species considered here are methane (CH_4), oxygen (O_2), carbon dioxide (CO_2), water(H_2O), and nitrogen (N_2). Nitrogen is assumed to be inert. In this research, the mass fraction of each species is not given by solving transport equations for species mass fraction, it is derived based on the stoichiometric equation above and the definition of progress variable (Eq. 3.10) as follows:

$$Y_{\mathrm{CH_4}} = Y^\mathrm{u}_{\mathrm{CH_4}} + (Y^\mathrm{b}_{\mathrm{CH_4}} - Y^\mathrm{u}_{\mathrm{CH_4}})c\,, \tag{3.18}$$

$$Y_{\mathrm{O_2}} = Y_{\mathrm{CH_4}}\frac{(O/F)_\mathrm{st}}{\phi}\,, \tag{3.19}$$

$$Y_{\mathrm{CO_2}} = (1 - Y_{\mathrm{CH_4}} - Y_{\mathrm{O_2}} - Y_{\mathrm{N_2}})\frac{\mathcal{N}_{\mathrm{CO_2}}}{\mathcal{N}_{\mathrm{CO_2}} + 2\mathcal{N}_{\mathrm{H_2O}}}\,, \tag{3.20}$$

$$Y_{\mathrm{H_2O}} = (1 - Y_{\mathrm{CH_4}} - Y_{\mathrm{O_2}} - Y_{\mathrm{N_2}})\frac{2\mathcal{N}_{\mathrm{H_2O}}}{\mathcal{N}_{\mathrm{CO_2}} + 2\mathcal{N}_{\mathrm{H_2O}}}\,, \tag{3.21}$$

$$Y_{\mathrm{N_2}} = \frac{7.52\mathcal{N}_{\mathrm{N_2}}}{\phi\mathcal{N}_{\mathrm{CH_4}}}\Big/(1 + \frac{(O/F)_\mathrm{st}}{\phi} + \frac{7.52\mathcal{N}_{\mathrm{N_2}}}{\phi\mathcal{N}_{\mathrm{CH_4}}})\,, \tag{3.22}$$

where $(O/F)_\mathrm{st}$ is stoichoimetric ratio, ϕ is equivalence ratio, and $\mathcal{N}_i$ is species molecular weight.

One of the advantages of FSD transport equation model is that it is easy to apply this model to different fuels. All that is required is the calculation of the laminar flame speed and relationships for the mass fraction of the various reactants and products in terms of the progress variable. In the current research work, in addition to methane-air, similar stoichiometric reactions are assumed for propane-air, and hydrogen-air as follows:

$$C_3H_8 + 5O_2 + 3.76N_2 \rightarrow 3CO_2 + 4H_2O + 3.76N_2\,, \tag{3.23}$$

$$2H_2 + O_2 + 3.76N_2 \rightarrow 2H_2O + 3.76N_2\,. \tag{3.24}$$

3.2.3 Theory of Flame Surface Density

The concept of the flame surface density has been reviewed extensively in previous papers by Marble and Broadwell [88], Pope [44], Bray *et al.* [109], and Candel *et al.* [89]. The definition taken here is the flame area per unit volume of the surface at which $c = c^*$, where c is the local progress variable and c^* is the progress variable which represents the flame surface. Theoretically, from Pope's [44] approach, let the points $\mathrm{X}[u, v, t]$ represent the flame surface (defined by $c = c^*$), where $u, v \in U$ are local coordinates parameterizing the surface. Then the flame surface to volume ratio, $\Sigma(c^*; \mathrm{x}, t)$, is defined by

$$\Sigma(c^*; \mathrm{x}, t) \equiv \int\int_U \delta(\mathrm{x} - \mathrm{X}[u, v, t]) A(u, v, t) \mathrm{d}u\mathrm{d}v\,, \tag{3.25}$$

where,

$$A(u, v, t) \equiv \left| \frac{\partial \mathrm{X}}{\partial u} \times \frac{\partial \mathrm{X}}{\partial v} \right|. \tag{3.26}$$

Here $A(u, v, t)\mathrm{d}u\mathrm{d}v$ represents a differential element of area, and thus the integral over a volume of interest of Σ gives the instantaneous flame surface area within that volume.

The flame surface density for LES can be defined in terms of the filtered flame surface density, Σ_{sfs}, and is formally related to $\Sigma(c^*; \mathrm{x}, t)$ by

$$\Sigma_{\mathrm{sfs}} = \bar{\Sigma}. \tag{3.27}$$

In order to discuss the closure of the filtered progress variable equation with filtered flame surface density, it is more convenient to take the definition of the flame surface density from Vervisch *et al.* [110] as the LES filtered conditional gradient of the progress variable at the flame surface, $c=c^*$:

$$\Sigma_{\text{sfs}} = \overline{|\nabla c|\delta(c^* - c)}\,. \tag{3.28}$$

The following sections 3.2.4 and 3.2.5 will discuss the details of the two approaches for modelling the subfilter flame surface density, Σ_{sfs}, algebraic model and transport equation.

3.2.4 Algebraic Models

Algebraic LES models for the FSD have been developed on the basis of the earlier-derived RANS model. Boger *et al.* [108] suggested a simple formulation similar to Eddy-Break-Up (EBU) and Bray-Moss-Libby (BML) models for RANS

$$\Sigma_{\text{sfs}} = K_\Sigma \frac{\tilde{c}(1-\tilde{c})}{\Delta}\,. \tag{3.29}$$

Here K_Σ is a model constant. Boger *et al.* [108] calculated a value as $4\sqrt{6/\pi}$ for K_Σ based on an infinitely thin planar flame and a Gaussian LES filter. It has been also shown that K_Σ depends on filter width Δ and turbulence level, but is independent of the observation time.

Charlette *et al.* [79] presented the following model for Σ_{sfs}, which also bears similarities to EBU and BML expressions, but includes a term that accounts for the resolved part of the flame surface density:

$$\Sigma_{\text{sfs}} = |\nabla\tilde{c}| + \alpha\Gamma_{\text{k}}\Big(\frac{\delta_{\text{L}}}{\Delta}, \frac{\sqrt{2\tilde{k}/3}}{s_{\text{L}}}\Big)\frac{\sqrt{\tilde{k}}}{s_{\text{L}}}\frac{\tilde{c}(1-\tilde{c})}{\Delta}\,. \tag{3.30}$$

Here Γ_{k} is the efficiency function of the Intermittent Turbulence Net Flame Stretch (ITNFS) model of Meneveau and Poinsot [111], $\tilde{k}$ represents the subfilter-scale turbulent kinetic energy, and α is a model constant.

Angelberger *et al.* [41] have also proposed an algebraic model for the resolved and subfilter FSD which has the form

$$\Sigma_{\rm sfs} = [1 + \alpha\Gamma\Big(\frac{\delta_{\rm L}}{\Delta}, \frac{u'}{s_{\rm L}}\Big)\frac{u'}{s_{\rm L}}]|\nabla\tilde{c}|\,, \tag{3.31}$$

where the function Γ is similar to the ITNFS efficiency function, $\Gamma_{\rm k}$.

More complete discussion of algebraic LES models for the FSD are given by Boger *et al.* [108], and Hawkes [25]. Generally, algebraic models are simple and sufficient for treating situations where there is a local balance between the production and dissipation of the FSD at the flame front. However, for unsteady situations, the complicated dynamics of flame stretch can not be completely represented by a simple algebraic model. Dynamic model constants could be developed based on the physical arguments and DNS data, or using the dynamic approach proposed by Germano *et al.* [60, 68]. A more realistic estimation for LES FSD modelling can be provided by adopting a modelled transport equation for the FSD. This will be discussed next.

3.2.5 Modelled Transport Equation for FSD

Originally, the concept of solving a modelled transport equation for flame surface density was applied to the non-premixed turbulent combustion by Marble and Broadwell [88]. Since then, there have been many studies of the approach in turbulent premixed combustion. Marble and Broadwell employed the coherent flame model to describe the physical processes that create and destroy flame surface area. More recent studies have led to an exact transport equation for the flame surface density based on theoretical considerations for a propagating surface as given by Pope [44] and Candel *et al.* and Poinsot [89].

A conservation equation for flame surface density can be derived by using an approach similar to that of Pope [44]. In order to show the equation in a conservation formulation, the flame surface density variable used herein is taken the form as the FSD per unit mass, $\tilde{\Sigma} = \Sigma_{\rm sfs}/\bar{\rho}$. The following Favre-filtered form may be derived for

the unclosed transport equation:

$$\frac{\partial}{\partial t}(\bar{\rho}\tilde{\Sigma}) + \frac{\partial}{\partial x_i}(\bar{\rho}\tilde{\Sigma}\tilde{u}_i) + \frac{\partial}{\partial x_i}\bar{\rho}\tilde{\Sigma}[\overline{(u_i)}_{\rm s} - \tilde{u}_i] = \overline{(\alpha_{\rm T})}_{\rm s}\bar{\rho}\tilde{\Sigma} - \frac{\partial}{\partial x_i}[\overline{(u_{\rm p}N_i)}_{\rm s}\bar{\rho}\tilde{\Sigma}] + \overline{\left(u_{\rm p}\frac{\partial N_i}{\partial x_i}\right)}_{\rm s}\bar{\rho}\tilde{\Sigma}\,, \tag{3.32}$$

where $[\overline{(u_i)}_{\rm s} - \tilde{u}_i]$ is the subfilter flux of FSD, $\mathbf{N} = -\nabla c/|\nabla c|$ is the local flame surface normal pointing into the reactants, $(\alpha_{\rm T})_{\rm s}$ is the surface strain and given by

$$\overline{(\alpha_{\rm T})_{\rm s}} = \overline{\left[(\delta_{ij} - N_i N_j)\frac{\partial u_i}{\partial x_j}\right]_{\rm s}}\,. \tag{3.33}$$

A more detailed derivation of this unclosed transport equation is given by both Pope [44] and Hawkes [25].

Each term in Eq. 3.32 above has an associated physical meaning. On the left-hand side is a net rate of change, a resolved flow convection, and a subfilter convection. On the right-hand side is a fluid strain, a planar propagation, and production or destruction of FSD [25].

There has been a considerable research on RANS modelling of the FSD transport equation (Eq. 3.32) [94, 112]. More recently, Hawkes and Cant [25] have suggested an approach to the modelling for LES that resembles in many respects the RANS models, but also includes terms that account for the resolved components of FSD production and destruction. The following sections will present the details of the modelled terms proposed by Hawkes and Cant [25].

3.2.6 Modelling of Propagation and Curvature

In the unclosed FSD transport equation given above, the last two terms on the RHS, $-\nabla\cdot[\overline{(u_{\rm p}{\rm N})}_{\rm s}\bar{\rho}\tilde{\Sigma}] + \overline{(u_{\rm p}\nabla\cdot{\rm N})}_{\rm s}\bar{\rho}\tilde{\Sigma}$, represent the propagation and the production or destruction of FSD due to the combined effects of curvature and propagation. Based on the assumption of constant propagation speed, $u_{\rm p}$, at the subfilter-scale level, the resolved and subfilter-scale term may be expressed as

$$-\nabla\cdot[\overline{(u_{\rm p}{\rm N})}_{\rm s}\bar{\rho}\tilde{\Sigma}] + \overline{(u_{\rm p}\nabla\cdot{\rm N})}_{\rm s}\bar{\rho}\tilde{\Sigma} = {\rm P}_{\rm res} + {\rm C}_{\rm res} + {\rm C}_{\rm sfs}\,, \tag{3.34}$$

where

$$\mathrm{P_{res}} = -\nabla \cdot [\overline{(u_\mathrm{p})_\mathrm{s}}\ \overline{(\mathrm{N})_\mathrm{s}}\bar{\rho}\tilde{\Sigma}]\,, \tag{3.35}$$

$$\mathrm{C_{res}} = \overline{(u_\mathrm{p})_\mathrm{s}}\,\nabla \cdot \overline{(\mathrm{N})_\mathrm{s}}\bar{\rho}\tilde{\Sigma}\,, \tag{3.36}$$

and

$$\mathrm{C_{sfs}} = -\overline{(u_\mathrm{p})_\mathrm{s}}[\nabla \cdot \overline{(\mathrm{N})_\mathrm{s}} - \overline{(\nabla \cdot \mathrm{N_s})}]\bar{\rho}\tilde{\Sigma}\,. \tag{3.37}$$

The terms P_res and C_res represent the resolved component of planar propagation and curvature, respectively. The term C_sfs represents the difference between the actual curvature and the resolved curvature. The mean propagation speed, $\overline{(u_\mathrm{p})_\mathrm{s}}$, may be estimated by using conservation of mass and introducing the heat release parameter, τ, for a one dimensional steady premixed laminar flame as follows

$$\rho u_\mathrm{p} = \rho_\mathrm{r} s_\mathrm{L}\,, \qquad \tau = \frac{T_\mathrm{ad} - T_\mathrm{r}}{T_\mathrm{r}}\,, \qquad \rho = \frac{\rho_\mathrm{r}}{1+\tau c}\,, \tag{3.38}$$

where c can be expressed as the reduced temperature given by $c = (T - T_\mathrm{r})/(T_\mathrm{ad} - T_\mathrm{r})$. The propagation speed may be written as

$$\overline{(u_\mathrm{p})_\mathrm{s}} \approx \overline{s_\mathrm{L}(1+\tau c)_\mathrm{s}} = s_\mathrm{L}(1+\tau c^*)\,. \tag{3.39}$$

The forms for $\mathrm{P_{res}}$ and $\mathrm{C_{res}}$ suggested by Hawkes and Cant [25] are employed herein where $\mathrm{P_{res}}$ and $\mathrm{C_{res}}$ are given by

$$\mathrm{P_{res}} = -\frac{\partial}{\partial x_i}[s_\mathrm{L}(1+\tau c^*)N_i\bar{\rho}\tilde{\Sigma}]\,, \tag{3.40}$$

$$\mathrm{C_{res}} = s_\mathrm{L}(1+\tau c^*)\frac{\partial N_i}{\partial x_i}\bar{\rho}\tilde{\Sigma}\,, \tag{3.41}$$

and where the surface averaged normal is evaluated as $\overline{(\mathrm{N})_\mathrm{s}} = -\nabla\bar{c}/(\bar{\rho}\tilde{\Sigma})$.

There are several RANS models that can be adopted for modelling the subfilter curvature term given by Pope and Cheng [44], Trouvé and Poinsot [98], Veynante [105], Charlette *et al.* [79]. In this research, the following model proposed by Cant [25] is used for the modelling of $\mathrm{C_{sfs}}$, which includes the resolution factor α in order to make the model vanish as the flow becomes resolved. This model resembles the commonly employed CFM model proposed by Candel *et al.* [92] and has the form

$$\mathrm{C_{sfs}} = -\alpha\beta s_\mathrm{L}\frac{(\bar{\rho}\tilde{\Sigma})^2}{1-\bar{c}}\,, \tag{3.42}$$

where α is the resolution factor and β is the model constant.

3.2.7 Modelling of Strain Term

The term $\overline{(\alpha_{\mathrm{T}})_{\mathrm{s}}}\bar{\rho}\tilde{\Sigma}$ appearing in Eq. 3.32 represents the straining effect of the surrounding fluid on the flame surface. Considerable attention has been devoted to the modelling of the effects of fluid strain, see e.g., Cant *et al.* [90], Yeung *et al.* [103], and Trouvé and Poinsot [98]. The term $\overline{(\alpha_{\mathrm{T}})_{\mathrm{s}}}$ may be decomposed as follows:

$$\overline{(\alpha_{\mathrm{T}})_{\mathrm{s}}} = \mathrm{S}_{\mathrm{res}} + \mathrm{S}_{\mathrm{hr}} + \mathrm{S}_{\mathrm{sfs}}\,, \tag{3.43}$$

where the resolved strain term, $\mathrm{S}_{\mathrm{res}}$, is evaluated using

$$\mathrm{S}_{\mathrm{res}} = (\delta_{ij} - n_{ij})\frac{\partial \tilde{u}_i}{\partial x_j}\,, \tag{3.44}$$

and n_{ij} is a model for the surface statistic $\overline{(N_i N_j)_{\mathrm{s}}}$, which acts as an orientation factor for the flame strain with respect to the resolved flow gradients. The following model proposed by Cant *et al.* [90] for $\overline{(N_i N_j)_{\mathrm{s}}}$ is employed in the present work:

$$n_{ij} = \overline{(N_i)_{\mathrm{s}}}\,\overline{(N_j)_{\mathrm{s}}} + \frac{1}{3}\alpha\delta_{ij}\,. \tag{3.45}$$

The heat release, S_{hr}, is a term that accounts for the expansion effects associated with heat release and also affects the resolved production as well as the resolved planar propagation terms and is modelled using an adjustment to the resolved curvature effect by

$$\mathrm{S}_{\mathrm{hr}} = -(c^* - \tilde{c})\tau s_{\mathrm{L}}\nabla\cdot\overline{(\mathrm{N})_{\mathrm{s}}}\,. \tag{3.46}$$

The modelling of the subfilter strain term, $\mathrm{S}_{\mathrm{sfs}}$, adapted by Hawkes and Cant [25] is to reproduce the effects of chemistry and turbulence length scales by ITNFS model of Meneveau and Poinsot [111] and is given by

$$\mathrm{S}_{\mathrm{sfs}} = \Gamma_{\mathrm{k}}\frac{\sqrt{\tilde{k}}}{\Delta}\,, \tag{3.47}$$

where the efficiency function Γ_{k} is implemented using the curve fitted form of Angelberger *et al.* [41] given by

$$\Gamma_{\mathrm{k}}\Big(\frac{\Delta}{\delta_{\mathrm{L}}}, \frac{u'}{s_{\mathrm{L}}}\Big) = 0.75\exp\Big[-\frac{1.2}{(u'/s_{\mathrm{L}})^{0.3}}\Big]\Big(\frac{\Delta}{\delta_{\mathrm{L}}}\Big)^{2/3}\,. \tag{3.48}$$

3.2.8 Modelling of Turbulent Transport Term

The term $\overline{(u_i)_{\rm s}} - \tilde{u}_i$ on the LHS of Eq. 3.32 may be interpreted as the subfilter-scale flux of the FSD. This term is strongly connected with the subfilter-scale flux of the progress variable given by $\widetilde{uc} - \tilde{u}\tilde{c}$. This statement has been theoretically proved by Cant *et al.* [90] with the relation between the RANS equivalents of these two terms and the analysis of the DNS results by Veynante *et al.* [113]. The scalar fluxes of the progress variable and the flame surface density are found to be controlled mainly by non-gradient transport (NGT) mechanisms. It is expected that NGT to be the most dominant when the turbulence levels are low and there is a large expansion associated with heat release. Based on these ideas, the following model is applied for the turbulent transport term, $\overline{(u_i)_{\rm s}} - \tilde{u}_i$, due to the heat release and the non-gradient transport mechanisms:

$$\overline{(u_i)_{\rm s}} - \tilde{u}_i = {\rm S_{hr}} - \frac{\nu_{\rm t}}{{\rm Sc_t}} \frac{1}{(\bar{\rho}\tilde{\Sigma})} \frac{\partial(\bar{\rho}\tilde{\Sigma})}{\partial x_i} \,. \tag{3.49}$$

The model of the turbulent transport term is similar to the model suggested by Veynante *et al.* [77], but differs in that the efficiency of the NGT is reduced with increased turbulence, instead of increasing the efficiency of gradient diffusion term. The proposed model reduces to the exact transport of the FSD for the case of a fully resolved, one-dimensional, incompressible flame with unity Lewis number.

3.2.9 Summary of Hawkes and Cant FSD Model

The modelled progress variable and flame surface density transport equations developed by Hawkes and Cant [25] can be summarized as

$$\frac{\partial}{\partial t}(\bar{\rho}\tilde{c}) + \frac{\partial}{\partial x_i}(\bar{\rho}\tilde{u}_i\tilde{c}) = \frac{\partial}{\partial x_i}\Big(\frac{\bar{\rho}\nu_{\rm t}}{{\rm Sc_t}}\frac{\partial \tilde{c}}{\partial x_i}\Big) + \rho_{\rm r} s_{\rm L} \bar{\rho}\tilde{\Sigma} \,, \tag{3.50}$$

$$\begin{aligned} \frac{\partial}{\partial t}(\bar{\rho}\tilde{\Sigma}) + \frac{\partial}{\partial x_i}(\bar{\rho}\tilde{\Sigma}\tilde{u}_i) \;\; = \;\; & -\frac{\partial}{\partial x_i}\bar{\rho}\tilde{\Sigma}[\overline{(u_i)}_{\rm s} - \tilde{u}_i] \\ & +({\rm S_{res}} + {\rm S_{hr}} + {\rm S_{sfs}})\bar{\rho}\tilde{\Sigma} \\ & +{\rm P_{res}} + {\rm C_{res}} + {\rm C_{sfs}} \,, \end{aligned} \tag{3.51}$$

where the various terms appearing in the modelled transport equation for $\tilde{\Sigma}$ are defined as follows [25]:

- the surface turbulent velocity fluctuation

$$\overline{(u_i)}_{\mathrm{s}} - \tilde{u}_i = -(c^* - \tilde{c})\tau s_{\mathrm{L}} N_i - \frac{1}{(\bar{\rho}\tilde{\Sigma})} \frac{\nu_{\mathrm{t}}}{\mathrm{Sc_t}} \frac{\partial(\bar{\rho}\tilde{\Sigma})}{\partial x_i}, \tag{3.52}$$

- the resolved strain source term

$$\mathrm{S_{res}} = (\delta_{ij} - n_{ij}) \frac{\partial \tilde{u}_i}{\partial x_j}, \tag{3.53}$$

- the heat release strain source term

$$\mathrm{S_{hr}} = -(c^* - \tilde{c})\tau s_{\mathrm{L}} \frac{\partial N_i}{\partial x_i}, \tag{3.54}$$

- the subfilter strain source term

$$\mathrm{S_{sfs}} = \Gamma_{\mathrm{k}} \frac{\sqrt{\tilde{k}}}{\Delta}, \tag{3.55}$$

- the resolved propagation term

$$\mathrm{P_{res}} = \frac{\partial}{\partial x_i} [s_{\mathrm{L}}(1 + \tau c^*) N_i \bar{\rho}\tilde{\Sigma}], \tag{3.56}$$

- the resolved curvature term

$$\mathrm{C_{res}} = s_{\mathrm{L}}(1 + \tau c^*) \frac{\partial N_i}{\partial x_i} \bar{\rho}\tilde{\Sigma}, \tag{3.57}$$

- the subfilter curvature term

$$\mathrm{C_{sfs}} = -\alpha\beta s_{\mathrm{L}} \frac{(\bar{\rho}\tilde{\Sigma})^2}{1 - \tilde{c}}, \tag{3.58}$$

and where β is a user-determined model constant and must satisfy $\beta \geq 1$ for reasons of realisibility [43].

If we combine turbulent transport term, heat release strain term, and resolved propagation term together, and assume that on the flame front $c^* = \tilde{c}$, these terms can be re-written as

$$\begin{aligned} -\frac{\partial}{\partial x_i}\bar{\rho}\tilde{\Sigma}[\overline{(u_i)}_{\mathrm{s}} - \tilde{u}_i] + \mathrm{S_{hr}}\bar{\rho}\tilde{\Sigma} + \mathrm{P_{res}} + \mathrm{C_{res}} &= \frac{\partial}{\partial x_i}\Big(\frac{\bar{\rho}\nu_{\mathrm{t}}}{\mathrm{Sc_t}}\frac{\partial\tilde{\Sigma}}{\partial x_i}\Big) \\ &\quad -s_{\mathrm{L}}(1+\tau\tilde{c})N_i\frac{\partial(\bar{\rho}\tilde{\Sigma})}{\partial x_i} \\ &\quad -s_{\mathrm{L}}\tau N_i\bar{\rho}\tilde{\Sigma}\frac{\partial\tilde{c}}{\partial x_i}\,. \end{aligned} \tag{3.59}$$

Using the expression above, the final form of the modelled transport equation of flame surface density can be re-expressed as

$$\begin{aligned} \frac{\partial}{\partial t}(\bar{\rho}\tilde{\Sigma}) + \frac{\partial}{\partial x_i}(\bar{\rho}\tilde{\Sigma}\tilde{u}_i) &= \frac{\partial}{\partial x_i}\Big(\frac{\bar{\rho}\nu_{\mathrm{t}}}{\mathrm{Sc_t}}\frac{\partial\tilde{\Sigma}}{\partial x_i}\Big) + (\delta_{ij}-n_{ij})\frac{\partial\tilde{u}_i}{\partial x_j}\bar{\rho}\tilde{\Sigma} - s_{\mathrm{L}}(1+\tau\tilde{c})N_i\frac{\partial}{\partial x_i}(\bar{\rho}\tilde{\Sigma}) \\ &\quad -s_{\mathrm{L}}\tau N_i\bar{\rho}\tilde{\Sigma}\frac{\partial\tilde{c}}{\partial x_i} + \Gamma_{\mathrm{k}}\frac{\sqrt{\tilde{k}}}{\Delta}\bar{\rho}\tilde{\Sigma} - \alpha\beta s_{\mathrm{L}}\frac{(\bar{\rho}\tilde{\Sigma})^2}{1-\tilde{c}}\,, \end{aligned} \tag{3.60}$$

where $\bar{c}$ can be estimated using

$$\bar{c} = \frac{(1+\tau)\tilde{c}}{1+\tau\tilde{c}}\,. \tag{3.61}$$

The complete set of modelled equations include Eq. 3.50 and Eq. 3.60, modelled transport equations for progress variable and flame surface density, respectively.

According to the LES concept, the modelled transport equations, as far as possible, should give reasonable results regardless of the choice of filter width Δ. This leads to two important considerations for the models. Firstly, the transport equation should revert to the exact closed transport equation as the scalar and velocity fields become fully resolved in which the subfilter-scale fluxes of momentum vanish and Δ is much smaller than the radius of curvature of the flame surface. Secondly, the model should reflect accepted RANS models for a situation in which Δ becomes comparable to the turbulence integral scale. The modelled terms in the transport equations of c and Σ by Hawkes [25] have displayed these two essential LES requirements. A more detailed discussion of the physical interpretation and realisability arguments for the FSD model considered in this study is given by Hawkes [25].

Chapter 4

Parallel Adaptive Mesh Refinement Finite-Volume Scheme

The Favre-filtered governing equations (Eq. 2.6, Eq. 2.7, and Eq. 2.8) described in Chapter 2 together with the filtered transport equations (Eq. 2.37, Eq. 3.50, and Eq. 3.60) introduced in Chapters 2 and 3 provide a suitable description for carrying out LES predictions of the physical and chemical processes that occur in a premixed turbulent flame. A parallel adaptive mesh refinement finite volume method is now proposed, developed, and reviewed in this chapter for the numerical solution of the filtered equation set.

This thesis work has involved the development of both a two- and a three-dimensional LES framework for solving multi-species turbulent reacting flows applied to the compressible form of the Navier-Stokes governing equations, which included the transport equations for FSD model, two-dimensional AMR application for FSD model, three-dimensional turbulence field initialization and thickened flame model, and processing of the comparison of LES-FSD simulation results to the experimental data.

4.1 Favre-Filtered Governing Equations

The Favre-filtered governing equations for LES of premixed turbulent flames introduced in the previous chapters can be expressed using matrix-vector notation in

the following form:

$$\frac{\partial \mathbf{U}}{\partial t} + \vec{\nabla} \cdot \vec{\mathbf{F}} = \mathbf{S}, \tag{4.1}$$

where $\mathbf{U}$ represents the vector of conserved variables, $\vec{\mathbf{F}}$ is the flux dyad, and $\mathbf{S}$ is the source term. The flux dyad $\vec{\mathbf{F}}$ can be decomposed into an inviscid component, $\vec{\mathbf{F}}_\mathbf{I}$, and a viscous component, $\vec{\mathbf{F}}_\mathbf{V}$, and can thus be written as

$$\begin{aligned} \vec{\mathbf{F}} &= \vec{\mathbf{F}}_\mathbf{I} + \vec{\mathbf{F}}_\mathbf{V} \\ &= (\mathbf{F}_\mathbf{I} - \mathbf{F}_\mathbf{V}, \mathbf{G}_\mathbf{I} - \mathbf{G}_\mathbf{V}, \mathbf{H}_\mathbf{I} - \mathbf{H}_\mathbf{V}), \end{aligned} \tag{4.2}$$

where $\mathbf{F}_\mathbf{I}$, $\mathbf{F}_\mathbf{V}$, $\mathbf{G}_\mathbf{I}$, $\mathbf{G}_\mathbf{V}$, $\mathbf{H}_\mathbf{I}$, and $\mathbf{H}_\mathbf{V}$ are the components of inviscid and viscous flux vectors in the x-, y-, and z-coordinate directions, respectively. The vectors $\mathbf{U}$, $\mathbf{F}_\mathbf{I}$, $\mathbf{F}_\mathbf{V}$, $\mathbf{G}_\mathbf{I}$, $\mathbf{G}_\mathbf{V}$, $\mathbf{H}_\mathbf{I}$, $\mathbf{H}_\mathbf{V}$, and $\mathbf{S}$ can be expressed as

$$\mathbf{U} = \begin{pmatrix} \bar{\rho} \\ \bar{\rho}\tilde{u} \\ \bar{\rho}\tilde{v} \\ \bar{\rho}\tilde{w} \\ \bar{\rho}\tilde{E} \\ \bar{\rho}\tilde{c} \\ \bar{\rho}\tilde{\Sigma} \\ \bar{\rho}\tilde{k} \end{pmatrix}, \tag{4.3}$$

$$\mathbf{F}_\mathbf{I} = \begin{pmatrix} \bar{\rho}\tilde{u} \\ \bar{\rho}\tilde{u}\tilde{u} + \bar{p} \\ \bar{\rho}\tilde{u}\tilde{v} \\ \bar{\rho}\tilde{u}\tilde{w} \\ (\bar{\rho}\tilde{E} + \bar{p})\tilde{u} \\ \bar{\rho}\tilde{c}\tilde{u} \\ \bar{\rho}\tilde{\Sigma}\tilde{u} \\ \bar{\rho}\tilde{k}\tilde{u} \end{pmatrix}, \quad \mathbf{G}_\mathbf{I} = \begin{pmatrix} \bar{\rho}\tilde{v} \\ \bar{\rho}\tilde{u}\tilde{v} \\ \bar{\rho}\tilde{v}\tilde{v} + \bar{p} \\ \bar{\rho}\tilde{v}\tilde{w} \\ (\bar{\rho}\tilde{E} + \bar{p})\tilde{v} \\ \bar{\rho}\tilde{c}\tilde{v} \\ \bar{\rho}\tilde{\Sigma}\tilde{v} \\ \bar{\rho}\tilde{k}\tilde{v} \end{pmatrix}, \quad \mathbf{H}_\mathbf{I} = \begin{pmatrix} \bar{\rho}\tilde{w} \\ \bar{\rho}\tilde{u}\tilde{w} \\ \bar{\rho}\tilde{v}\tilde{w} \\ \bar{\rho}\tilde{w}\tilde{w} + \bar{p} \\ (\bar{\rho}\tilde{E} + \bar{p})\tilde{w} \\ \bar{\rho}\tilde{c}\tilde{w} \\ \bar{\rho}\tilde{\Sigma}\tilde{w} \\ \bar{\rho}\tilde{k}\tilde{w} \end{pmatrix}, \tag{4.4}$$

$$\mathbf{F_V} = \begin{pmatrix} 0 \\ \check{\tau}_{xx} + \sigma_{xx} \\ \check{\tau}_{xy} + \sigma_{xy} \\ \check{\tau}_{xz} + \sigma_{xz} \\ \tilde{u}(\check{\tau}_{xx} + \sigma_{xx}) + \tilde{v}(\check{\tau}_{xy} + \sigma_{xy}) + \tilde{w}(\check{\tau}_{xz} + \sigma_{xz}) - (\check{q}_x + \theta_x) \\ \frac{\bar{\rho}\nu_\mathrm{t}}{\mathrm{Sc_t}} \frac{\partial \tilde{c}}{\partial x} \\ \frac{\bar{\rho}\nu_\mathrm{t}}{\mathrm{Sc_t}} \frac{\partial \tilde{\Sigma}}{\partial x} \\ \bar{\rho}(\frac{\nu_\mathrm{t}}{\mathrm{Pr_t}} + \nu) \frac{\partial \tilde{k}}{\partial x} \end{pmatrix}, \tag{4.5}$$

$$\mathbf{G_V} = \begin{pmatrix} 0 \\ \check{\tau}_{xy} + \sigma_{xy} \\ \check{\tau}_{yy} + \sigma_{yy} \\ \check{\tau}_{yz} + \sigma_{yz} \\ \tilde{u}(\check{\tau}_{xy} + \sigma_{xy}) + \tilde{v}(\check{\tau}_{yy} + \sigma_{yy}) + \tilde{w}(\check{\tau}_{yz} + \sigma_{yz}) - (\check{q}_y + \theta_y) \\ \frac{\bar{\rho}\nu_\mathrm{t}}{\mathrm{Sc_t}} \frac{\partial \tilde{c}}{\partial y} \\ \frac{\bar{\rho}\nu_\mathrm{t}}{\mathrm{Sc_t}} \frac{\partial \tilde{\Sigma}}{\partial y} \\ \bar{\rho}(\frac{\nu_\mathrm{t}}{\mathrm{Pr_t}} + \nu) \frac{\partial \tilde{k}}{\partial y} \end{pmatrix}, \tag{4.6}$$

$$\mathbf{H_V} = \begin{pmatrix} 0 \\ \check{\tau}_{xz} + \sigma_{xz} \\ \check{\tau}_{yz} + \sigma_{yz} \\ \check{\tau}_{zz} + \sigma_{zz} \\ \tilde{u}(\check{\tau}_{xz} + \sigma_{xz}) + \tilde{v}(\check{\tau}_{yz} + \sigma_{yz}) + \tilde{w}(\check{\tau}_{zz} + \sigma_{zz}) - (\check{q}_z + \theta_z) \\ \frac{\bar{\rho}\nu_\mathrm{t}}{\mathrm{Sc_t}} \frac{\partial \tilde{c}}{\partial z} \\ \frac{\bar{\rho}\nu_\mathrm{t}}{\mathrm{Sc_t}} \frac{\partial \tilde{\Sigma}}{\partial z} \\ \bar{\rho}(\frac{\nu_\mathrm{t}}{\mathrm{Pr_t}} + \nu) \frac{\partial \tilde{k}}{\partial z} \end{pmatrix}, \tag{4.7}$$

$$\mathbf{S} = \begin{pmatrix} 0 \\ 0 \\ 0 \\ 0 \\ 0 \\ \dot{\bar{\omega}} \\ \tilde{S}_{\Sigma 1} + \tilde{S}_{\Sigma 2} + \tilde{S}_{\Sigma 3} + \tilde{S}_{\Sigma 4} + \tilde{S}_{\Sigma 5} \\ \tilde{S}_k \end{pmatrix}. \tag{4.8}$$

The source vector, $\mathbf{S}$, contains terms related to the chemistry and turbulence modelling which have been discussed in previous chapters. Detailed expressions for these terms are given in Appendix A.

4.2 Godunov Finite-Volume Method

4.2.1 Finite-Volume Formulation of Governing Equations

The integral form of the preceding governing equations can be derived by integrating the differential form of the equations over a volume, V, and applying the divergence theorem. The following integral expression is obtained from Eq. 4.1

$$\frac{\mathrm{d}}{\mathrm{d}t}\int_{V(t)} \mathbf{U}\mathrm{d}V + \oint_{S(t)} \mathbf{n}\cdot\vec{\mathbf{F}}\mathrm{d}S = \int_{V(t)} \mathbf{S}\mathrm{d}V, \tag{4.9}$$

where V is the control volume, S is the closed surface of the control volume, and $\mathbf{n}$ is the unit outward vector normal to the closed surface. The averaged value of $\mathbf{U}$ and of $\mathbf{S}$ for the control volume can be defined by the volume integrations as follows:

$$\overline{\mathbf{U}} = \frac{1}{V}\int_{V(t)} \mathbf{U}\mathrm{d}V, \tag{4.10}$$

$$\overline{\mathbf{S}} = \frac{1}{V}\int_{V(t)} \mathbf{S}\mathrm{d}V. \tag{4.11}$$

Eq. 4.9 can then be rewritten using 4.10 and 4.11. This leads to the following system of coupled integral equations for volume-averaged quantities

$$\frac{\mathrm{d}\overline{\mathbf{U}}}{\mathrm{d}t} = -\frac{1}{V}\oint_{S(t)} \mathbf{n}\cdot\vec{\mathbf{F}}\mathrm{d}S + \overline{\mathbf{S}}. \tag{4.12}$$

When the integral equation above is applied to a three-dimensional control volume in a structured multi-block mesh consisting of hexahedral cells, Eq. 4.12 can be re-written for each computational cell (i,j,k) as

$$\frac{\mathrm{d}\overline{\mathbf{U}}_{i,j,k}}{\mathrm{d}t} = -\frac{1}{V_{i,j,k}}\sum_{l=1}^{N_f}\left[\vec{n}_l\cdot\vec{\mathbf{F}}_l A_l\right]_{i,j,k} + \overline{\mathbf{S}}_{i,j,k}(\overline{\mathbf{U}}) = \overline{\mathbf{R}}_{i,j,k}(\overline{\mathbf{U}}), \tag{4.13}$$

where N_f denotes the number of cell faces, A_l is the surface area of face l, and $\mathbf{R}$ is the residual operator for the control volume (i,j,k). The semi-discrete form represented by Eq. 4.13 is a set of coupled non-linear ordinary differential equations for cell-averaged quantities, $\overline{U}_{i,j,k}$, which can be solved by evaluation of the flux integrals. The remainder of this chapter outlines various aspects of the finite-volume spatial discretization scheme proposed herein for the solution of the Favre-filtered equations governing a compressible, thermally perfect, reactive, premixed mixture in three space dimensions, including solution of Eq. 4.13 for the unsteady combusting turbulent flows of interest here.

4.2.2 Inviscid (Hyperbolic) Flux Evaluation

The finite-volume scheme defined above requires the evaluation of the solution fluxes at the cell faces. The inviscid fluxes are discretized by applying a Godunov-type upwind finite-volume spatial discretization procedure. Godunov-type finite-volume methods make use of the solution of a locally one-dimensional Riemann problem which provides a means for evaluating the numerical flux function at the cell boundaries. As first proposed by Godunov [114], the method is a monotonicity preserving scheme which is able to capture solution discontinuities, such as shocks, without introducing oscillations in the solutions. Solution of the Riemann problem also provides natural upwinding of the solution content. Exact Riemann solvers, such as the one proposed

by Gottlieb and Groth [115], can be used for the Euler equations for an ideal polytropic gas. The inviscid flux $\mathbf{F}$ between cell (i,j,k) and cell $(i+1,j,k)$ is then given at the cell interface $(i+\frac{1}{2},j,k)$ by

$$\vec{\mathbf{F}}_{i+\frac{1}{2},j,k}\cdot\vec{n}=\vec{\mathbf{F}}(\mathcal{R}(\mathbf{U}_{\mathrm{L}},\mathbf{U}_{\mathrm{R}}))=\vec{\mathbf{F}}(\mathcal{R}(\overline{\mathbf{U}}_{i,j,k},\overline{\mathbf{U}}_{i+1,j,k})), \tag{4.14}$$

where $\mathbf{U}_{\mathrm{L}}$ and $\mathbf{U}_{\mathrm{R}}$ are left and right vectors, respectively, and $\mathcal{R}$ represents the solution of the Riemann problem. A first-order accurate solution in space can be obtained by solving Riemann problems using the cell averages as the left and right states when evaluating the face fluxes. For higher-order accuracy, however, a spatial reconstruction of the solution in each computational cell is required which will be discussed in the following section. More efficient and tractable approximate Riemann solvers such as the Roe [116], Harten-Lax-van-Leer-Einfeldt (HLLE) [117] and Advection Upstream Splitting Method (AUSM$^+$-up) [118] approximate Riemann solvers can be used for dealing with more complicated systems such as those under consideration here, where experience has shown that the approximate approach does not decrease the accuracy of the overall solution scheme. In this thesis research, the AUSM$^+$-up approximate Riemann solver proposed by Liou [118] is used, as it is valid for a wide range of flow speeds and Mach numbers encountered in the premixed turbulent reactive flows of interest here. Details of the AUSM$^+$-up flux function for the filtered equations governing premixed reactive flow are given in the sections to follow.

Piecewise Limited Linear Reconstruction

As indicated above, to extend the discretization to higher-order spatial accuracy, a sub-cell reconstruction is required. A linear least-squares method is used to determine the solution slopes within each cell based on information from neighbouring cells [119]. The fluxes are then calculated by solving a Riemann problem based on the reconstructed solution states at the midpoint of each cell interface as follows:

$$\begin{aligned}\overline{\mathbf{U}}^{\mathrm{L}}_{i+\frac{1}{2},j,k}&=\overline{\mathbf{U}}_{i,j,k}+\Phi_{i,j,k}\vec{\nabla}\overline{\mathbf{U}}_{i,j,k}\cdot\Delta\vec{\mathrm{x}}_{\mathrm{L}},\\ \overline{\mathbf{U}}^{\mathrm{R}}_{i+\frac{1}{2},j,k}&=\overline{\mathbf{U}}_{i+1,j,k}+\Phi_{i+1,j,k}\vec{\nabla}\overline{\mathbf{U}}_{i+1,j,k}\cdot\Delta\vec{\mathrm{x}}_{\mathrm{R}},\end{aligned} \tag{4.15}$$

where $\Delta\tilde{\mathrm{x}}_{\mathrm{L}}$ and $\Delta\tilde{\mathrm{x}}_{\mathrm{R}}$ are given by

$$\begin{aligned} \Delta\vec{\mathrm{x}}_{\mathrm{L}} &= \vec{\mathrm{x}} - \vec{\mathrm{x}}_{i,j,k}, \\ \Delta\vec{\mathrm{x}}_{\mathrm{R}} &= \vec{\mathrm{x}} - \vec{\mathrm{x}}_{i+1,j,k}, \end{aligned} \tag{4.16}$$

and the $\vec{\mathrm{x}}$ is the location of interface center. The vector of slope limiters, Φ, is used for robustness and to maintain monotonicity of the solution near shocks and discontinuities. An extensive analysis of limiters is made in the review by Waterson and Deconinck [120]. Both the Barth-Jespersen and the Venkatakrishnan slope limiters have been implemented in the present algorithm. The Barth-Jespersen limiter [121] which is used extensively in the thesis can be expressed as

$$\Phi_{i,j,k} = \begin{cases} \min\left(1, \frac{\overline{\mathbf{U}}_{\max} - \overline{\mathbf{U}}_{i,j,k}}{\overline{\mathbf{U}}_k - \overline{\mathbf{U}}_{i,j,k}}\right), & \text{if} \quad \overline{\mathbf{U}}_k - \overline{\mathbf{U}}_{i,j,k} > 0, \\ \min\left(1, \frac{\overline{\mathbf{U}}_{\min} - \overline{\mathbf{U}}_{i,j,k}}{\overline{\mathbf{U}}_k - \overline{\mathbf{U}}_{i,j,k}}\right), & \text{if} \quad \overline{\mathbf{U}}_k - \overline{\mathbf{U}}_{i,j,k} < 0, \\ 1, & \text{if} \quad \overline{\mathbf{U}}_k - \overline{\mathbf{U}}_{i,j,k} = 0, \end{cases} \tag{4.17}$$

where

$$\begin{aligned} \overline{\mathbf{U}}_{\max} &= \max(\overline{\mathbf{U}}_{i,j,k}, \overline{\mathbf{U}}_{\text{neighbours}}), \\ \overline{\mathbf{U}}_{\min} &= \min(\overline{\mathbf{U}}_{i,j,k}, \overline{\mathbf{U}}_{\text{neighbours}}), \end{aligned} \tag{4.18}$$

and $\overline{\mathbf{U}}_{\text{neighbours}}$ are the primitive variables of the neighbouring cells. In the expressions above, $\overline{\mathbf{U}}_k$ is the unlimited reconstructed solution value at the k^{th} flux quadrature point.

Approximate Riemann Solvers

As discussed above, Godunov-type finite-volume methods require the solution of locally one-dimensional Riemann problems. The Riemann problem is a special initial-value problem with discontinuous initial states and self-similar solutions. It is posed at the interface between adjacent cells. One approach is to make use of an exact solution procedure for the Riemann problem as outlined by Gottlieb and Groth [115] for the Euler equations governing an ideal polytropic gas. However, often an approximation is sufficient for use in a finite-volume scheme, since only an interface

flux is needed, and the details of the sub-cell solution are averaged out after each time step. The approximate solvers can also be more readily extended for the treatment of more complex systems of partial differential equations, such as the filtered LES equations governing premixed combustion flows of interest here. The most detailed upwind approximation scheme associated with the Riemann problem is found in the solvers of Roe [116], which is based on a local linearization of the flow equations, and Osher [122], which replaces shock waves by inverted isotropic waves [123]. Since then, a family of solvers has been developed by Harten, Lax, and van Leer (HLL) [124], HLLE [117], and AUSM$^+$-up of Liou *et al.*. In this research, Roe, HLLE and AUSM$^+$-up are all implemented in the algorithm. For details related to the Roe and HLLE solvers refer to Sachdev [125] and Gao [126]. Here, our discussion will focus on the Roe and AUSM$^+$-up flux functions for the filtered LES equations of interest.

Roe's approximate Riemann solver is based on a local linearization of the governing partial differential equations (PDEs). The linearized Riemann problem approximates all waves by discontinuous jumps. The one-dimensional, compressible inviscid-form of the filtered equations in non-conservative form is given by

$$\frac{\partial \mathbf{U}}{\partial t} + \frac{\partial \mathbf{F}}{\partial x} = \frac{\partial \mathbf{U}}{\partial t} + \frac{\partial \mathbf{F}}{\partial \mathbf{U}}\frac{\partial \mathbf{U}}{\partial x} \approx \frac{\partial \mathbf{U}}{\partial t} + \hat{\mathbf{A}}(\hat{\mathbf{U}})\frac{\partial \mathbf{U}}{\partial x} = 0, \tag{4.19}$$

where $\hat{\mathbf{A}}(\hat{\mathbf{U}})$ is the flux Jacobian computed at a reference state, $\hat{\mathbf{U}}$, which is a function of the left and right solution states of the Riemann problem, $\mathbf{U}_\mathrm{L}$ and $\mathbf{U}_\mathrm{R}$. Since the approximate flux Jacobian contains constant coefficients, this represents a linear hyperbolic system of equations for which an analytic solution is available for the intercell flux. The flux can be expressed as

$$\mathbf{F}_{i+\frac{1}{2}} = \frac{1}{2}(\mathbf{F}_\mathrm{L} + \mathbf{F}_\mathrm{R}) - \frac{1}{2}\sum_{i}^{m} \hat{\alpha}_i |\hat{\lambda}_i| \hat{\mathbf{R}}_i, \tag{4.20}$$

where m is the number of conservation laws in the system of equations under consideration. An appropriate reference state, $\hat{\mathbf{U}}$, can be constructed for the evaluation of the eigenvalues, $\hat{\lambda}_i$, right eigenvectors, $\hat{\mathbf{R}}_i$, and wave-strengths, $\hat{\alpha}_i$, of the approximate flux Jacobian, $\hat{\mathbf{A}}(\hat{\mathbf{U}})$ in terms of the left and right solution values. This reference state was designed such that the approximate flux Jacobian, $\hat{\mathbf{A}}$, satisfies three conditions:

(i) $\hat{\mathbf{A}}$ has real eigenvalues with a complete set of linearly independent eigenvectors so that the system remains strictly hyperbolic; (ii) it should be consistent with the exact flux Jacobian, if $\mathbf{U}_\mathrm{R}=\mathbf{U}_\mathrm{L}=\mathbf{U}$, then one should have $\hat{\mathbf{A}}=\frac{\partial \mathbf{F}}{\partial \mathbf{U}}|_{\mathbf{U}}$; and (iii) it should ensure conservation across discontinuities, $\mathbf{F}(\mathbf{U}_\mathrm{R})-\mathbf{F}(\mathbf{U}_\mathrm{L})=\hat{\mathbf{A}}(\mathbf{U}_\mathrm{R}-\mathbf{U}_\mathrm{L})$ [116].

For the governing equations described previously, Eq. 1.3 and Eq. 1.4, the Roe-averaged velocity, $\hat{u}$, $\hat{v}$, and $\hat{w}$, sensible enthalpy, $\hat{h}$, progress variable, $\hat{c}$, flame surface density, $\hat{\Sigma}$, and turbulence kinetic energy, k, are all given by the general formula of

$$\hat{\Psi}=\frac{\sqrt{\rho_\mathrm{L}}\Psi_\mathrm{L}+\sqrt{\rho_\mathrm{R}}\Psi_\mathrm{R}}{\sqrt{\rho_\mathrm{L}}+\sqrt{\rho_\mathrm{R}}}, \tag{4.21}$$

where Ψ_L and Ψ_R represent the left and the right state vectors consisting of quantities listed above, and the Roe-averaged density, $\hat{\rho}$, is evaluated by $\hat{\rho}=\sqrt{\rho_\mathrm{L}\rho_\mathrm{R}}$. There are eight eigenvalues for the turbulent combusting flows considered here given by

$$\hat{\lambda}_1=\hat{u}-\hat{a},\quad \hat{\lambda}_{2,3,4}=\hat{u},\quad \hat{\lambda}_5=\hat{u}+\hat{a},\quad \hat{\lambda}_{6,7,8}=\hat{u}. \tag{4.22}$$

The corresponding eigenvector matrices are given in Appendix A.

Roe's approximate Riemann solver is valid for shock and contact waves. An entropy fix is necessary to account for the fact that the Roe's approximate Riemann solver cannot reasonably represent expansion waves associated with acoustic waves having wave speeds $\hat{\lambda}_1$ and $\hat{\lambda}_5$ in the vacinity of sonic points. The averaged eigenvalues, $|\hat{\lambda}_k|$, in Roe's flux function, Eq. 4.20, are replaced by Harten's entropy fix [127] to increase the magnitude of these two acoustic waves near sonic points such that $|\hat{\lambda}_k^*|$ is given by

$$|\hat{\lambda}_k^*|=\begin{cases}|\hat{\lambda}_k| & \text{if } |\hat{\lambda}_k|\geq 2\Delta\lambda_k,\\ \frac{\hat{\lambda}_k^2}{4\Delta\lambda_k}+\Delta\lambda_k & \text{if } |\hat{\lambda}_k|<2\Delta\lambda_k,\end{cases} \tag{4.23}$$

where $\Delta\lambda_k=\max(0,\lambda_k(\mathbf{U}_\mathrm{R})-\lambda_k(\mathbf{U}_\mathrm{L}))$, $k=1,5$. This procedure avoids the prediction of unphysical expansion shocks.

The AUSM$^+$-up scheme is the latest version in the AUSM-family which is valid at all speed regimes and in a Mach-number-independent fashion. The difference between AUSM-family of schemes is that the inviscid flux is split into convective and pressure contributions to the fluxes. The inviscid fluxes of the governing equation in this

research are as follows:

$$\mathbf{F} = \mathbf{F}_{\mathrm{c}} + \mathbf{P} = \dot{m}\mathbf{\Phi} + \mathbf{P} = \bar{\rho}\tilde{u} \begin{pmatrix} 1 \\ \tilde{u} \\ \tilde{v} \\ \tilde{w} \\ \tilde{E} \\ \tilde{c} \\ \tilde{\Sigma} \\ \tilde{k} \end{pmatrix} + \begin{pmatrix} 0 \\ \bar{p} \\ 0 \\ 0 \\ 0 \\ 0 \\ 0 \\ 0 \end{pmatrix}. \tag{4.24}$$

In what follows, the cell interface labeled by subscript "1/2" straddles two neighboring cells labeled by subscripts "L" and "R", respectively, lying to the left and right of the interface.

The numerical flux, $\mathbf{F}_{1/2}$, at cell interface can be expressed in terms of mass flux $\dot{m}=\bar{\rho}\tilde{u}$ and vector $\mathbf{\Phi}=(1,\tilde{u},\tilde{v},\tilde{w},\tilde{E},\tilde{c},\tilde{\Sigma},\tilde{k})^{\mathrm{T}}$ as

$$\mathbf{F}_{1/2} = \dot{m}_{1/2}\mathbf{\Phi}_{\mathrm{L/R}} + \mathbf{P}_{1/2}, \tag{4.25}$$

where $\mathbf{\Phi}_{\mathrm{L/R}}$ is the left and right vectors and will be determined in a simple upwind scheme,

$$\mathbf{\Phi} = \begin{cases} \mathbf{\Phi}_{\mathrm{L}}, & \text{if } \dot{m}_{1/2} > 0, \\ \mathbf{\Phi}_{\mathrm{R}}, & \text{otherwise.} \end{cases} \tag{4.26}$$

The mass flux, $\dot{m}$, is defined as

$$\dot{m}_{1/2} = u_{1/2}\rho_{\mathrm{L/R}} = a_{1/2}M_{1/2} \begin{cases} \rho_{\mathrm{L}}, & \text{if } u_{1/2} > 0, \\ \rho_{\mathrm{R}}, & \text{otherwise,} \end{cases} \tag{4.27}$$

where $u_{1/2}$ is the interface convective velocity, $a_{1/2}$ is the interface speed of the sound, $M_{1/2}$ is the interface Mach number, and $\rho_{\mathrm{L/R}}$ is the left and right density convected by $u_{1/2}$.

The interface Mach number, $M_{1/2}$, is determined in terms of the flow Mach number in the left neighbour and right neighbour cells, M_{L} and M_{R}, respectively, and evaluated using

$$M_{1/2} = \mathcal{M}^{+}_{(m)}(M_{\mathrm{L}}) + \mathcal{M}^{-}_{(m)}(M_{\mathrm{R}}) + M_p. \tag{4.28}$$

The split Mach numbers $\mathcal{M}^{\pm}_{(m)}$ are polynomial functions of degree $m=1,2,4$, as given in [128] and have the form:

$$\mathcal{M}^{\pm}_{(4)}(M) = \begin{cases} \mathcal{M}^{\pm}_{(1)}, & \text{if } |M| \geq 1, \\ \mathcal{M}^{\pm}_{(2)}(1 \mp 16\beta\mathcal{M}^{\mp}_{(2)}), & \text{otherwise}, \end{cases} \tag{4.29}$$

where

$$\mathcal{M}^{\pm}_{(1)}(M) = \frac{1}{2}(M \pm |M|), \tag{4.30}$$

$$\mathcal{M}^{\pm}_{(2)}(M) = \pm\frac{1}{4}(M \pm 1)^2. \tag{4.31}$$

The left and right Mach numbers, $M_{\mathrm{L/R}}$, can be defined by convective velocity, $u_{1/2}$, and the speed of sound, $a_{1/2}$, as follows:

$$M_{\mathrm{L/R}} = \frac{u_{\mathrm{L/R}}}{a_{\mathrm{L/R}}}. \tag{4.32}$$

The pressure diffusion term M_p, introduced to enhance calculations for low flow speeds or multi-phase flow, is defined to be

$$M_p = -\frac{K_p}{f_a}\max(1 - \sigma_p\bar{M}^2, 0)\frac{p_{\mathrm{R}} - p_{\mathrm{L}}}{\rho_{1/2}a^2_{1/2}}, \tag{4.33}$$

where

$$\rho_{1/2} = \frac{\rho_{\mathrm{L}} + \rho_{\mathrm{R}}}{2}, \tag{4.34}$$

$$a_{1/2} = \frac{a_{\mathrm{L}} + a_{\mathrm{R}}}{2}, \tag{4.35}$$

and

$$\bar{M}^2 = \frac{u^2_{\mathrm{L}} + u^2_{\mathrm{R}}}{2a_{1/2}} \tag{4.36}$$

with $0 \leq K_p \leq 1$ and $\sigma_p \leq 1$. The scaling factor is defined by the reference Mach number M_0 as follows:

$$f_a(M_0) = M_0(2 - M_0) \in [0, 1], \tag{4.37}$$

where the reference Mach number is given by

$$M_0^2 = \min(1, \max(\bar{M}^2, M^2_\infty)) \in [0, 1]. \tag{4.38}$$

The formula for evaluating the pressure flux is similar to that for the mass flux and takes the form

$$p_{1/2} = \mathcal{P}^{+}_{(n)}(M_{\mathrm{L}})p_{\mathrm{L}} + \mathcal{P}^{-}_{(n)}(M_{\mathrm{R}})p_{\mathrm{R}} + p_u, \tag{4.39}$$

where $n = 1, 3, 5$ correspond to the degree of the polynomials $\mathcal{P}^{\pm}$, as in $\mathcal{M}^{\pm}$. In general, the fifth-degree polynomials proposed by Liou [128] are preferred because they are found to yield more accurate solutions. They are also expressed in terms of the split Mach number and can be written as

$$\mathcal{P}^{\pm}_{(5)}(M) = \begin{cases} \frac{1}{M}\mathcal{M}^{\pm}_{(1)}, & \text{if } |M| \geq 1, \\ \mathcal{M}^{\pm}_{(2)}[(\pm 2 - M) \mp 16\alpha M \mathcal{M}^{\mp}_{(2)}], & \text{otherwise}, \end{cases} \tag{4.40}$$

and the velocity difference (diffusion) term p_u is evaluated by

$$p_u = -K_u \mathcal{P}^{+}_{(5)}(M_{\mathrm{L}})\mathcal{P}^{-}_{(5)}(M_{\mathrm{R}})(\rho_{\mathrm{L}} + \rho_{\mathrm{R}})(f_a a_{1/2})(u_{\mathrm{L}} + u_{\mathrm{R}}), \tag{4.41}$$

using the parameters

$$\alpha = \frac{3}{16}(-4 + 5f_a^2) \in \Big[-\frac{3}{4}, \frac{3}{16}\Big], \tag{4.42}$$

$$\beta = \frac{1}{8} \tag{4.43}$$

with $0 \leq K_u \leq 1$. In this thesis work, $K_p = 0.25$, $K_u = 0.75$, and $\sigma_p = 1.0$ are used [118].

The AUSM^{+}-up scheme has been shown to be valid in low speed flows and robust for all Mach number regimes. A more complete and detailed discussion is given in the recent paper by Liou [118].

4.2.3 Viscous Flux Evaluation

The viscous fluxes of the governing equations are elliptic in nature and should therefore not be upwinded. Furthermore, evaluation of the viscous component of the numerical flux depends on both the solution and its gradients at the cell interfaces as follows:

$$\vec{\mathbf{F}}_{i+\frac{1}{2},j,k} = \vec{\mathbf{F}}\left(\mathbf{U}_{i+\frac{1}{2},j,k}, \vec{\nabla}\mathbf{U}_{i+\frac{1}{2},j,k}\right), \tag{4.44}$$

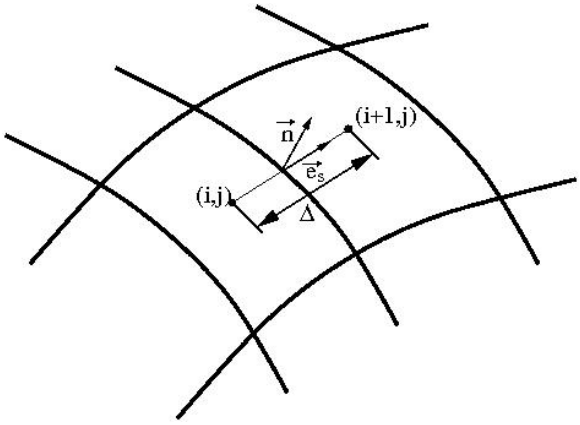

Figure 4.1: Hybrid average gradient-diamond-path approach for a two-dimensional grid.

where $\mathbf{U}_{\mathrm{i+\frac{1}{2},j,k}}$ is the solution vector at the cell interface which is evaluated by averaging the reconstructed values of the left and right of the all interface and given by

$$\mathbf{U}_{\mathrm{i+\frac{1}{2},j,k}} = \frac{(\mathbf{U}_{\mathrm{L}} + \mathbf{U}_{\mathrm{R}})}{2}. \tag{4.45}$$

In this thesis work, the gradient, $\vec{\nabla}\mathbf{U}_{i+\frac{1}{2},j,k}$ is evaluated by employing a hybrid average gradient-diamond-path approach proposed by Mathur and Murthy [3, 129]. In this approach, the cell-face gradient is determined using

$$\vec{\nabla}\mathbf{U}_{i+\frac{1}{2},j,k} = \frac{\mathbf{U}_{i+1,j,k} - \mathbf{U}_{i,j,k}}{\Delta}\frac{\vec{n}}{\vec{n}\cdot\vec{e_s}} + \left(\overline{\nabla\mathbf{U}} - \overline{\nabla\mathbf{U}}\cdot\vec{e}_s\frac{\vec{n}}{\vec{n}\cdot\vec{e_s}}\right), \tag{4.46}$$

with

$$\overline{\nabla\mathbf{U}} = \alpha\nabla\mathbf{U}_{i,j,k} + (1-\alpha)\nabla\mathbf{U}_{i+1,j,k}, \tag{4.47}$$

and $\vec{n}$ the norm of the face, Δ the distance between the adjacent cell centres, and $\mathbf{e}_s$ the unity vector along this direction. The weighting factor, α, is based on cell volume ratios and given by

$$\alpha = \frac{V_{i,j,k}}{V_{i,j,k} + V_{i+1,j,k}}. \tag{4.48}$$

These parameters and procedure for the viscous flux evaluation are depicted in the schematic diagram of Figure 4.1 for a two-dimensional computational grid. The procedure is also directly applicable in the three-dimensional case.

4.2.4 Time Marching Scheme

The set of coupled non-linear ordinary differential equations (ODEs) arising from the spatial discretization procedure given by Eq. 4.13 can be solved by applying a time-marching scheme to advance the solution forward in time. In this work, the linear reconstruction used in the spatial discretization scheme is second-order accurate. To maintain a consistent scheme in terms of accuracy, a time-marching scheme having the same order of accuracy is used. Various time-marching methods can be used for different purposes. For more information on time marching schemes, refer to CFD textbooks by Lomax, Pulliam and Zingg [32] and by Hirsch [130, 131]. In this thesis research, the explicit two-stage Runge-Kutta time-marching scheme is used [32].

The explicit time marching used here is conditionally stable and the time step is limited by the inviscid Courant-Friedrichs-Lewy (CFL) stability, viscous von Neumann stability, and the turbulent and chemical time-step constraints. For reacting flows, the inverse of the maximum diagonal of the chemical source term Jacobian is added to the time step calculation. A stable time step, Δt^n, is then determined by using

$$\Delta t^n = \min\Big(\mathrm{CFL}\frac{\Delta l}{|\vec{u}|+a}, \frac{\alpha}{2}\frac{\rho\Delta l^2}{\max(\nu,\nu_\mathrm{t})}, \big(\beta\max\frac{\partial \mathbf{S}}{\partial \mathbf{U}}\big)^{-1}\Big), \tag{4.49}$$

where Δl is the cell-face length of a cell, a is the sound speed, and ν and ν_t are molecular viscosity and turbulent eddy viscosity, respectively, and where α and β are scaling factors.

4.3 Block-Based Adaptive Mesh Refinement

Adaptive mesh refinement algorithms automatically adapt the mesh to the solution of the governing equations and can be very effective in treating problems with disparate length scales. AMR permits local mesh refinement and helps to minimize the number of computational cells required for a particular calculation. There has been extensive research in the past 15-20 years on AMR algorithms including studies of patch-based AMR [132, 133], cell-based AMR [134, 135], blocked-based

AMR [132, 133, 136–140] and hybrid block-based AMR methods [141]. In this research, a block-based AMR formulation is used that borrows from the ideas of Berger and co-workers [132, 133, 136–140] for Cartesian meshes and has similarities with the block-based approaches described by Quirk [139] and Berger [136]. As in other extensions of Cartesian mesh adaptation procedures to more arbitrary quadrilateral and hexagonal meshes [142, 143], the proposed AMR scheme allows for the use of multi-block, body-fitted anisotropic grids for resolving thin shear and boundary layers. Moreover, a refinement procedure preserves the original stretching of the mesh. Based on the approach developed by Groth *et al.* [144, 145] for computational magnetohydrodynamics, a flexible block-based hierarchical data structure is used to facilitate the automatic solution-directed mesh adaptation of the mesh according to physics-based refinement criteria.

The implementation of the AMR procedure in the proposed algorithm involves the following steps [3]:

- evaluation of the refinement measures for each solution block and marking of solution blocks for refinement and coarsening;
- assessment of the refinement levels for all solution blocks to ensure that the refinement ratio between adjacent blocks is no greater than 1:2;
- removal of solution blocks associated with coarsening of grid;
- addition of "leaves" representing new children solution blocks in the tree data structure;
- update of block connectivity and block information used in sharing solution data between blocks; and
- application of the actual coarsening and refinement of blocks marked for a resolution change with a redistribution of the children solution blocks among the processors to ensure load balancing.

In this research, the two-dimensional AMR scheme has been applied when evaluating the mesh resolution requirements of the FSD subfilter-scale model. A brief review

of the block-based AMR methodology is given below and a more detailed account can be found in the Ph.D thesis by Gao [126]. Although this study only considered the application of AMR to two-dimensional flames and the FSD resolution requirements for this case, the three-dimensional AMR scheme has been fully implemented by Gao [3] and Northrup and Groth [146].

In the AMR scheme used here, each of these structured blocks of the computational mesh consists of $M_x \times M_y$ quadrilateral cells in two space dimensions and $M_x \times M_y \times M_z$ hexahedral cells in the three-dimensional case, where M_x, M_y and M_z are even but not necessarily equal integers. Mesh adaptation is accomplished by dividing and coarsening of appropriate grid blocks. In regions requiring increased cell resolution, a "parent" block is refined by dividing itself into four or eight "children" or "offspring" depending on the dimensionality. Each of the four or eight children of a parent block becomes a new block having the same number of cells as the parent and thereby doubling the cell resolution in the region of interest. This refinement process can be reversed in regions that are deemed over-resolved and four or eight children are coarsened or merged into a single parent block. Figure 4.2 illustrates two neighbouring hexahedral blocks of a three-dimensional mesh, the top block has undergone one level of refinement and the bottom block has not. The resulting refined grid consists of nine blocks. The refined grid can be coarsened or de-refined by reversing the division process and merging eight blocks into one.

The refining and coarsening of blocks are directed using multiple physics-based refinement criteria as previously discribed by Powell *et al.* [134]. For the turbulent combusting flows considered here, the following refinement criteria are used:

$$\epsilon_1 \propto |\vec{\nabla}\rho|, \quad \epsilon_2 \propto |\vec{\nabla} \cdot \vec{u}|, \quad \epsilon_3 \propto |\vec{\nabla} \times \vec{u}|,$$
$$\epsilon_4 \propto |\vec{\nabla}T|, \quad \epsilon_5 \propto |c|, \quad \epsilon_6 \propto |\Sigma|. \tag{4.50}$$

The first three quantities correspond to local measures of the density gradient, compressibility, and vorticity of the mean flow field and enable the detection of contact surfaces, shocks, and shear layers. The last three measure the gradient of mean temperature, progress variable, and flame surface density and provide reliable detection of flame fronts and combustion zones for reactive flows. In this thesis, the last crite-

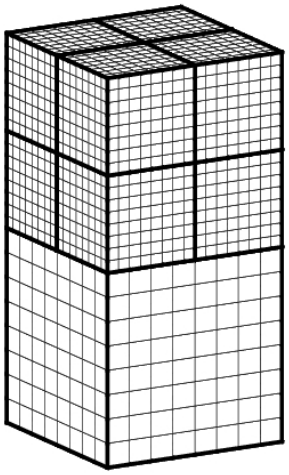

Figure 4.2: An example of two neighbouring$8 \times 8 \times 8$ hexahedral solution blocks: one which has undergone refinement and one which has not [3].

rion, flame surface density, has been used in the two-dimensional freely propagating turbulent premixed flame with AMR.

Using these measures, the decision for refinement of a given solution block is determined according to the following procedure [3]:

- calculate the refinement measures for each cell and assign the maximum value for all cells as the refinement measures for the solution block;
- determine the global minimal and maximal values of the refinement criteria for all solution blocks.
- mark solution blocks to be refined/coarsened after comparing their refinement measures to the refinement/coarsening thresholds scaled by the global extrema, i.e., blocks with refinement measures below some specified minimum measure are coarsened and blocks with measures above some upper bound are refined.

In order to maintain the connectivity of the solution blocks in the multi-block mesh, a flexible block-based hierarchical tree-like data structure is used herein. In

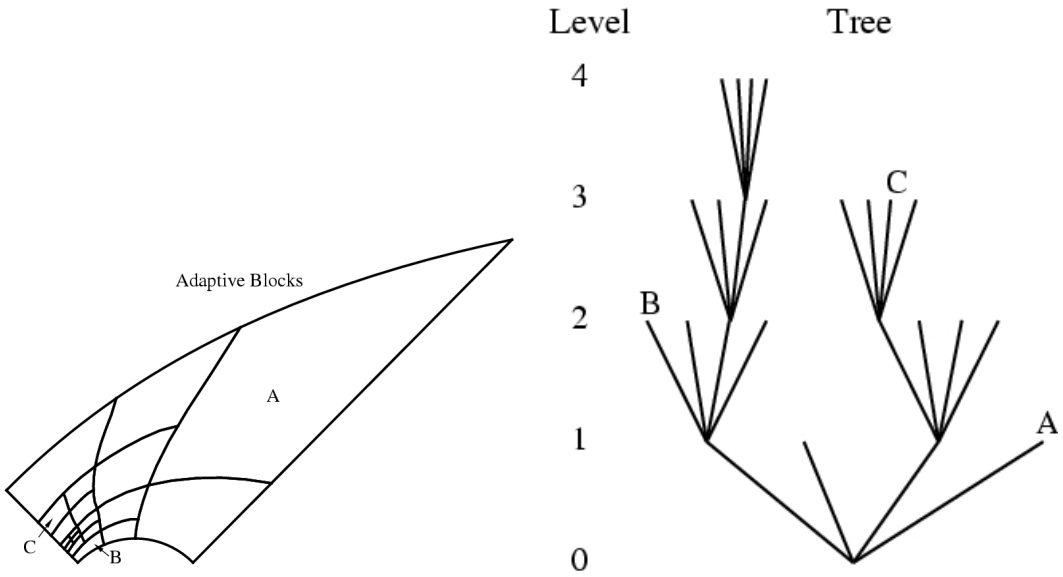

(a) Multi-block refinement (b) Quadtree

Figure 4.3: Multi-block quadrilateral AMR mesh showing solution blocks at various levels of refinement and the corresponding quadtree data structure [3].

particular, quadtree and octree data structures are used for tracking the connectivity of blocks in the two- and the three-dimensional cases, respectively. Figure 4.3(a) shows two-dimensional multi-block quadrilateral AMR mesh solution blocks at various levels of refinement. Figure 4.3(b) illustrates the corresponding quadtree data structure used to keep track of mesh refinement and the connectivity between solution blocks. Figure 4.4 depicts a three-dimensional multi-block hexahedral AMR mesh consisting of solution blocks at various levels of refinement and the corresponding octree data structure. The quadtree/octree data structure developed here naturally keeps track of the refinement level and connectivity between grid blocks during isotropic refinement processes. Although it is not strictly anisotropic, the refinement approach here preserves original stretching of the mesh and allows for anisotropic mesh and improved treatment of thin boundary and shear layers.

To allow data to be exchanged between adjacent blocks, having common interfaces, each block has an additional two (or more) layers of overlapping "ghost" cells, which contain solution information from neighbouring blocks. This happens by exchanging

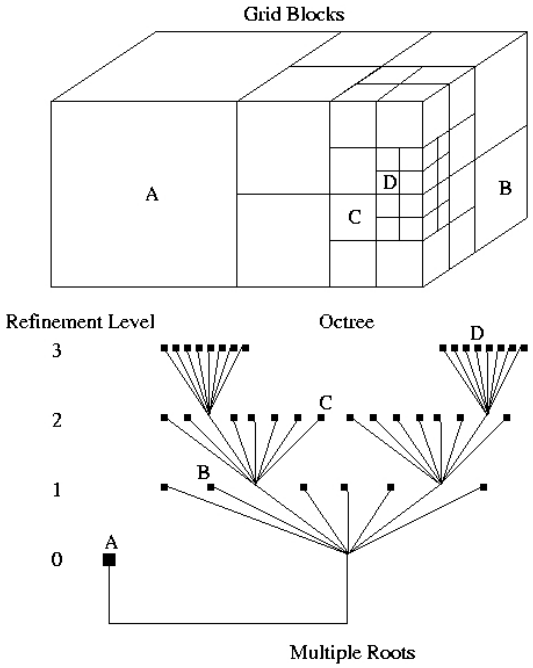

Figure 4.4: Multi-block hexahedral AMR mesh showing solution blocks at various levels of refinement and the corresponding octree data structure [3].

information of the "ghost" cells between adjacent blocks after each time step. In this research, two additional layers of overlapping "ghost" cells have been used to share the solution information between adjacent blocks. Figures 4.5(a) and 4.5(b) show the ghost cells used for two- and three-dimensional solution blocks, respectively. The ghost cells provide solution information from neighbouring blocks and are used to facilitate communications between solution blocks.

4.4 Domain Decomposition and Parallel Implementation

The multi-block hexahedral mesh and tree data structure lends itself naturally to domain decomposition and enables efficient and scalable implementations of the solution algorithm for the reactive mixture conservation equations on distributed-

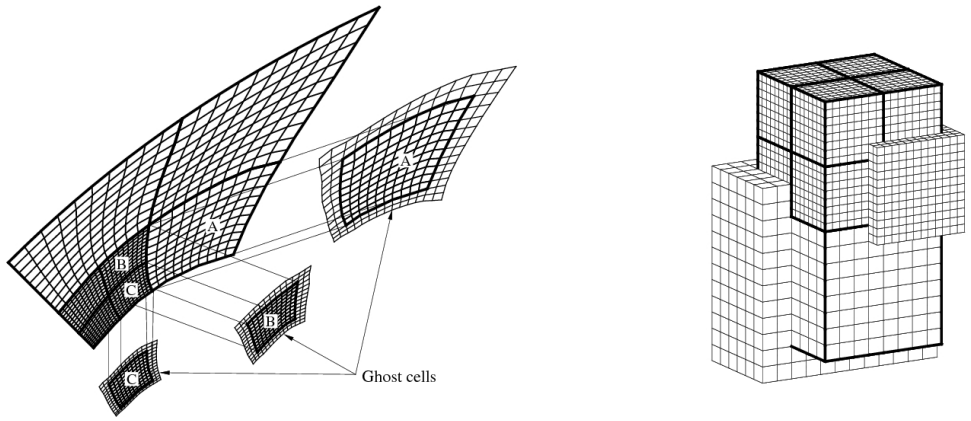

(a) Two space dimensions

(b) Three space dimensions

Figure 4.5: Two layers of overlapping "ghost" cells contain solution information from neighbouring blocks [3].

memory multi-processor architectures [147]. A parallel implementation of the block-based AMR scheme has been developed using the C++ programming language and the message passing interface (MPI) library [3,148]. Domain decomposition is carried out by farming the solution blocks out to the separate processors, with more than one block permitted on each processor. For homogeneous architectures with multiple processors all of equal speed, an effective load balancing is achieved by exploiting the self-similar nature of the solution blocks and simply distributing the blocks equally among the processors. For heterogeneous parallel machines, such as a network of workstations and computational grids, a weighted distribution of the blocks can be adopted to preferentially place more blocks on the faster processors and less blocks on the slower processors. Inter-processor communication is mainly associated with block interfaces and involves the exchange of ghost-cell solution values and conservative flux corrections at every stage of the multi-stage time integration procedure. Message passing of the ghost-cell values and flux corrections is performed in an asynchronous fashion with gathered wait states and message consolidation [149].

Chapter 5

Simulation Results

In this chapter, numerical simulation results for the flame surface density model applied to the prediction of premixed flames in one, two, and three-dimensions are described and discussed. Both freely propagating flames in isotropic decaying turbulence and the turbulent methane/air flames associated with a cylindrical Bunsen-type burner for both stoichiometric and lean fuel/air mixtures are considered. The predictions of the FSD model are compared to those obtained with the thickened-flame subfilter model for the two-dimensional flames and comparisons are also made between the FSD predictions and experimental results for the Bunsen burner flame in full three space dimensions. The numerical results provide a partial validation of the LES methodology and demonstrate the predictive capabilities of the FSD model for flames representative of more practical combustion processes, such as the combustion occurring in lean-premixed gas turbine engines.

Computational resources for performing all of the calculations reported herein were provided by the SciNet High Performance Computing Consortium at the University of Toronto and Compute/Calcul Canada through funding from the Canada Foundation for Innovation (CFI) and the Province of Ontario, Canada. All of the computations were carried out on a cluster of IBM Power6-575 (4.7 GHz) nodes connected with a high-speed, low-latency, non-blocking 4x-DDR Infiniband interconnect.

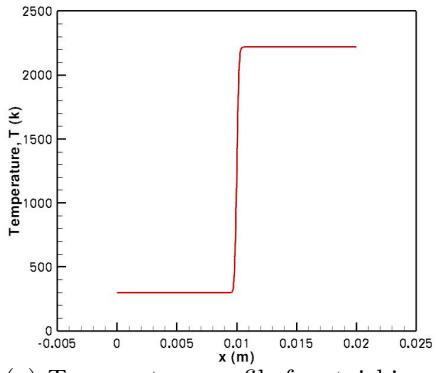

(a) Temperature profile for stoichiometric laminar premixed 1D CH_4-Air flame.

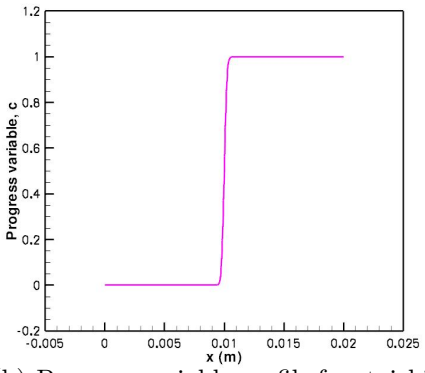

(b) Progress variable profile for stoichiometric laminar premixed 1D CH_4-Air flame.

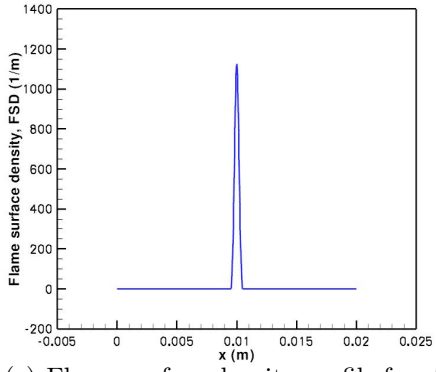

(c) Flame surface density profile for stoichiometric laminar premixed 1D CH_4-Air flame.

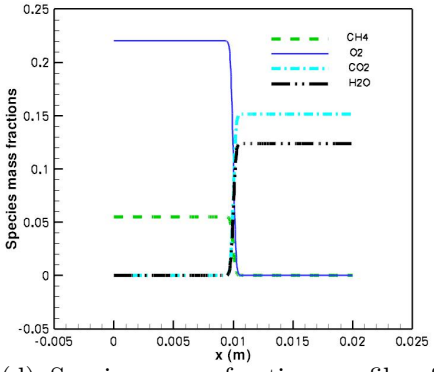

(d) Species mass fraction profiles for stoichiometric laminar premixed 1D CH_4-Air flame.

Figure 5.1: Flame profiles for stoichiometric laminar premixed 1D CH_4-Air flame.

5.1 One-Dimensional Premixed Flames

5.1.1 One-Dimensional Laminar Premixed Flame

The validation of the current implementation of the FSD model is first examined for a one-dimensional laminar premixed flame under stoichiometric conditions ($\phi = 1.0$). This problem provides a good first test of the validity of the implementation of the FSD model in the current LES framework with the parallel AMR finite-volume solution procedure.

Numerical results for this case are summarized in Figures 5.1(a)–5.1(d) and present partial verification of the implementation of FSD model. The figures provide predictions of the flame structure and show the variation of the velocity, progress variable, flame surface density, and species mass fraction through the flame. The computational domain consists of 100 cells in the direction of flame propagation and mesh stretching is used to cluster cells near the center of the domain where the flame front is located. The inlet and outlet boundary velocity and pressure, denoted by subscripts 1 and 2, respectively, have been adjusted systematically such that the mass flux is constant throughout the domain and a stationary flame structure is achieved. The inlet premixed fuel and oxidizer initial conditions are held constant except for the velocity, u_1, which is computed using the outlet velocity, u_2, and density, ρ_2, assuming a constant mass flux, $\rho_1 u_1 = \rho_2 u_2$. The outlet properties are all extrapolated from the interior of the domain except for pressure, which is calculated from the inlet pressure using relation $p_2 = p_1 - \rho u_1(u_1 - u_2)$. The Roe flux function with VVenkatakrishnan limiter were both used along with a 4-stage optimally smoothing time marching scheme to obtain the steady state for the flame structure. Low-Mach number preconditioning with a minimum preconditioning Mach number $M_{\mathrm{r}_{\min}}$ of 0.1 along with scalar local time-stepping were used to accelerate convergence of the calculations to steady state.

The predicted temperature of the products for this one-dimensional planar flame, $T = 2218.5$ K, is in good agreement with the predicted value obtained using Cantera [150] ($T = 2218$ K) and the results of Figure 5.1 provide good support for the validity of the present implementation of the FSD model and LES solver.

5.1.2 One-Dimensional Turbulent Premixed Flames

In order to validate further the implementation of FSD model and assess the dependence of the net propagation speed, s_{T}, on the turbulent kinetic energy, k, the simulation of the one-dimensional turbulent propagation flame was again performed here with prescribed values for the turbulent kinetic energy throughout the domain. The laminar flame calculation described above was repeated with a constant value for the turbulent intensity, u', imposed everywhere throughout the domain.

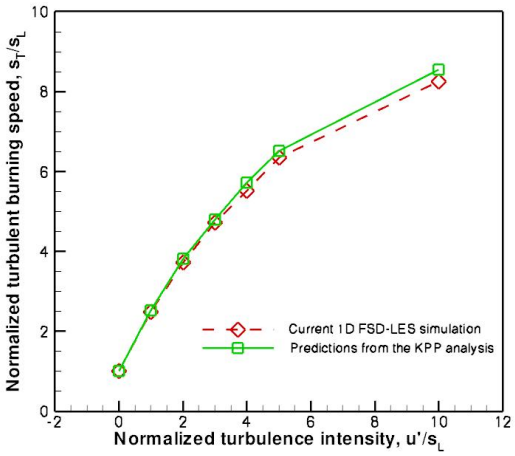

Figure 5.2: Comparison of the current 1D FSD-LES simulation results to the predictions of KPP analysis.

This test case provides further evaluation of the implementation of the subfilter-scale modelling based on the FSD model. The results of the turbulent flame calculations are shown in Figure 5.2. The computed turbulent flame speeds are compared with the expected KPP (Kolmogorov-Petrovski-Piskunov) values for different values of u'/s_{L} ranging from 0 to 20. KPP analysis [112,151,152] is a simple theoretical tool that may be used to analyze turbulent combustion models. The analysis is based on several restrictive assumptions, including the assumption of frozen turbulence (turbulent flow field is not affected by combustion), and may be applied to specific classes of combustion models. A more detailed description of KPP analysis is given in Appendix B. From the seven cases shown in the figure, in which $u'/s_{\mathrm{L}} = 0.0$, 1.0, 2.0, 3.0, 4.0, 5.0, and 10.0, we can see that there is good agreement of the predicted turbulent flame speeds obtained using the FSD model and finite-volume solution procedure with the expected KPP values. These one-dimensional results provide further evidence of the validity of the current implementation of the FSD-LES modelling.

5.2 Two-Dimensional Premixed Turbulent Freely Propagating Flames

As a next step in the verification and validation process for the FSD-LES modelling, numerical predictions have been carried out for a two-dimensional freely propagating turbulent premixed methane-air flame. Although it can be argued that two-dimensional turbulence differs strongly from three-dimensional turbulence by the absence of the vortex stretching mechanism, turbulent curvature statistics suggest that the three-dimensional topology of a propagating surface is primarily two-dimensional [153,154]. Moreover, the two-dimensional premixed flame studies considered here have provided a solid basis for performing subsequent fully three-dimensional simulations and evaluating and interpreting the three-dimensional results.

The stoichiometric premixed flame is initialized by introducing a one-dimensional planar laminar premixed flame similar to that discussed above on to a computational domain with isotropic turbulence. Subsonic boundary conditions are prescribed at inflow and outflow boundaries, and periodic boundary conditions are applied at the top and bottom of the domain. The initial homogeneous turbulent flow field is generated by prescribing a specified synthetic energy spectrum [97] and using the procedure developed by Rogallo [155]. The parameters characterizing the initial conditions for the turbulent flame are: turbulence intensity, $u' = 2.59$ m/s; integral length scale, $\Lambda = 6.47$ mm; Taylor micro scale, $\lambda = 0.832$ mm; Kolmogorov scale $\eta = 0.06$ mm; turbulent Reynolds number, $\mathrm{Re}_\lambda = 137$; laminar flame speed $s_\mathrm{L} = 0.38$ m/s; and flame thickness, $\delta_\mathrm{L} = 0.044$ mm. The size of the rectangular-shaped domain considered for the simulation is $x = 0.0366$ m and $y = 0.0342$ m. This provides a computational domain that contains approximately 44 Taylor micro length scales and 5.6 integral length scales associated with the imposed turbulence field in the direction of flame propagation.

5.2.1 Influences of Mesh Resolution

In order to resolve the turbulence field and flame front properly, the simulation domain should be discretized with a sufficient number of cells to be able to accurately represent the turbulence and flame front. In particular, for the FSD model, it is important that the soliton-like nature of the FSD solution at the flame front is accurately resolved. For this purpose, it was felt that the baseline mesh resolution requirements of the proposed finite-volume scheme for accurately representing the freely-propagating flame of interest should be established. A study of the influence of the mesh resolution on the solution quality was therefore carried out. Four different uniform grids were considered: $64\times60=3,840$, $128\times120=15,360$, $256\times240=61,440$, and $512\times480=245,760$ cell meshes with the computational cells equally distributed on 48 solution blocks. The cell sizes compared to the Taylor micro and Kolmogorov scales for each of the different mesh resolutions are $\Delta x=0.56\lambda=7.36\eta$ for 64×60 cells, $\Delta x=0.33\lambda=4.14\eta$ for 128×120 cells, $\Delta x=0.17\lambda=2.3\eta$ for 256×240 cells, and $\Delta x=0.08\lambda=1.17\eta$ for 512×480 cells. For each simulation, the filter width, Δ, was held fixed and equal to $\Delta=2\Delta x_{128\times120}$, where $\Delta x_{128\times120}=0.267=1.25\delta_{\mathrm{L}}$ mm is the mesh spacing of the 128×120 grid. The simulation results are computed up to 0.3 ms, which corresponds to a time of approximately one eddy turnover based on the Taylor micro scale.

The predicted FSD solutions of the freely-propagating flame in the two-dimensional decaying turbulence flow field on the four different mesh resolutions are shown in Figures 5.3(a)–5.3(d). Color contours of the predicted values of $\bar{\rho}\tilde{\Sigma}$ are given in the figures with peak values of the FSD occurring within the flame. The wrinkling of the initially planar laminar flame by the resolved turbulent field is quite evident in each case. Although very long time results are not shown here, it was found that there is a corresponding increase in the calculated turbulent flame speed as the simulation progresses until a near equilibrium flame speed is achieved of $s_{\mathrm{T}}=0.95$ m/s ($s_{\mathrm{T}}/s_{\mathrm{L}}\approx2.5$) at $t=1.8$ ms. At that point in the calculation, the predicted turbulent intensity has diminished by more than a factor of 30%.

Comparing the results of Figures 5.3(a)–5.3(d), it is fairly evident that the coars-

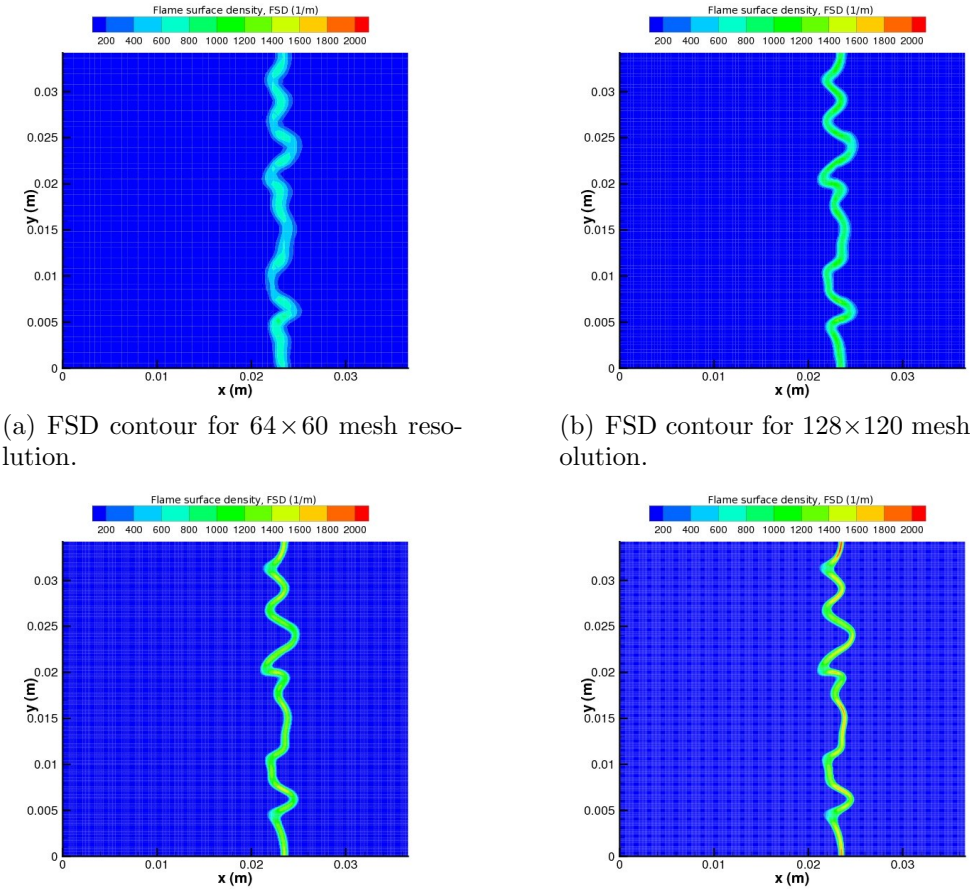

(a) FSD contour for 64×60 mesh resolution.

(b) FSD contour for 128×120 mesh resolution.

(c) FSD contour for 256×240 mesh resolution.

(d) FSD contour for 512×480 mesh resolution.

Figure 5.3: Predicted contours of the flame surface density, $\bar{\rho}\tilde{\Sigma}$, at $t = 0.3$ ms. Results are shown for four different computational grids: (a) uniform mesh with 64×64 cells; (b) uniform mesh with 128×128 cells; (c) uniform mesh with 256×256 cells; and (d) uniform mesh with 512×512 cells.

est mesh (64 × 60 cells) does not provide adequate resolution of the flame front as compared to the solution on the finest mesh. The finest mesh (512×480 cells) results in a well resolved thin and smooth flame front with a well predicted maximum value for the FSD. The peak values of the FSD increases with the increased mesh resolution: $\text{FSD}_{\text{max}} = 1282/\text{m}$ for the 64×60 grid, $\text{FSD}_{\text{max}} = 1677/\text{m}$ for the 128×120 grid, $\text{FSD}_{\text{max}} = 1812/\text{m}$ for the 256×240 grid, and $\text{FSD}_{\text{max}} = 1921/\text{m}$ for the 512×480 grid. Nevertheless, the solutions on the other intermediate meshes (256×240 and 128×120

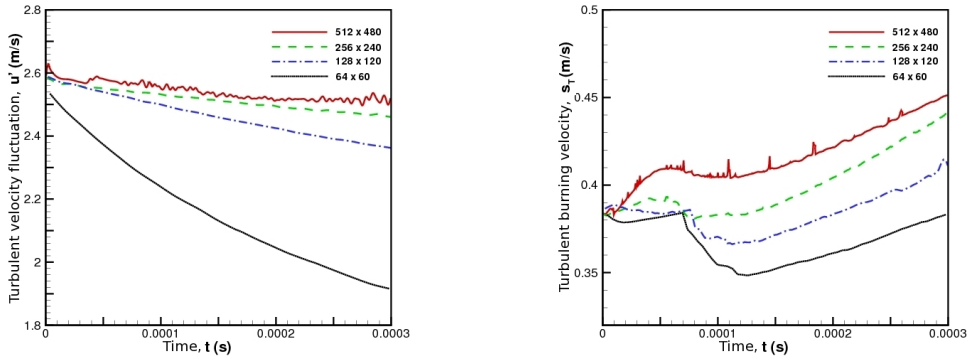

(a) Resolved turbulence intensity decay. (b) Predicted turbulent burning rate.

Figure 5.4: Predicted decay of resolved turbulence intensity (a) and predicted turbulent burning rate (b) for the different mesh resolutions: uniform mesh with 64×60 cells; uniform mesh with 128×120 cells; uniform mesh with 256×240 cells; and uniform mesh with 512×480 cells.

grids) also show reasonable agreement with the finest mesh solution in terms of overall flame wrinkling and peak values of the FSD.

Turning attention to the predicted turbulent field, the predicted temporal variations of the resolved turbulence intensity, u', determined for each of the four meshes are shown in Figure 5.4(a). It may be observed that the predictions of u' for the 512×480, 256×240 and 128×120 grids are generally in agreement. In fact it appears that a virtually grid-independent result has been achieved on the 256×240 mesh, whereas the 64×60 grid result is clearly somewhat under-resolved. However, even though the turbulence field is generally resolved on the finer meshes, if one considers the predicted turbulent flame speed on each mesh as shown in Figure 5.4(b), it is quite apparent that the flame front and FSD are still not yet fully resolved. Further refinement of the mesh is required to obtain a fully grid-independent solution. Note that similar mesh refinement studies have been performed for the thickened flame model and, as expected, the artificial thickening of the flame front reduces the mesh resolution requirements for obtaining grid-independent burning rates (accurate burning rates can be achieved on more moderately refined meshes).

5.2.2 Influences of Filter Width

In LES, aside from mesh resolution, the filter size, Δ, is an important factor affecting the quality of the simulation results. The two-dimensional freely-propagating premixed flame has been considered on the base, 128×120 grid, for four different filter sizes, Δ: $0.5\Delta x$, Δx, $2\Delta x$, and $4\Delta x$, in which Δx is the cell size. The simulation results were again carried out for one eddy turnover time or until $t = 0.3$ ms.

Figure 5.5 gives the comparison contours of FSD between the filter size $0.5\Delta x$ (Figure 5.5(b)) and the filter size $4.0\Delta x$ (Figure 5.5(d)). It may be seen that the wrinkling of the flame surface decreases and the flame thickness increases as the filter size is increased. This is expected since the filtering process would smear out the flame area, reducing flame wrinkling and increasing the flame thickness. The maximum values of FSD decrease for increasing the filter size, and this is physically consistent considering the definition of FSD. The comparison of turbulence decay between the different filter sizes has been shown in Figure 5.5(e). It is evident that the increased filter size is resulting in faster turbulence decay. This also can be understood from the LES philosophy, in which the magnitude of the resolved scales decrease and the magnitude of subfilter-scales increase with the increased filter size as more turbulence energy is shifted to the unresolved scale. In LES of turbulent premixed flames, the relative degree of resolved turbulence compared to the unresolved turbulence is an important aspect. For different filter sizes, the percentages of unresolved turbulence are 0.34% for $\Delta = 0.5\Delta x$, 1.5% for $\Delta = \Delta x$, 5.6% for $\Delta = 2\Delta x$, and 20% for $\Delta = 4\Delta x$ case. In this thesis, the expected percentage of unresolved turbulence should be less than 20% and greater than 1.5%. From the above discussion, it is suggested for the future applications of the current LES solver that the filter width, Δ, should be twice of the mesh size, i.e., $\Delta = 2\Delta x$.

5.2.3 Adaptive Mesh Refinement

As noted in Section 5.2.1, one of the numerical challenges associated with the FSD subfilter-scale model is that the resolution requirements for $\tilde{\Sigma}$ are typically quite high, requiring higher resolution of the flame surface than that required by other competing

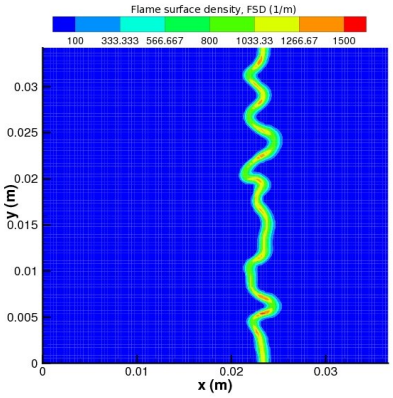

(a) FSD contour with filter size $0.5\Delta x$.

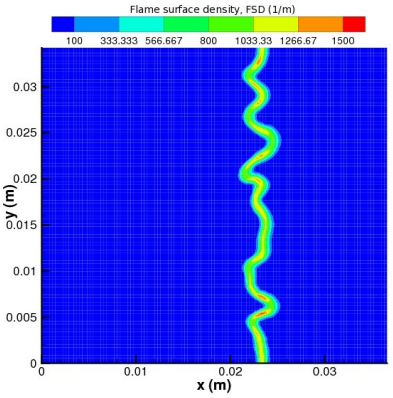

(b) FSD contour with filter size Δx.

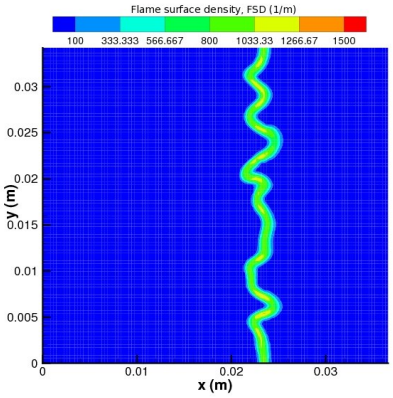

(c) FSD contour with filter size $2.0\Delta x$.

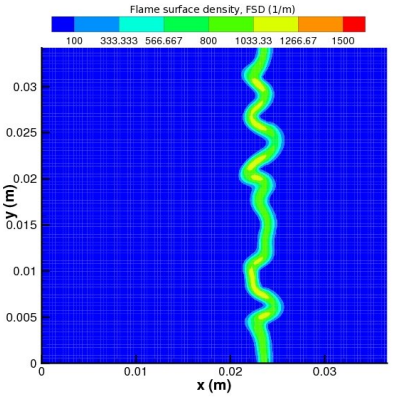

(d) FSD contour with filter size $4\Delta x$.

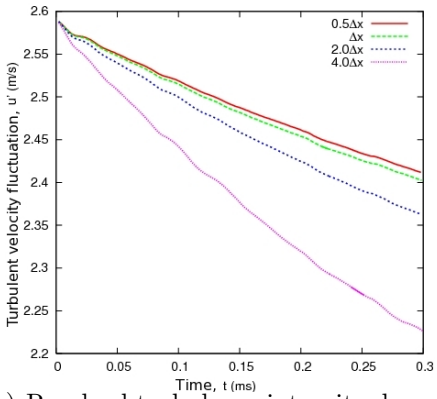

(e) Resolved turbulence intensity decay.

Figure 5.5: Predicted contours of FSD and resolved turbulence intensity decay with different filter sizes.

subfilter-scale treatments for premixed flames. For the case described above, the thickness of the turbulent flame based on the FSD is about 1.5λ or $3\delta_{\mathrm{L}}$, requiring

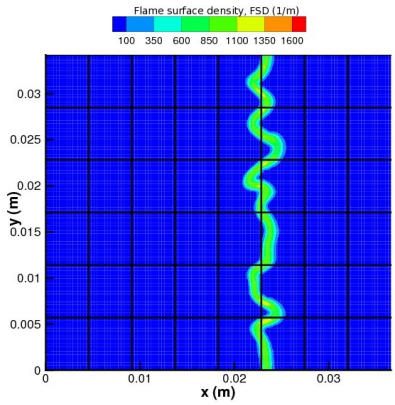

(a) Predicted contours of FSD, $\bar{\rho}\tilde{\Sigma}$, for a 128×120 uniform mesh with 48 blocks.

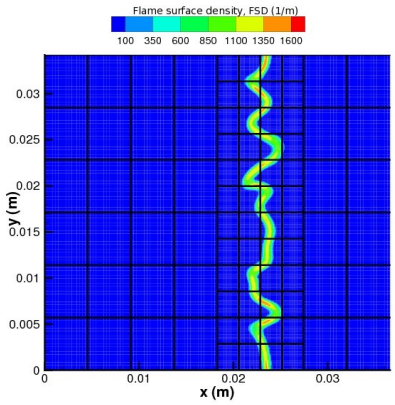

(b) Predicted contours of FSD, $\bar{\rho}\tilde{\Sigma}$, for AMR mesh with 1-level of refinement; 84 blocks and 26,880 cells.

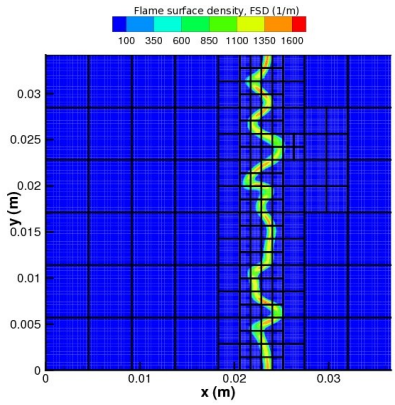

(c) Predicted contours of FSD, $\bar{\rho}\tilde{\Sigma}$, for AMR mesh with 2-level of refinement; 165 blocks and 52,800 cells.

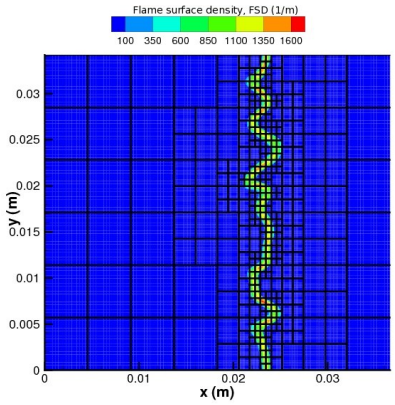

(d) Predicted contours of FSD, $\bar{\rho}\tilde{\Sigma}$, for AMR mesh with 3-level of refinement; 390 blocks and 124,800 cells.

Figure 5.6: Predicted contours of fame surface density, $\bar{\rho}\tilde{\Sigma}$, through the turbulent flame front obtained using uniform mesh with 128×120 cells and AMR meshes with 1-, 2- and 3-levels of refinement.

mesh spacing considerably smaller than the filter width, Δ, to accurately resolve the variation of $\tilde{\Sigma}$ across the flame. The proposed finite-volume AMR treatment was found to be very effective in accurately treating the flame front. The technique permitted local refinement of the mesh to resolve the FSD solution and thereby obtain near grid-independent results in a very economical fashion. Figures 5.6(a)–5.6(d) depict and compare LES results for the freely propagating flame obtained using the baseline 128×120 grid described previously and three AMR meshes with 1-, 2- and

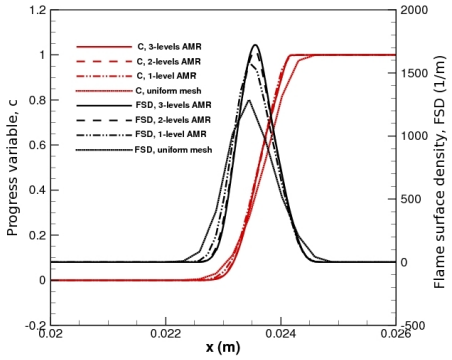

(a) Predicted profiles of $\tilde{c}$, and $\bar{\rho}\tilde{\Sigma}$ for AMR meshes.

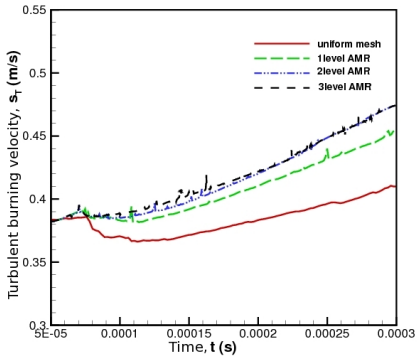

(b) Predicted turbulent burning rate for AMR meshes.

Figure 5.7: Predicted profiles of the progress variable (a), $\tilde{c}$, flame surface density (a), $\bar{\rho}\tilde{\Sigma}$, and turbulent burning rate (b) obtained using uniform mesh with 128×120 cells and AMR meshes with 1-, 2- and 3-levels of refinement.

3-levels of refinement. Again, the filter width, $\Delta x = 2\Delta x_{128\times120}$, is held constant for all cases. The finest AMR mesh consists of 124,800 cells on 390 (16×20) solution blocks.

It can be seen from the figures that a grid-independent result for the FSD is obtained on the finest mesh. Further evidence for this is given in the predicted profiles of the progress variable, $\tilde{c}$, and flame surface density through the flame front of Figure 5.7(a) obtained using the uniform mesh and the three AMR grids. In addition, the plot of the computed turbulent flame speed obtained on the sequence of refined meshes as shown in Figure 5.7(b) also indicates that the AMR procedure rapidly leads to what appears to be a grid-independent result.

5.2.4 Predicted Premixed Flame Structure

The two-dimensional turbulent stoichiometric methane-air flame results are shown in Figure 5.8. The results are generated at a time equal to five eddy turnover time (1.5 ms) based on the Taylor micro scale after initialization of the solution field. Figure 5.8(a) gives contours of the progress variable distribution which varies from the unburnt gas side of the flame as 0 and burnt side as 1. The corresponding FSD

contours are presented in Figure 5.8(b). It can be observed that resolved flame brush remains well structured and strongly wrinkled and there are significant variations of FSD along the flame that is related to the local flame geometry. As time advances, the flame profile becomes more wrinkled, developing a complicated structure with regions of strong resolved curvature.

The contours for the RHS terms in Eq. 3.60 for two-dimensional turbulent methane-air flames are presented in Figure 5.9 and provide insight into both the FSD modelling and physics of the flame. The resolved strain term, as shown in Figure 5.9(a), is an important aspect of the LES flame surface density model. It is zero outside of the flame brush since the FSD is zero, and varies significantly within the resolved flame profile. The effect of this term is primarily related to the production of FSD, but there are also isolated regions of FSD destruction. The contours of the resolved propagation are shown in Figure 5.9(b). This term acts as expected, causing an increase in FSD on the fresh gas side and a decrease on the burnt gas side of the flame. It may be seen from Figure 5.9(c) that the resolved curvature term behaves as a production term in regions where the flame is convex to the reactants and as a destruction term in regions where the flame is concave to the reactants. The addition of these two terms (resolved propagation and curvature) represents the net effects of laminar propagation. The subfilter-scale terms of the FSD model also include the influences of subfilter strain

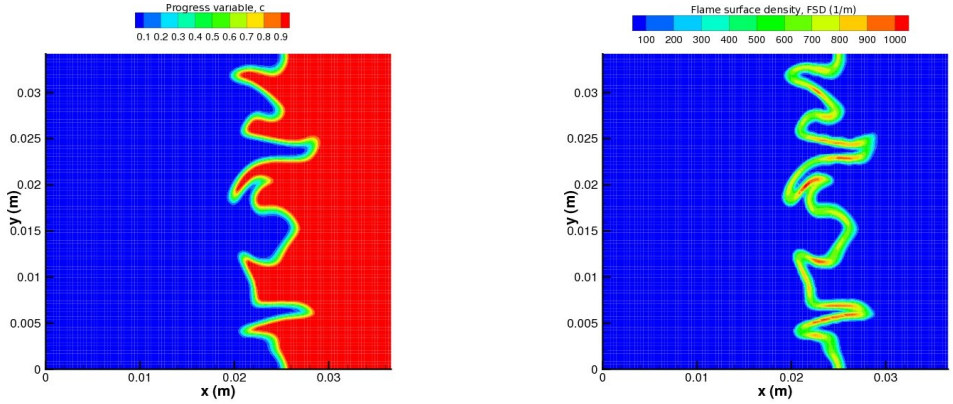

(a) Progress variable contour.

(b) Flame surface density contour.

Figure 5.8: Flame structure for the 2D stoichiometric CH4-air flame at $t = 1.5$ ms.

and subfilter curvature. The predicted distributions of both of these terms are shown in Figure 5.9(d) and Figure 5.9(e), respectively. The subfilter strain is a production term with values corresponding to the local FSD. Conversely, the subfilter curvature acts as a localized destruction of the FSD.

The predicted distribution of the RHS terms in the modelled FSD transport equation are also shown in Figure 5.9(f), so as to asses the relative importance of the contributions of each term to the overall mechanism of flame propagation. Figure 5.9(f) shows the profiles of the RHS terms for the two-dimensional turbulent methane-air flame at 1.5 ms. It is evident from the figure that there is a complex balance of terms through the flame brush resulting in the final net rate of change of FSD. The largest contributions at the trailing edge of the flame arise from resolved curvature and subfilter curvature terms which act in the production and destruction of the FSD, respectively. At the leading edge, the main contributions arise from the resolved and subfilter strain terms and resolved propagation and curvature terms.

5.2.5 Influences of Turbulence Intensity: Comparison of FSD Model and Thickened Flame Models

Simulations of two-dimensional freely propagating flames were also carried out for three different levels of turbulence intensity. The initial ratios of turbulence intensity to laminar flame speed in the unburnt mixture are: $u'/s_{\mathrm{L}} = 6.8,\ 10.4,\ 20.7$. These cases are identified as case A, case B and case C, respectively. A summary of the turbulence scales and flow conditions is listed in Table 5.1, where ϕ is the equivalence ratio, δ_{L} is the laminar flame thickness, λ is the Taylor micro scale, Λ is the integral length scale, and η is the Kolmogorov length scale. The parameters characterizing the initial conditions in the unburnt gas are: $\Lambda = 6.4$ mm; and $\lambda = 0.83$ mm. The dimensions of the domain for the simulations are $L_x = 0.0366$ m and $L_y = 0.0342$ m, and a 128×120 cell uniform computational mesh with 48 solution blocks was employed. Inflow and outflow subsonic boundary conditions were again imposed on the left and right boundaries, respectively, whereas the two remaining boundaries are periodic. For comparison purposes, numerical predictions of the freely propagating

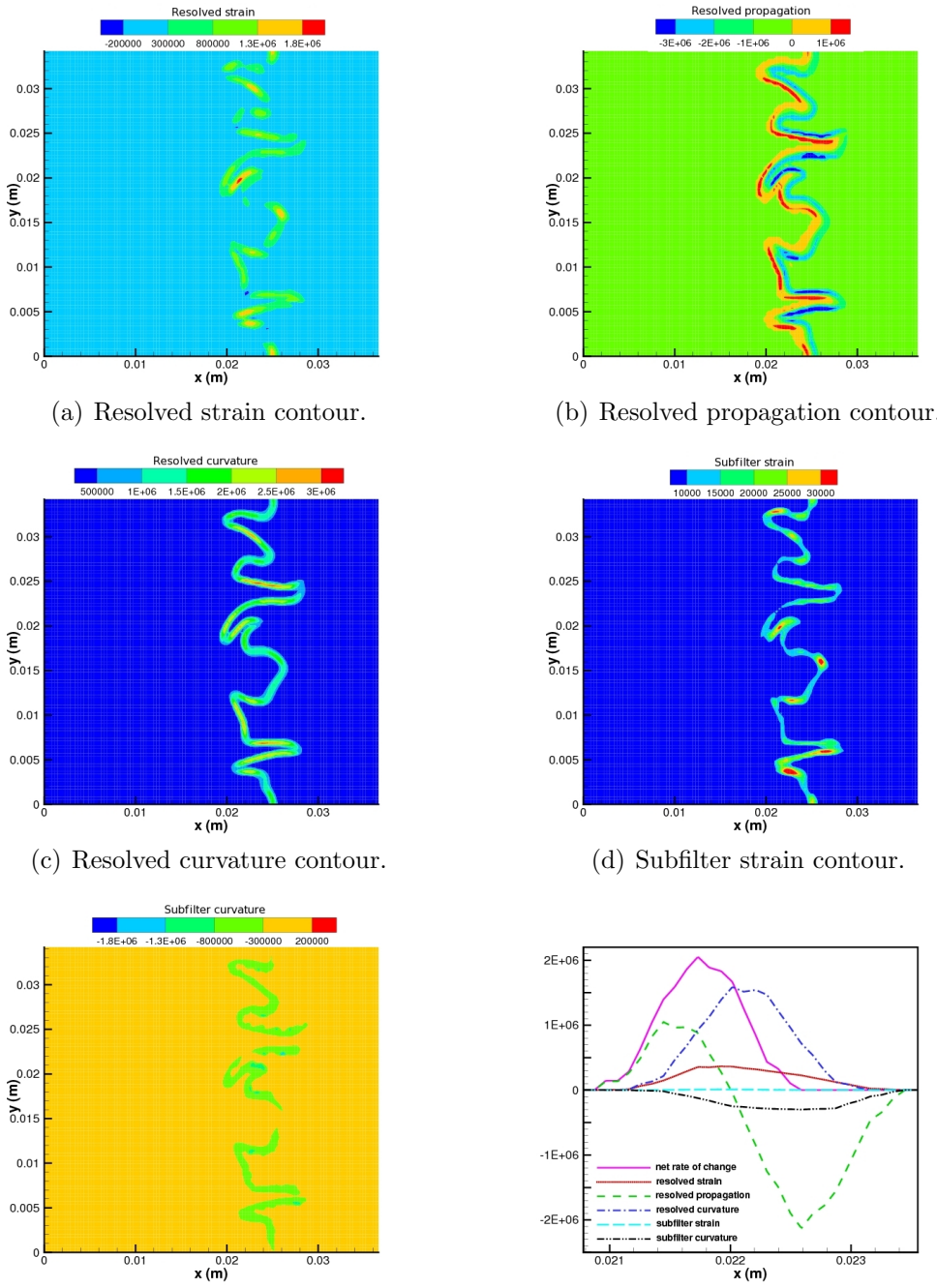

(a) Resolved strain contour.

(b) Resolved propagation contour.

(c) Resolved curvature contour.

(d) Subfilter strain contour.

(e) Subfilter curvature contour.

(f) Budget of all RHS terms.

Figure 5.9: Contours of RHS terms in Eq. 3.60 at $y = 0$ and $z = 0$ plane for 2D stoichiometric CH4-air flame at $t = 1.5$ ms.

flame were also obtained using a thickened flame model with a constant thickening factor, $F = 5$. Figures 5.10(b)–5.10(e) show the predicted contours of methane mass fraction at a time equal to 0.6 ms. This time corresponds to roughly two, three and six eddy turnover times based on Taylor scale for cases A, B and C, respectively.

The predicted contours of the methane mass fraction clearly illustrate the strong influence of the turbulence intensity on the predicted flame structure. For both, the thickened flame and FSD models, there is a significant increase in the resolved flame front wrinkling with turbulent intensity. Comparing the two models, the overall agreement between the predicted flames geometries is rather good. The wrinkling generated by large turbulent structures is very similar for both models. Differences are largely due to the fact that the flame front of the thickened model has been artificially thickened and a greater proportion of the flame wrinkling is therefore modeled. The differences become more evident when the flame is subject to higher turbulence levels, as displayed in Figures 5.10(f) and 5.10(e). In this case, some of the small wrinkled structures that develop at earlier times in the FSD simulation have grown significantly; however, these same structures are not present in the thickened flame simulation.

FSD contours for the three turbulence intensities are shown in Figures 5.11(a), 5.11(c) and 5.11(e). As can be seen, the maximum values of FSD increase with turbulence intensity. Higher turbulence intensities lead to more flame wrinkling, which in turn, produce more flame surface. A point of note is the thickness associated with the FSD contours. There is a thickening of the FSD, which is partly due to lack of resolution of the FSD. As noted above, a numerical challenge associated with the FSD approach is that the required resolution of FSD is higher as compared to the thickened flame

Flame	ϕ	Λ	λ	u'	s_L	δ_L	u'/s_L
CH4-Air		mm	mm	m/s	m/s	mm	
A	1.0	6.4	0.83	2.58	0.38	0.044	6.8
B	1.0	6.4	0.83	3.95	0.38	0.044	10.4
C	1.0	6.4	0.83	7.87	0.38	0.044	20.7

Table 5.1: Summary of the 2D freely propagating turbulence scales and flow conditions.

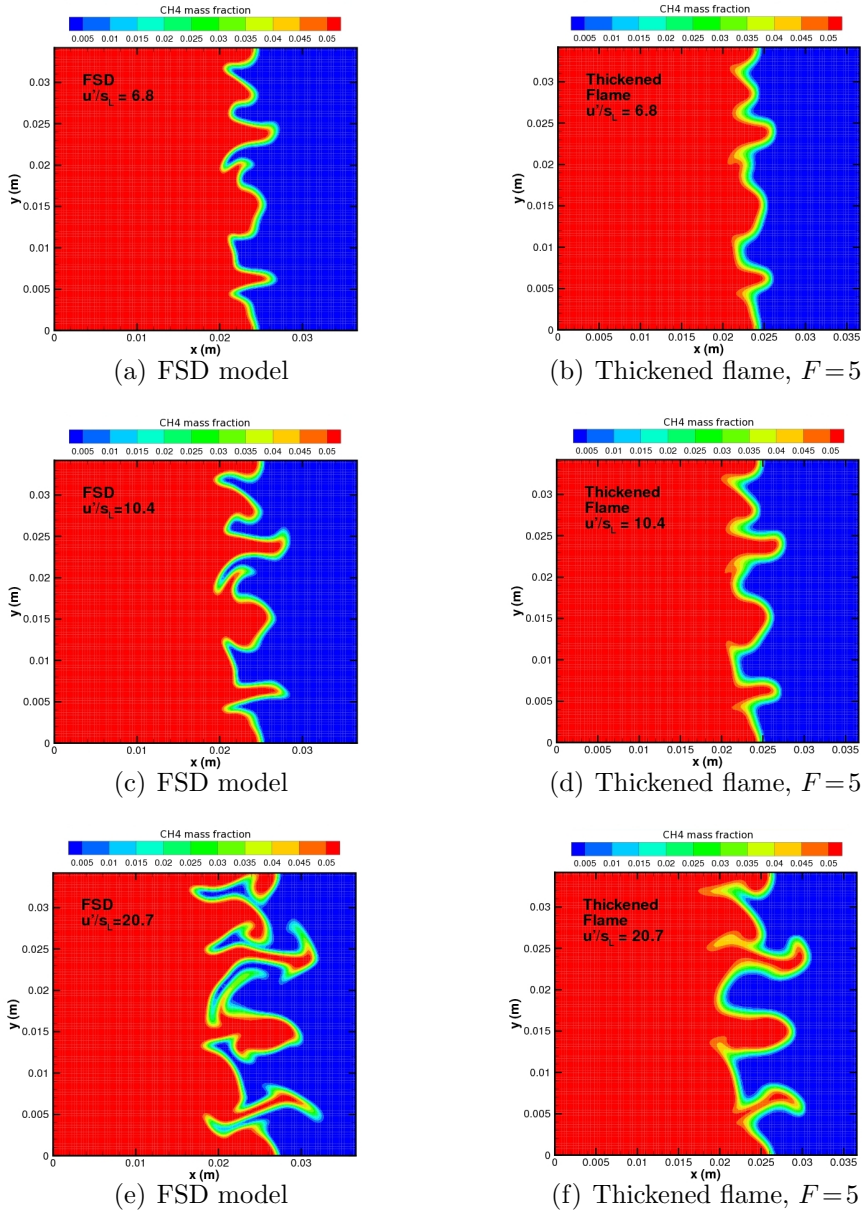

(a) FSD model (b) Thickened flame, $F=5$

(c) FSD model (d) Thickened flame, $F=5$

(e) FSD model (f) Thickened flame, $F=5$

Figure 5.10: Predicted CH_4 contours for cases A-C at 0.6 ms with FSD model and thickened flame model: (a) Case A, $u'/s_L=6.8$, with FSD model, (b) Case A, $u'/s_L=6.8$, with thickened flame model, $F=5$, (c) Case B, $u'/s_L=10.4$, with FSD model, (d) Case B, $u'/s_L=10.4$, with thickened flame model, $F=5$, (e) Case C, $u'/s_L=20.7$, with FSD model, (f) Case C, $u'/s_L=20.7$, with thickened flame model, $F=5$.

model and other similar approaches. On the other hand, a reduced number of transport equations need to be solved when a FSD and progress variable formulation is

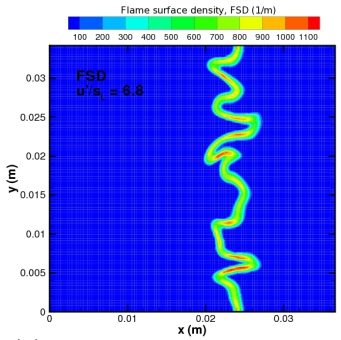

(a) FSD contours, FSD model

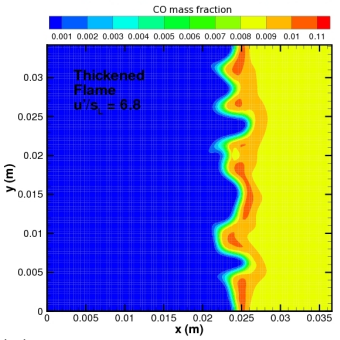

(b) CO mass fraction, Thickened flame, $F=5$

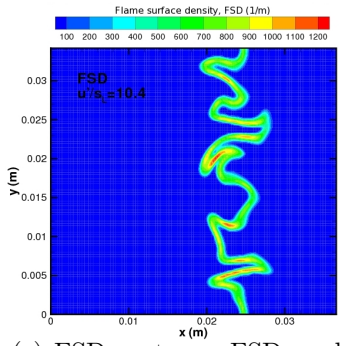

(c) FSD contours, FSD model

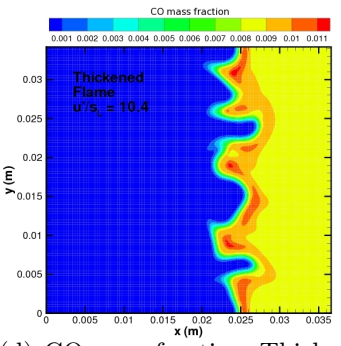

(d) CO mass fraction, Thickened flame, $F=5$

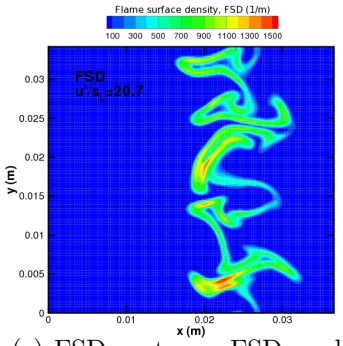

(e) FSD contours, FSD model

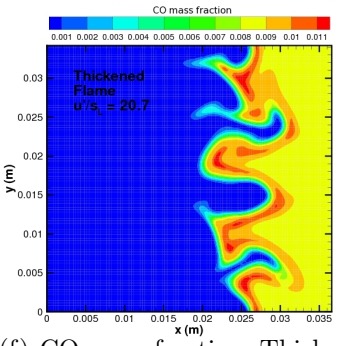

(f) CO mass fraction, Thickened flame, $F=5$

Figure 5.11: Predicted CO and FSD contours for cases A-C at 0.6 ms with FSD model and thickened flame model: (a) Case A, $u'/s_{\mathrm{L}}=6.8$, with FSD model, (b) Case A, $u'/s_{\mathrm{L}}=6.8$, with thickened flame model, $F=5$, (c) Case B, $u'/s_{\mathrm{L}}=10.4$, with FSD model, (d) Case B, $u'/s_{\mathrm{L}}=10.4$, with thickened flame model, $F=5$, (e) Case C, $u'/s_{\mathrm{L}}=20.7$, with FSD model, (f) Case C, $u'/s_{\mathrm{L}}=20.7$, with thickened flame model, $F=5$.

employed, which, from the computational viewpoint, is advantageous. Another advantage of the FSD approach is the separation of complex chemistry from turbulence in which chemistry modeling is simply incorporated through the laminar flame speed and heat release parameter.

Since the thickened flame approach offers some potential of dealing with more complex chemical kinetic schemes and detailed transport, results obtained for an intermediate species like CO are considered next. As discussed previously in Section 3.2.2 for the FSD model, the mass fraction of each species is derived based on the one-step global reaction and the definition of progress variable. A limitation of the current FSD model pertains to solving complex chemical reactions and obtaining intermediate species. Figures 5.11(b), 5.11(d) and 5.11(f) show the predicted CO mass fraction contours using the thickened flame model approach. It should be noted that the thickened flame results were obtained using the algorithm developed by Hernandez-Perez [156]. For the three different cases, the largest concentrations of CO tend to occur in regions where the flame front is convex towards the reactants. This is in agreement with direct numerical simulation results reported in references [157,158]. These regions generally coincide with zones where the flame undergoes downstream interaction, which have been reported to be the main areas for CO production. In these regions the CO oxidation layer is curtailed. It is interesting to note that despite the fact that only a two-step reaction mechanism is used in the LES of the premixed flames, important features regarding the interaction between turbulence and chemistry have been captured with thickened flame model.

The turbulent burning rates for the three different values of turbulent intensity have been computed, based on the integrated FSD and the integrated consumption rate of fuel, in the FSD and thickened flame simulations, respectively. The corresponding expressions for FSD and the thickened flame burning rates are given by

$$s_{\mathrm{T}} = \frac{s_{\mathrm{L}}}{L_y} \int_A \bar{\rho} \tilde{\Sigma} \mathrm{d}A, \tag{5.1}$$

and

$$s_{\mathrm{T}} = \frac{1}{\bar{\rho}_{\mathrm{r}} \tilde{Y}_{\mathrm{F}} L_y} \int_A \overline{\dot{\omega}_{\mathrm{F}}} \mathrm{d}A, \tag{5.2}$$

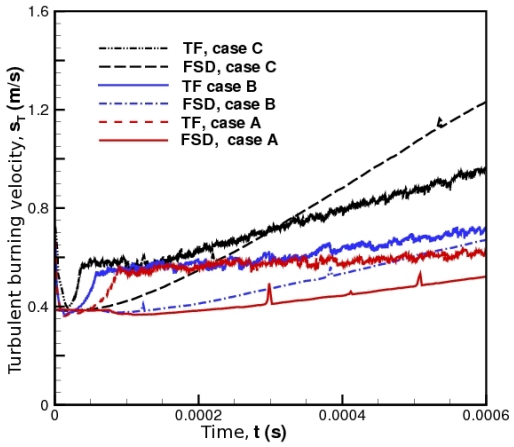

Figure 5.12: Predicted turbulent burning rates for freely propagating flame in two-dimensional decaying isotropic turbulent fields for Cases A-C.

where $\bar{\rho}_{\mathrm{r}}$ is the reactants density and $\tilde{Y}_{\mathrm{F}}$ is the fuel mass fraction in the reactants.

The predicted turbulent burning rates obtained for both the thickened flame and FSD models for cases A-C are shown in Figure 5.12. From the figure, it can be seen that there is a short period of adjustment to the initial conditions until the burning rates attain the laminar flame speed. After this initial period of adjustment, the burning rates generally increase while the flame front is wrinkled by the turbulent flow field. The fuel consumption rate is clearly enhanced by turbulence as more flame surface is produced by the wrinkling of the flame front.

For both models, the computed burning rates follow the same trend. As the turbulence level is increased, more wrinkling is generated, resulting in a corresponding increase in the turbulent burning rates. The predicted turbulent flame speeds are quantitatively similar for low turbulence intensities, however, for high turbulence intensity the FSD model yields a higher flame speed.

5.2.6 Influences of Fuel Type

One of the advantages of FSD subfilter-scale model for LES is that it is relatively easy to apply the model to the combustion of different fuels. All that is required is

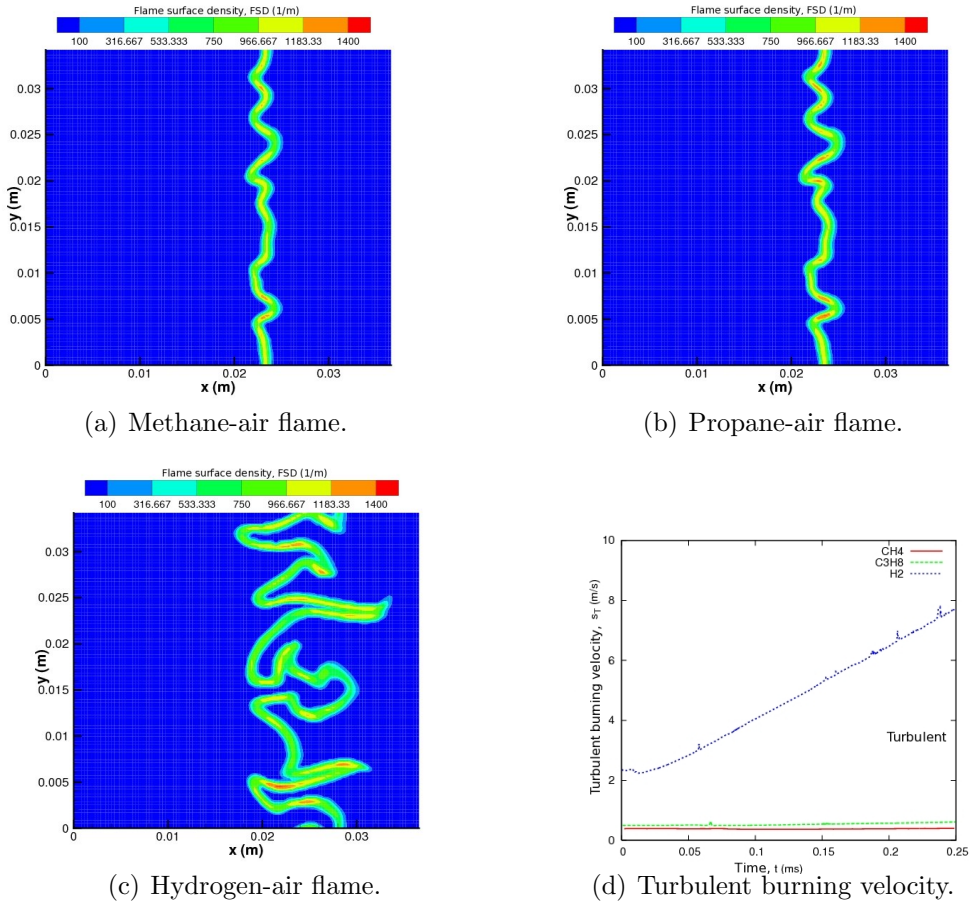

(a) Methane-air flame.

(b) Propane-air flame.

(c) Hydrogen-air flame.

(d) Turbulent burning velocity.

Figure 5.13: Predicted FSD contours for different fuels: (a) Methane-air flame, (b) Propane-air flame, (c) Hydrogen-air flame, and (d) turbulent burning rate for three different fuels.

the calculation of the laminar flame speed and relationships for the mass fraction of the various reactants and products in terms of the progress variable. Note that this may also be viewed as a drawback as the chemistry of intermediate species can not be properly represented without introducing additional progress variables. Here the validation for different fuels has been carried out for methane-air, propane-air, and hydrogen-air two-dimensional freely propagating flames. The computations were carried out with a ratio of turbulence intensity to laminar flame speed of 6.5 for all three fuels, and for a physical time of 0.25 ms, which is approximately one eddy turnover time for the methane-air and the propane-air mixtures, and almost

five eddy turnover time for the hydrogen-air mixture. The laminar flame speeds for the three different fuels are 0.38 m/s (CH4), 0.5 m/s (C3H8), and 2.38 m/s (H2). Figures 5.13(a)–5.13(c) depict the predicted FSD solutions for the three fuels. It may be observed that methane-air and propane-air have very similar flame wrinkling and structure, but the hydrogen-air flame exhibits a much higher degree of wrinkling as should be expected.

5.3 Three-Dimensional Premixed Turbulent Freely Propagating Methane-Air Flames

Following the verification studies of flame propagation in one- and two-dimensions, further verification of the implementation of the FSD subfilter-scale model with the LES framework has been sought by considering fully three-dimensional simulations of freely propagating flames in homogeneous isotropic decaying turbulent fields. Similar to the two-dimensional simulations described previously, the three-dimensional turbulent flames are initialized by introducing a planar laminar stoichiometric methane-air premixed flame onto a computational domain containing the isotropic turbulent field using the procedure developed by Rogallo [155]. Also as in the two-dimensional simulations, turbulence fields of three different turbulence intensities were considered. These cases are identified as case D, case E, and case F, respectively, and the parameters characterizing the initial turbulent field in the unburnt mixture for each of the cases are as follows: relative turbulence intensity, $u'/s_{\mathrm{L}} = 3.3$ (case D), 7.25 (case E), 14.38 (case F); integral length scale, $\Lambda = 1.635$ mm (case D), 1.79 mm (case E), 1.79 mm (case F); Taylor micro scale, $\lambda = 0.442$ mm (case D), 0.46 mm (case E), 0.46 mm (case F); Komogorov scale, $\eta = 0.052$ mm (case D), 0.029 mm (case E), 0.029 mm (case F); laminar flame speed, $s_{\mathrm{L}} = 0.40$ m/s (case D), 0.40 m/s (case E), 0.2 m/s (case F); and flame thickness, $\delta_{\mathrm{L}} = 0.052$ mm (case D), 0.029 mm (case E), 0.029 mm (case F). In addition, in order to investigate the influences of stoichiometry, a lean case has also been carried out with relative turbulence intensity $u'/s_{\mathrm{L}} = 14.38$ (case G) and equivalent ratio $\phi = 0.7$. A summary of the turbulence scales and flow

conditions for the three testing cases is provided in Table 5.2.

A cube-shaped physical domain was considered for the simulations with dimensions of 0.01 m $\times$ 0.01 m $\times$ 0.01 m. Numerical results were obtained using a refined mesh in the flame propagating direction. The computational domain was discretized using a $240 \times 60 \times 60 = 864,000$ cell mesh with the cells equally distributed on 4096, $16 \times 4 \times 4$-cell, solution blocks. This corresponds to a mesh spacing of $\Delta x = 0.04$ mm, $\Delta y = 0.16$ mm, and $\Delta z = 0.16$ mm. A filter width of $\Delta = 2\Delta x = 0.08$ mm $= 0.1\delta_{\mathrm{L}}$ was used when performing the LES. The design of this mesh is based on the study of the two-dimensional freely propagating flames with AMR scheme, Section 5.2.3. The simulation results were carried out for one eddy turnover time based on the integral length scale for all three cases. This corresponds to the physical times of 1.3 ms ($u'/s_{\mathrm{L}} = 3.3$), 0.65 ms ($u'/s_{\mathrm{L}} = 7.25$), and 0.33 ms ($u'/s_{\mathrm{L}} = 14.38$), respectively.

5.3.1 Influences of Turbulence Intensity

Numerical predictions of the three-dimensional freely propagating flames for cases D, E, and F, obtained using the FSD model are depicted in Figure 5.14. The predicted iso-surfaces of the progress variable corresponding to $c = 0.5$ at $t = 0.33$ ms are shown. The initial turbulence velocity field is also shown in Figure 5.14(a). The fully three-dimensional structures of the resolved flame surfaces are apparent in the figure. The wrinkling of the initial planar flame front is clearly illustrated. Furthermore, the flame front wrinkling is noticeably increased with increasing turbulence intensity. The increased wrinkling of the flame front also results in a corresponding increase in the predicted burning rate and hence flame propagating speed.

Flame	ϕ	Λ	λ	η	u'	s_{L}	δ_{L}	u'/s_{L}	$\Lambda/\delta_{\mathrm{L}}$
CH4-Air		mm	mm	mm	m/s	m/s	mm		
D	1.0	1.635	0.442	0.05174	1.33	0.403	0.05	3.30	30.46
E	1.0	1.790	0.460	0.02935	2.92	0.403	0.05	7.25	33.34
F	1.0	1.790	0.460	0.02935	5.79	0.403	0.05	14.38	33.34
G	0.7	1.790	0.460	0.02935	2.92	0.201	0.11	14.38	33.34

Table 5.2: Summary of the freely propagating turbulence scales and flow conditions.

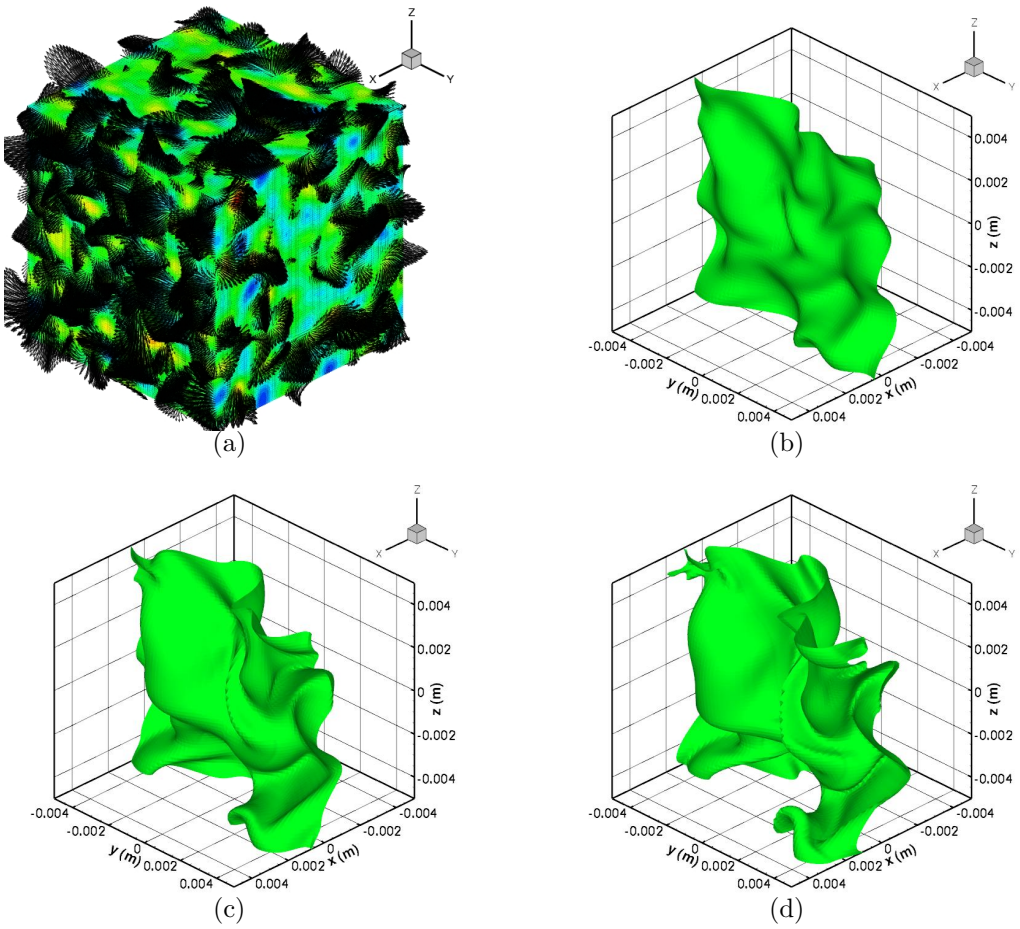

Figure 5.14: (a) Initial turbulent flow field. Predicted iso-surfaces of c corresponding to $c=0.5$ at time $t=0.33$ ms for stoichiometric cases with turbulence intensities: (b) $u'/s_L=3.3$ (case D) (c) $u'/s_L=7.25$ (case E) and (d) $u'/s_L=14.38$ (case F).

The predicted turbulence burning rates for different turbulence intensities are presented in Figure 5.15(a). It should be noted that the longer simulation time is still needed to reach the quasi-steady turbulent burning rates for cases D, $u'/s_L=3.30$, and E, $u'/s_L=7.25$, in Figure 5.15(a). Figure 5.15(b) illustrates the time variation of the total kinetic energy, the resolved kinetic energy, and the subfilter kinetic energy for the three-dimensional flame propagation problem with a turbulence intensity $u'/s_L=7.25$ (case E). It is shown that most of the total kinetic energy has been resolved and only a small portion of the energy, the subfilter kinetic energy, has been modelled. This can be explained by the refined mesh used in the direction of flame propagation which

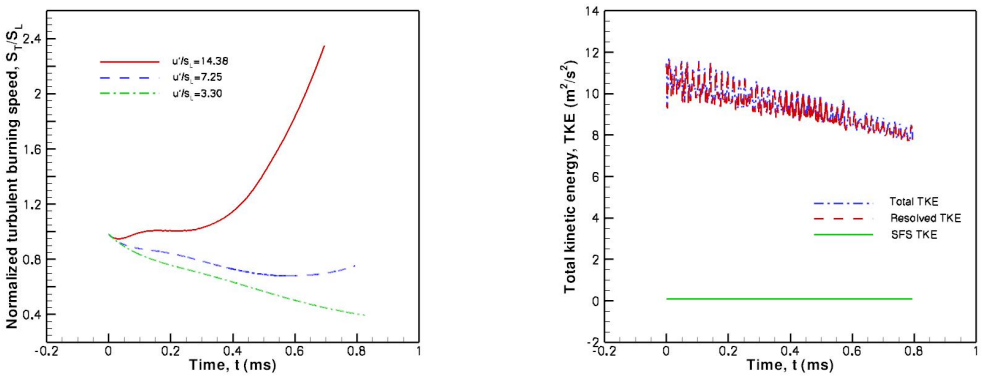

(a) (b)

Figure 5.15: (a) Turbulence burning rate for stoichiometric cases with three different turbulence intensities (case D, E, and F). (b) Turbulent kinetic energy for the stoichiometric case with turbulence intensity $u'/s_{\mathrm{L}} = 7.25$ (case E).

is required in order to accurately resolve the flame surface density based on resolution studies for two-dimensional flames considered previously.

The wrinkled structure of the premixed flame fronts are further presented in the contours of the progress variable, c, and FSD in the x-z plane, Figure 5.16. It may be observed that increased relative turbulence intensity increases the resolved wrinkling of the flame surface, as well as the maximum values of FSD. It also may be pointed out that the resolved flame structure is slightly tightened at the increased turbulence level. The reason for that is the subfilter flame strain term is scaled with the efficiency function Γ_k, which is an increasing function of the subfilter kinetic energy, $\tilde{k}$.

5.3.2 Time Evolution of Flame Profiles

In order to see clearly the time evolution of the freely-propagating flame profiles, simulation results for case E, in which the relative turbulence intensity is 7.25, are shown in Figures 5.17(a) and 5.17(b) for two different instances in time. The predicted iso-surfaces of the progress variable for $c = 0.5$ are shown in the figures at times $t = 0.33$ ms and $t = 0.65$ ms, respectively. Correspondingly, Figures 5.17(c)–5.17(f) provide the predicted contours of the progress variable and flame surface density in the x-z plane. From these figures, it can be seen that the resolved flame brushes remain well

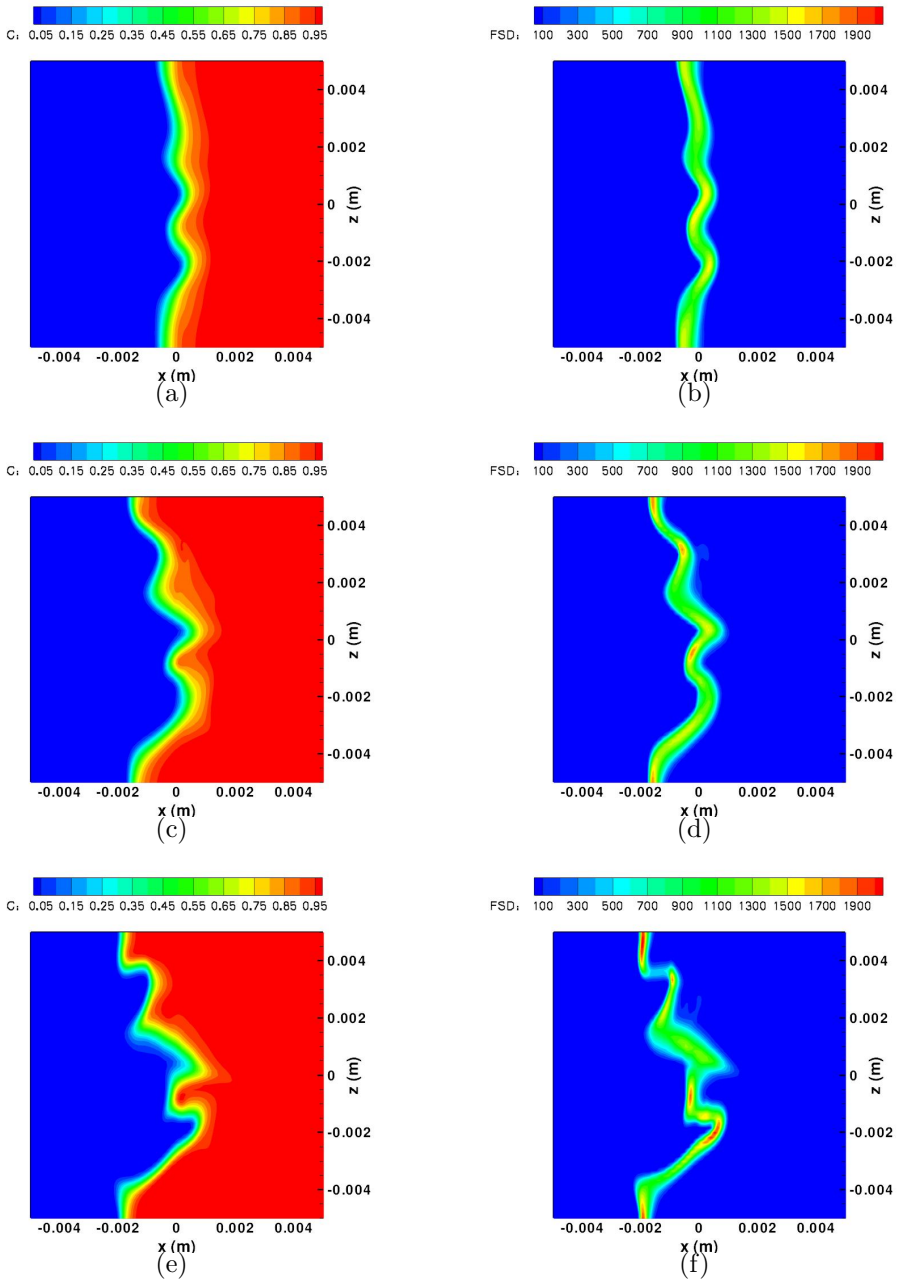

Figure 5.16: Predicted contours of c and FSD at x-z plane for the stoichiometric cases with turbulence intensities: (a) and (b) $u'/s_{\mathrm{L}}=3.3$ (case D), (c) and (d) $u'/s_{\mathrm{L}}=7.25$ (case E), and (e) and (f) $u'/s_{\mathrm{L}}=14.38$ (case F).

structured and there are significant variations of FSD along the flame that are related to the local flame geometry. The significant wrinkling of the flame surface is captured

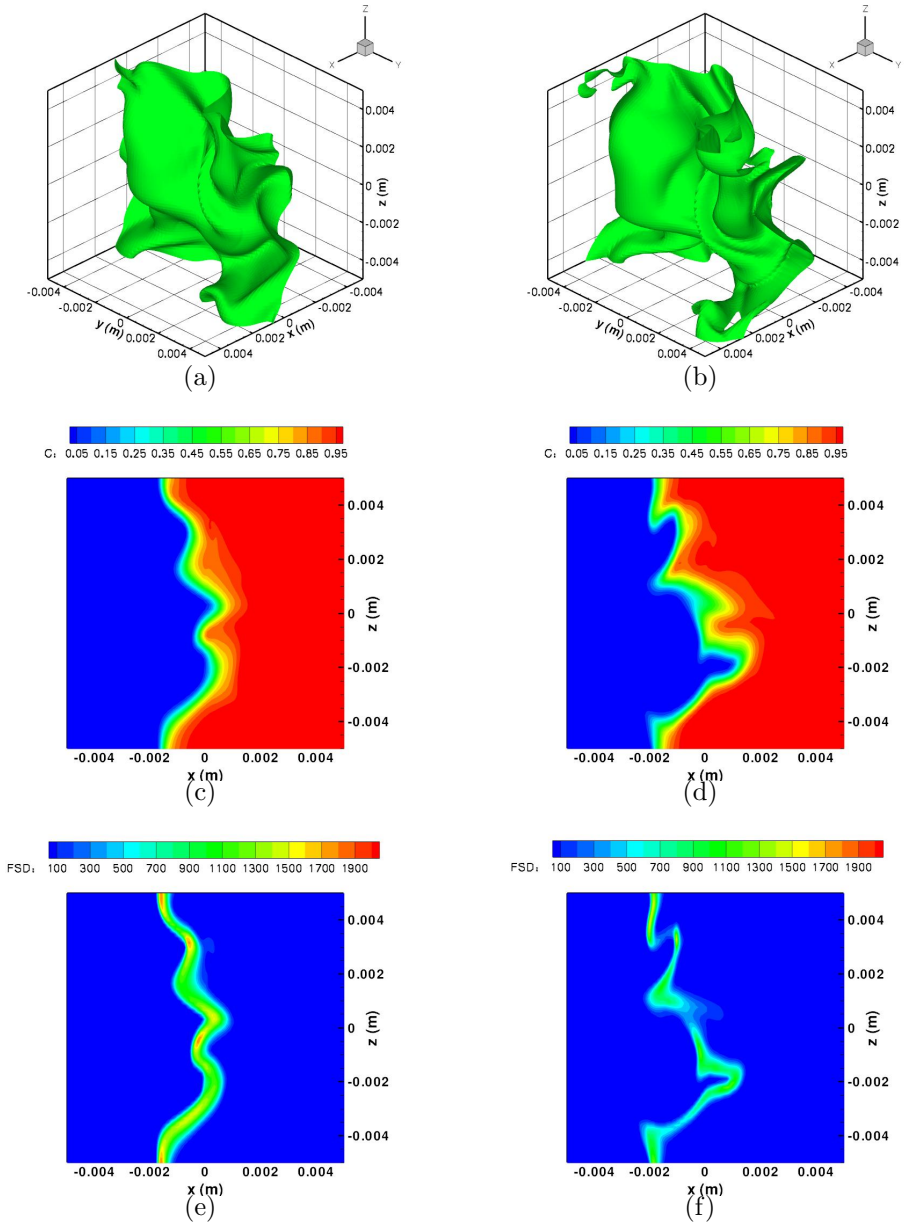

Figure 5.17: Predicted iso-surfaces of $c = 0.5$ for the stoichiometric case with turbulence intensity $u'/s_L = 7.25$ (case E) at time (a) $t = 0.33$ ms and (b) $t = 0.65$ ms, predicted contours of c at x-z plane for turbulence intensity $u'/s_L = 7.25$ at time (c) $t = 0.33$ ms and (d) $t = 0.65$ ms, predicted contours of FSD at x-z plane for turbulence intensity $u'/s_L = 7.25$ at time (e) $t = 0.33$ ms and (f) $t = 0.65$ ms

by the LES methodology. As time advances, the flame profiles become more wrinkled, developing a complicated structure with regions of strong resolved curvature. The

flame generally consists of large areas where the curvature is convex to the reactants and smaller areas featuring tighter concave curvatures. This behavior has also been found in DNS studies of flame structure (see, for example, Cant *et al.* [153]).

5.3.3 Behavior of Modelled Terms in FSD Closure

As for the two-dimensional flames considered above, the ability of the FSD model to provide insight into the structure and evolution of the three-dimensional flame surface is highlighted by considering the production and destruction terms that appear in the FSD transport equation. Figure 5.18 shows contours of the numerical values of the terms on the RHS of the modelled transport equation (Eq. 3.60) for case E with the relative turbulence intensity of 7.25 at time $t = 0.65$ ms. The resolved propagation term, P_{res} (Figure 5.18(b)), is causing an increase of the FSD on the fresh gas side and a decrease on the burnt gas side. The resolved curvature term, C_{res} (Figure 5.18(c)), acts as a production term in the regions where the flame is convex to the reactants and as a destruction term in the regions where the flame is concave to the reactants. The addition of the two terms, P_{res} and C_{res}, represents the net effects of laminar propagation. The ability of LES to exploit the partial resolution of the flame brush is highlighted by Figure 5.18(b) and 5.18(c). There are strong spatial variations in the resolved terms that would simply not be observed in a RANS simulation. The resolved strain term (Figure 5.18(a)) is acting, as expected, as a production term for the FSD. The subfilter strain term (Figure 5.18(d)) and subfilter curvature term (Figure 5.18(e)) act as the production and destruction terms for the flame surface, respectively. The sum of all the terms from the RHS of the transport equation for the FSD dictates the net rate of change of the flame surface area. Figure 5.18(f) illustrates the strongly dynamic nature of the flame propagation process through the spatial variations of the net rate of change of FSD.

The structure of the flame profile is the result of many contributions to production and destruction taken over a significant time period. This underlines the need for models based on the solution of a full transport equation of FSD. Figure 5.19 gives the budget of the RHS terms for cases D, E, and F at time $t = 0.33$ ms, which are

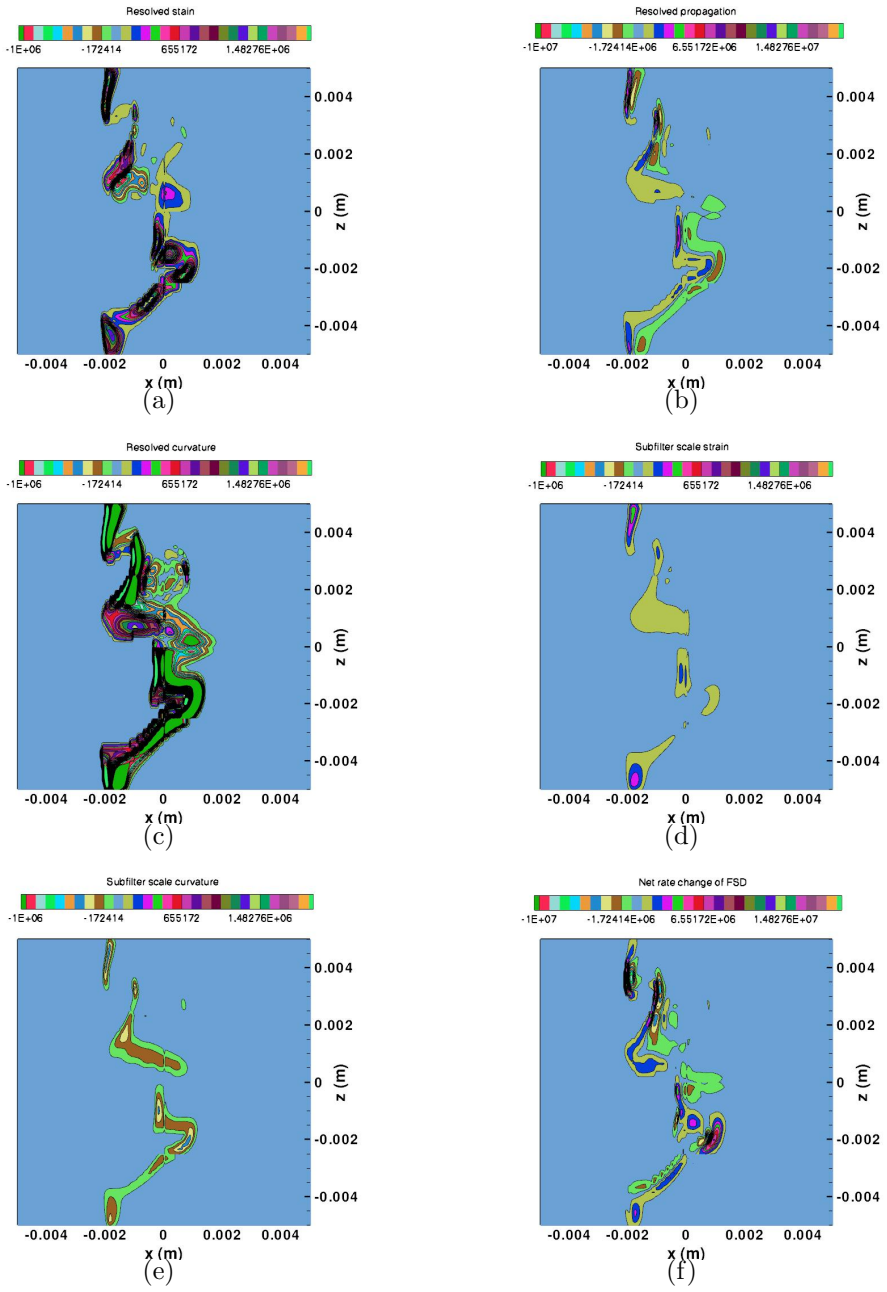

Figure 5.18: Predicted contours of RHS terms of Eq. 3.60 at x-z plane for the stoichiometric case with the turbulence intensity $u'/s_{\mathrm{L}} = 7.25$ (case E) at time $t = 0.65$ ms. (a) resolved strain term, (b) resolved propagation term, (c) resolved curvature term, (d) SFS strain term, (e) SFS curvature term, and (f) net rate of the change.

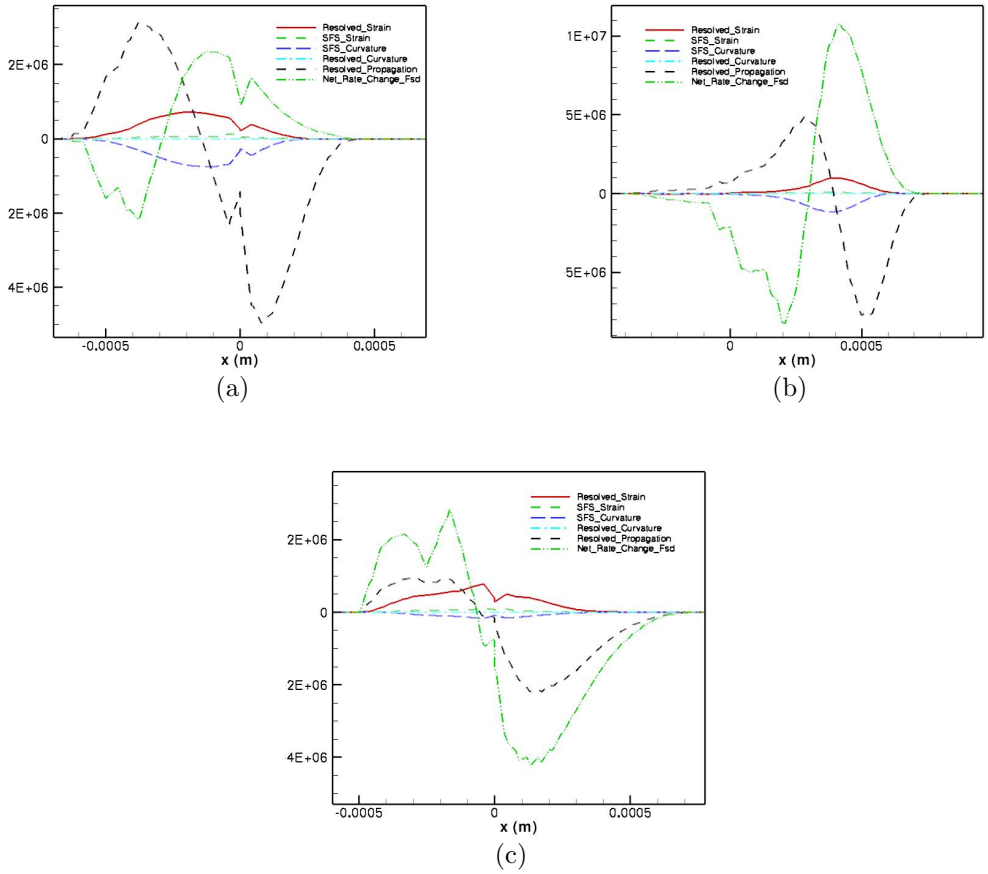

Figure 5.19: RHS term budget of Eq. 3.60 for stoichiometric cases with turbulence intensities: (a) $u'/s_L = 3.3$ (case D), (b) $u'/s_L = 7.25$ (case E), and (c) $u'/s_L = 14.38$ (case F).

the profiles normal to the three-dimensional flame front along one line. It may be observed that the increased relative turbulence intensity results in an increase in the flame brush thickness. In addition, the resolved propagation, curvature and strain terms become less significant with increased turbulence intensity.

5.3.4 Influences of Stoichiometry

In many practical applications, such as stationary gas turbines for power generation, there is a strong interest in achieving lean premixed combustion due to the advantages of higher thermal efficiency and lower NO_x emissions. As a follow on

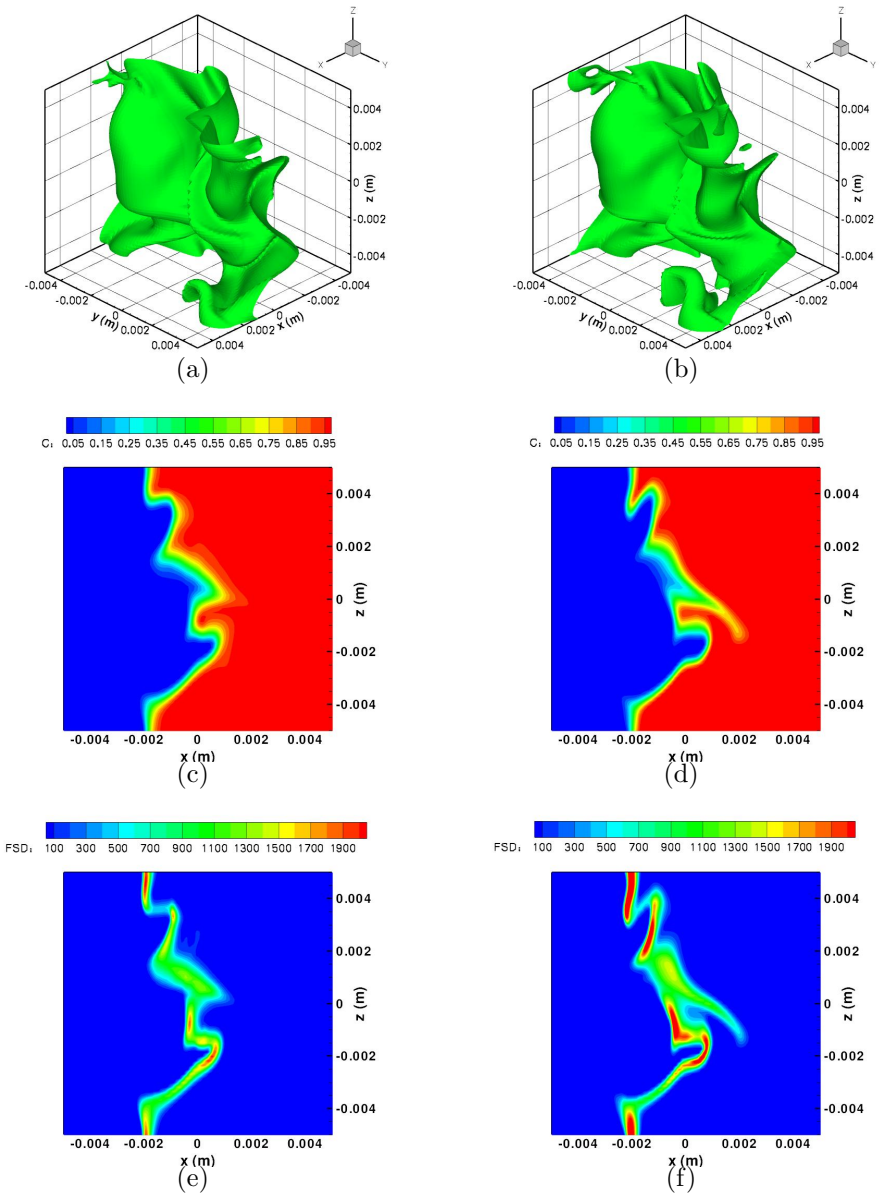

Figure 5.20: Comparison of predicted iso-surfaces of $c = 0.5$, contours of c and FSD for stoichiometric (case F) and lean (case G) flames with turbulence intensity $u'/s_L = 14.38$ at time $t = 0.33$ ms; (a) Predicted iso-surfaces of $c = 0.5$ for stoichiometric flame; (b) Predicted iso-surfaces of $c = 0.5$ for lean flame; (c) Predicted contours of c at x-z plane for stoichiometric flame; (d) Predicted contours of c at x-z plane for lean flame; (e) Predicted contours of FSD at x-z plane for stoichiometric flame; (f) Predicted contours of FSD at x-z plane for lean flame.

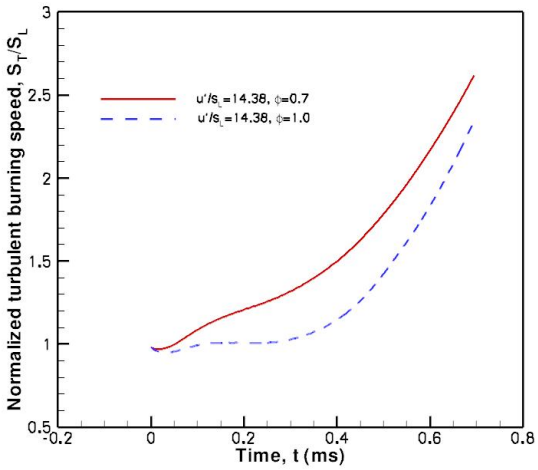

Figure 5.21: Comparison of predicted turbulent burning rates of stoichiometric (case F) and lean (case G) flames with turbulence intensity $u'/s_{\mathrm{L}} = 14.38$.

to the preceding numerical results for freely propagating stoichiometric methane-air premixed flames, numerical simulation of a lean premixed flame was also considered here with a relative turbulence intensity of $u'/s_{\mathrm{L}} = 14.38$ (case G) at time $t = 0.33$ ms. In addition, in order to compare the turbulence burning rate for stoichiometric (case F) and lean (case G) flames, numerical simulation has also been carried out until time $t = 0.7$ ms for both cases. The comparison of predicted iso-surfaces of $c = 0.5$ and contours of c and FSD for these two stoichiometric and lean flames are presented in Figure 5.20. It is apparent that the predicted lean premixed flame displays increased wrinkling and a more diffusive flame front than the stoichiometric flame (Figure 5.20(b) and Figure 5.20(a), Fig 5.20(d) and Fig 5.20(c)). Also, the values of the predicted contours of FSD are higher for the lean flame than for the stoichiometric flame as shown in Fig 5.20(f) and Figure 5.20(e). This behavior is also reflected in the comparison of the predicted turbulence burning rates for the lean and stoichiometric flames given in Figure 5.21, in which the normalized or relative turbulent burning rate for the lean case is found to be higher than for that of the stoichiometric case. Previous experimental and LES results of Kaminski *et al.* [159] suggest that there may be some dependence of flame wrinkling on stoichiometry and that lean flames can be destabilized even at relatively low turbulence intensities for

conditions under which a stoichiometric flame is only moderately affected. It should be noted here that the absolute value of the turbulent burning rate for the lean case is actually lower than the stoichiometric case. The reason that the normalized turbulent burning rate for the lean case becomes higher is because of the apparent increased wrinkling of the flame front under lean conditions.

5.4 Three-Dimensional Premixed Turbulent Methane-Air Bunsen Flames

Having carried out a partial validation of the proposed subfilter scale FSD model and LES implementation for one-, two-, and three-dimension premixed laminar and turbulence flames, we are now in a position to consider the numerical simulation of turbulent laboratory-scale flames and comparison of predicted flame behavior and structure to experimental measurements. There have been a variety of simplified turbulent premixed flame configurations studied experimentally by various researchers. Recent examples include the studies by Sattler *et al.* [160] of a turbulent V-flame, Shepherd *et al.* [161] of a swirl-stabilized flame, Most *et al.* [162] of a bluff-body stabilized flame, Chen *et al.* [163] of Bunsen and stagnation flames, and Filatyev *et al.* [164] of slot burner flame. Experimental diagnostics have advanced understanding of basic flame physics for these idealized laboratory flames and as well as aided in the development of models that can be used for engineering design. In addition, several DNS studies have been presented for a laboratory-scale slot burner flame and V-flame by Bell *et al.* [165, 166] and a lean Bunsen flame by Sankaran *et al.* [167].

In this thesis, LES was performed with the FSD subfilter-scale model for the laboratory-scale turbulent premixed Bunsen-type flames considered in the experimental work of Yuen and Gülder [4, 5] and the resulting numerical predictions have been carefully compared to the experimental measurements. The experiments were conducted for 31 different premixed Bunsen-type flame conditions. There were 15 different methane-air flames considered in the experimental work under various conditions with equivalence ratios of $\phi = 0.6 - 1.0$, non-dimensional turbulence intensities

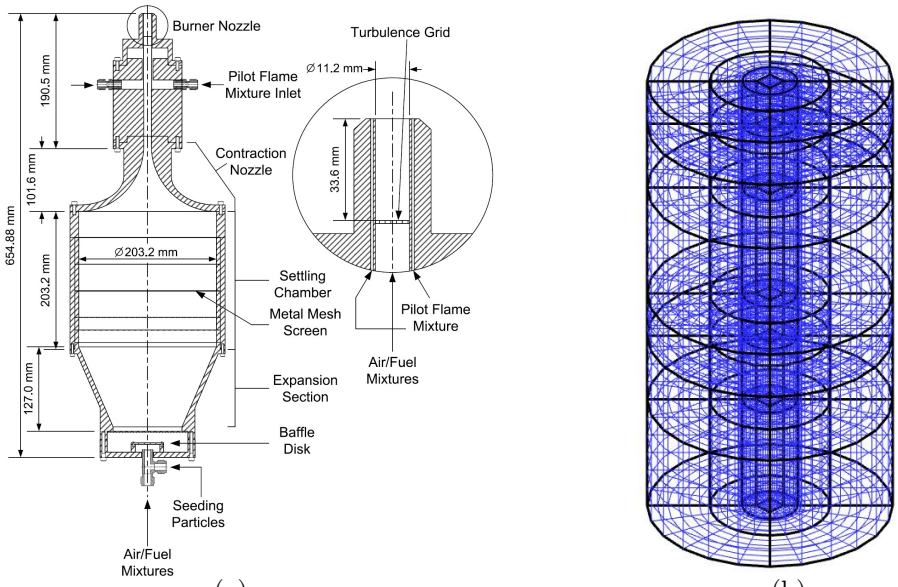

Figure 5.22: (a) Schematic of the premixed Bunsen-type flame [4]. (b) Computational mesh for the premixed Bunsen-type flame.

of $u'/s_{\mathrm{L}} = 3.2 - 24.1$, integral length scales of $\Lambda = 1.62 - 1.79$, turbulent Reynolds numbers of $\mathrm{Re} = 96 - 242$, and Karlovitz numbers of $\mathrm{Ka} = 1.1 - 37.7$. Another 16 flames were considered for propane-air mixtures with equivalence ratio in the range $\phi = 0.7 - 1.0$, non-dimensional turbulence intensities of $u'/s_{\mathrm{L}} = 2.7 - 20.3$, integral length scales of $\Lambda = 1.61 - 1.83$, turbulent Reynolds numbers of $\mathrm{Re} = 83 - 311$, and Karlovitz numbers of $\mathrm{Ka} = 0.8 - 23.3$. All of the 31 flames considered by Yuen and Gülder straddle the border between the flamelet and thin reaction zones given by $\mathrm{Ka} = 1$ on the premixed turbulent combustion regime diagram (refer to Chapter 1) and correspond to typical working conditions for real gas-turbine combustors. On the other hand, the geometry set up of the Bunsen burner, as shown in Figure 5.22(a), is fairly easy to represent using a cylindrical multi-block numerical mesh as depicted in Fig 5.22(b). The experimental premixed turbulent conical flames [4] were produced by using a Bunsen burner with an inner nozzle diameter of $d = 11.2$ mm. Turbulence levels were regulated by perforated plates located at 3-diameter lengths upstream of the burner nozzle. Particle image velocimetry (PIV) was used to measure instan-

taneous velocity field of the experimental conditions studied. Planar laser Rayleigh scattering was used to capture the flame front images.

5.4.1 Cases of Interest and Bunsen Flame Setup

In the present study, four of the experimental cases of Yuen and Gülder [4,5] were considered: two stoichiometric methane-air premixed flames with relative turbulence intensities of $u'/s_{\mathrm{L}} = 3.3$ (case H) and $u'/s_{\mathrm{L}} = 7.25$ (case I) and two lean methane-air premixed flame with relative turbulence intensities of $u'/s_{\mathrm{L}} = 6.55$ (case M) and $u'/s_{\mathrm{L}} = 14.38$ (case N). In addition, in order to explore more fully the influence of turbulence on the premixed Bunsen-type flames, four other flames, not considered in the experimental work, were also simulated. Two of the additional simulated flames were stoichiometric methane-air premixed flames with relative turbulence intensities of $u'/s_{\mathrm{L}} = 14.38$ (case J) and $u'/s_{\mathrm{L}} = 24.1$ (case K), respectively, and the other two flames were lean methane-air premixed flames with relative turbulence intensities of $u'/s_{\mathrm{L}} = 3.3$ (case L) and $u'/s_{\mathrm{L}} = 24.1$ (case P). The turbulence scales and flow conditions for all of these eight cases are summarized in Table 5.3. Furthermore, the locations corresponding to the operating conditions for these eight flames (cases H–P) on the premixed turbulent combustion regime diagram are given in Figure 5.23, which clearly shows that the eight flames lie above the flamelet regime (above the $\mathrm{Ka} = 1$ line) and are fully inside the so-called thin-reaction zones regime. For this reason, the eight flames of interest present significant challenges to the FSD-LES modelling considered herein, and indeed would challenge any modelling based on the laminar flamelet concept.

The geometry of the Bunsen burner is shown in Figure 5.22(a). As depicted in Figure 5.22(b), a cylindrical-shaped computational domain was used with a diameter of $5d$ and a height of $10d$, such that the influence of the far-field domain boundaries was minimized. Note that as indicated above, $d = 11.2$ mm for the burner. The domain was discretized using a multi-block, body-fitted, hexahedral mesh consisting of 1664 $12 \times 12 \times 8$ blocks and a total of $1,916,928$ computational cells. There were $1,024$ cells in the vertical direction, 48 cells in the azimuthal direction, and approxi-

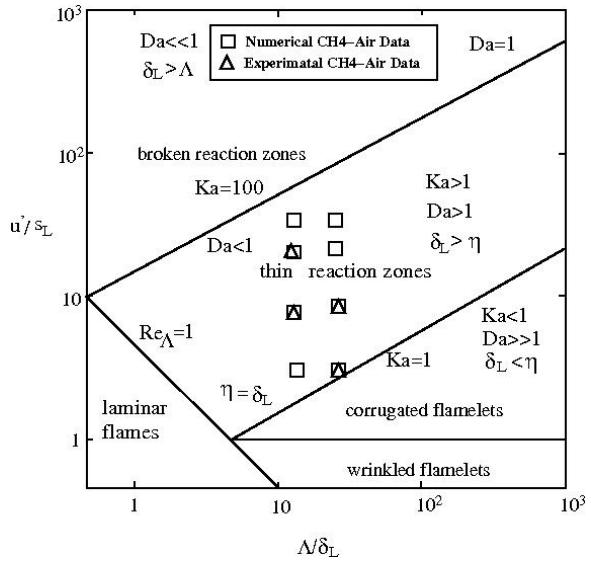

Figure 5.23: Premixed turbulent combustion regime diagram showing the conditions for the eight Bunsen-type flames (cases H–P, 4 experimental and 8 numerical cases) considered herein.

mately 42 cells in the radial direction for this case. The design and mesh spacing for this grid was determined based on the findings of study of the two-dimensional freely propagating flames with AMR described earlier in Section 5.2.3. Subsonic inflow and outflow boundary conditions were applied at the axial inflow and outflow boundaries and subsonic outflow boundary conditions with a fixed pressure were employed at the radial outflow boundaries. The turbulent inflow conditions were again obtained

Flame	ϕ	Λ	λ	η	u'	s_L	δ_L	u'/s_L	Λ/s_L	U
CH4-Air		mm	mm	mm	m/s	m/s	mm			m/s
H	1.0	1.635	0.442	0.05174	1.33	0.403	0.05	3.3	30.46	17.59
I	1.0	1.790	0.460	0.02935	2.92	0.403	0.05	7.25	33.34	15.58
J	1.0	1.790	0.460	0.02935	5.79	0.403	0.05	14.38	33.34	15.58
K	1.0	1.790	0.460	0.02935	9.71	0.403	0.05	24.1	33.34	15.58
L	0.7	1.635	0.442	0.05174	0.66	0.201	0.11	3.3	15.2	17.59
M	0.7	1.635	0.442	0.05174	1.33	0.201	0.11	6.55	15.2	17.59
N	0.7	1.790	0.460	0.02935	2.92	0.201	0.11	14.38	16.64	15.58
P	0.6	1.790	0.460	0.02935	2.92	0.121	0.18	24.1	9.88	15.58

Table 5.3: Summary of turbulence scales and flame conditions for the eight Bunsen-type flames (cases H–P) considered herein.

by using the procedure of Rogallo [155]. The mean inflow velocity was prescribed to match the measured values from the experimental cases (i.e., 15.58 m/s for all stoichiometric cases and 17.79 m/s for all lean cases) and the turbulence fluctuations were superimposed with different fluctuation velocities, u', cooresponding to the relative turbulence intensities, $u'/s_{\rm L}$, Table 5.3. Although not shown, for the selected mesh the percentages of the unresolved turbulence were 5% for case H, 5.8% for case I, 6.6% for case J, 6.3% for case K, 4.3% for case L, 5.2% for case M, 6.3% for case N, and 6.3% for case P. The LES of the eight premixed flames were carried out for a time period $t = 9.0$ ms after initialization, at which time quasi-steady flame structures were established. Support for the quasi-steady nature of the LES solutions is given below.

All of the three-dimensional LES computations of the Bunsen-type premixed flames were carried out using the SciNet facilities. The simulation of each case was performed using 13 IBM Power 6-575 nodes, each with 32 cores for a total of 416 cores. The estimated total CPU time was about 50,000 hours and total wall clock time was about 150 hours for each simulation.

5.4.2 Qualitative Features of LES Flame Structures

To begin this assessment of the FSD-LES modelling, qualitative features of six of the flames are first examined. Results for three stoichiometric cases (cases H, I, and J) and three lean methane-air flames (cases L, M, and N) are considered for this purpose. Three-dimensional views of the predicted instantaneous flame surfaces, identified by the $c = 0.5$ iso-surfaces of the progress variable, are displayed in Figure 5.24 corresponding to time $t = 9$ ms after the initiation of the simulation, all of which by this time have achieved a quasi-steady flame structure. In general, the six simulated flames exhibit highly wrinkled surfaces and the scale of wrinkling becomes larger near the tips of the flames. It can also be observed that the flame wrinkling increases with turbulence intensity. As expected the heights of the flames are seen to be related to the overall burning rates. The flame heights can be seen to decrease with increasing turbulence intensity as expected and, in general, the stoichiometric

flames are shorter for similar turbulence intensities than their lean counterparts. Note that the laminar flame speed for stoichiometric flames is a factor of two larger than the flame speed for the lean flames, and thus the absolute burning rates of the stoichiometric flames are expected to be higher than those of the lean flames. Further quantitative comparisons of predicted average flame heights to measurements based on analysis of the mean progress variable, $\bar{c}$, are discussed in the subsections to follow.

More details of the LES flame structures can be seen in Figures 5.25–5.27, which show the predicted contours of progress variable, FSD, and temperature fields, respectively, for a vertical y-z plane through the burner at time $t = 9$ ms. In particular, it is evident from these figures that there are increases in the maximum values of FSD with relative turbulence intensity increase. The flames are anchored and prevented from undergoing strong wrinkling by the burner base; however, further downstream above the burner exit, the flames become more strongly wrinkled and pockets of unburned reactants can be clearly identified. Note that the background or product temperatures are lower for the lean cases as should be expected.

Unlike the freely propagating flames considered earlier, it is somewhat difficult to compare here the level of resolved wrinkling for the three stoichiometric cases (case H, I, and J), the three lean methane-air flames (case L, M, and N). The LES results for three-dimensional freely propagating methane-air flames described in the previous sections of this chapter suggest that lean methane-air flames exhibit somewhat more wrinkling and have more diffused fronts. Moreover, the previous work of Kaminski *et al.* [159] suggests that there may be some dependence of flame wrinkling on equivalence ratio. However, for the Bunsen flames shown in Figures 5.24–5.27, it would seem that the lean methane-air flame fronts undergo somewhat less wrinkling by the turbulence than the stoichiometric flames. This feature will be examined further below when predicted overall turbulent burning rates are considered.

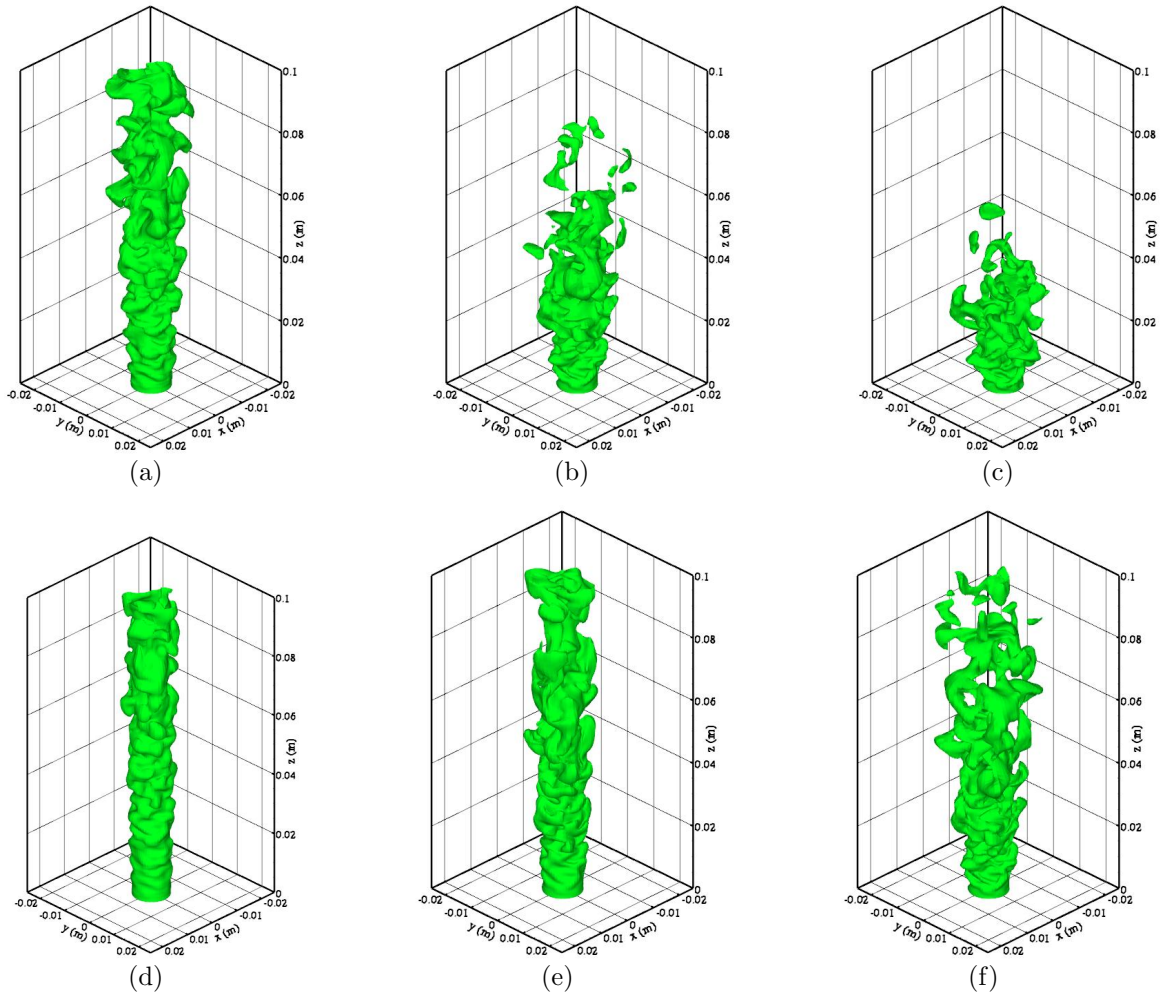

Figure 5.24: Predicted iso-surfaces of the progress variable at $c=0.5$ for stoichiometric cases with turbulence intensities at $t=9$ ms: (a) $u'/s_{\mathrm{L}}=3.3$ (case H), (b) $u'/s_{\mathrm{L}}=7.25$ (case I), (c) $u'/s_{\mathrm{L}}=14.38$ (case J), and lean cases with turbulence intensities: (d) $u'/s_{\mathrm{L}}=3.3$ (case L), (e) $u'/s_{\mathrm{L}}=6.55$ (case M), (f) $u'/s_{\mathrm{L}}=14.38$ (case N).

5.4.3 Analysis and Reduction of LES and Experimental Image Data

In order to directly compare the present LES-FSD simulations to the experimental measurements of Yuen and Gülder [4, 5] for the two stoichiometric and two lean methane-air premixed flames (cases H, I, M, and N, respectively), the temperature fields from both the planar experimental images and two-dimensional FSD-LES cal-

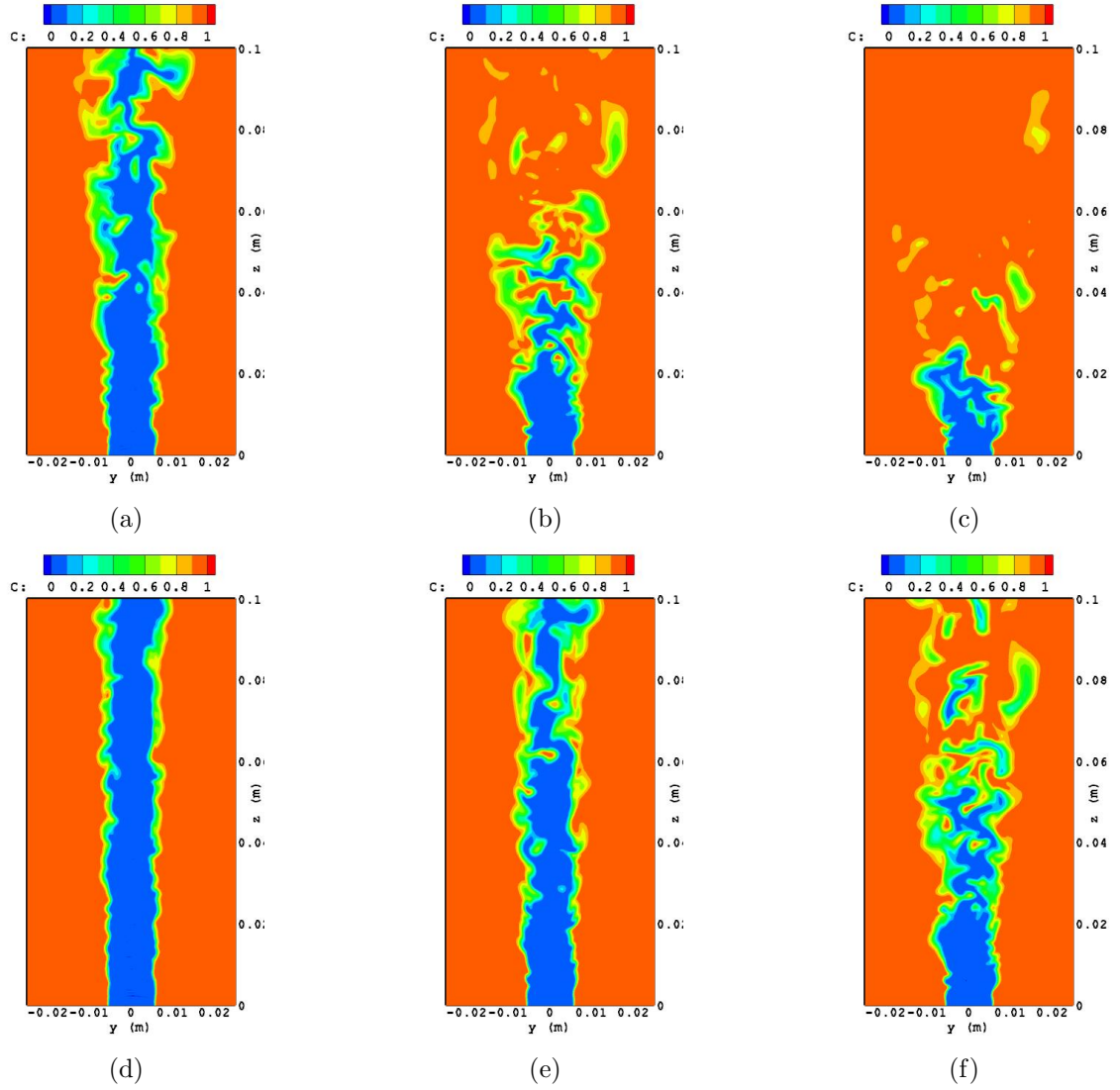

Figure 5.25: Predicted contours of the progress variable at y-z plane for stoichiometric cases with turbulence intensities at $t = 9$ ms: (a) $u'/s_L = 3.3$ (case H), (b) $u'/s_L = 7.25$ (case I), (c) $u'/s_L = 14.38$ (case J), and lean cases with turbulence intensities: (d) $u'/s_L = 3.3$ (case L), (e) $u'/s_L = 6.55$ (case M), (f) $u'/s_L = 14.38$ (case N).

culation solution cross sections were processed with the same algorithms in identical fashion so as to extract information concerning the flame heights, surface area, and curvature statistics. A detailed description of the data analyses and reduction techniques used can be found in the recent Ph. D. thesis of Yuen [4]. For the purposes of completeness, these data analyses are also briefly summarized in what follows.

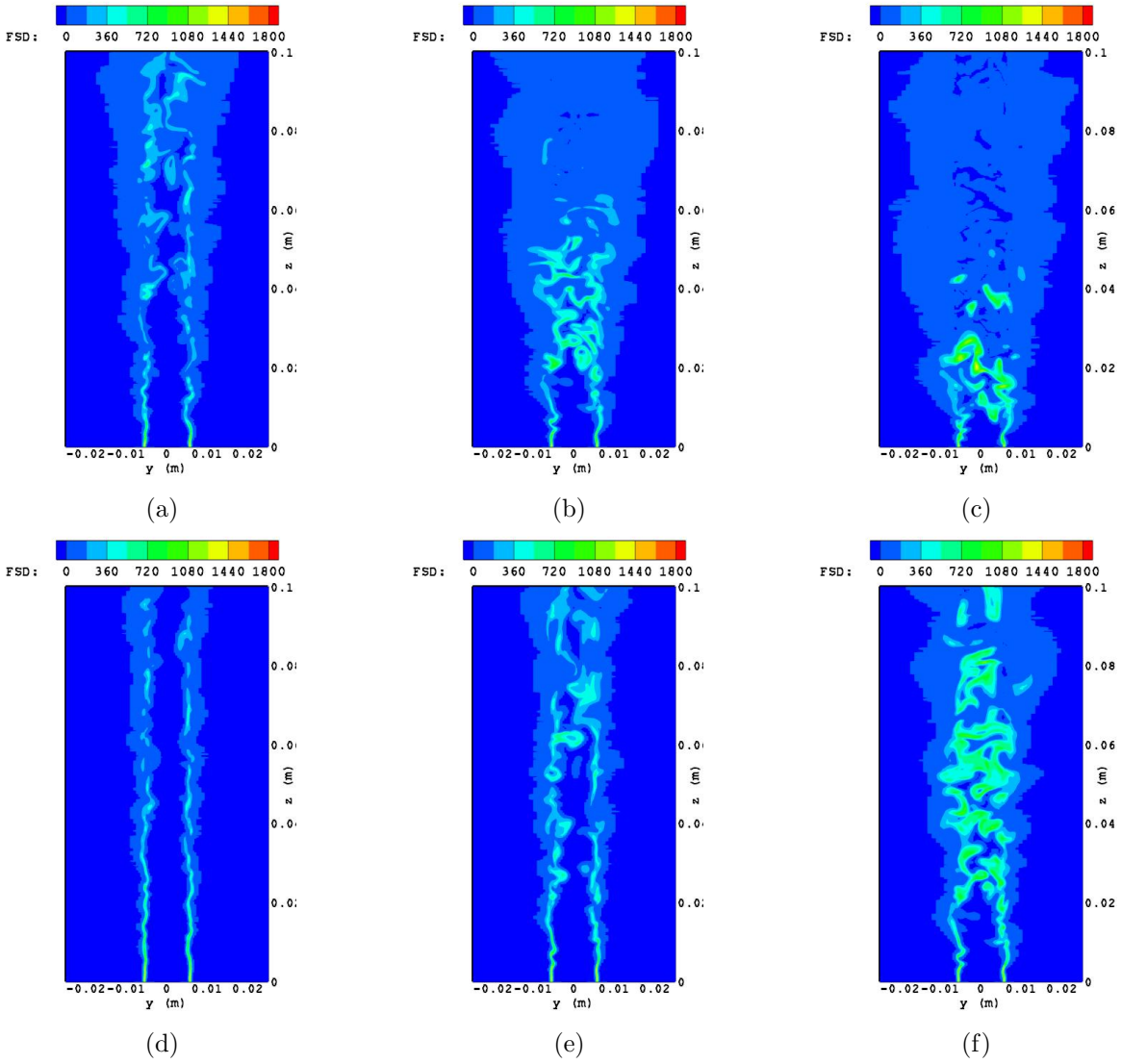

Figure 5.26: Predicted contours of the FSD at y-z plane for stoichiometric cases with turbulence intensities at $t = 9$ ms: (a) $u'/s_{\mathrm{L}} = 3.3$ (case H), (b) $u'/s_{\mathrm{L}} = 7.25$ (case I), (c) $u'/s_{\mathrm{L}} = 14.38$ (case J), and lean cases with turbulence intensities: (d) $u'/s_{\mathrm{L}} = 3.3$ (case L), (e) $u'/s_{\mathrm{L}} = 6.55$ (case M), (f) $u'/s_{\mathrm{L}} = 14.38$ (case N).

The temperature field analysis takes the two-dimensional planar distributions of the temperature from Rayleigh scattering images or LES results and converts the values of the temperature to a progress variable, c, which is defined in terms of the reduced temperature as follows:

$$c = \frac{T - T_{\mathrm{u}}}{T_{\mathrm{b}} - T_{\mathrm{u}}}, \tag{5.3}$$

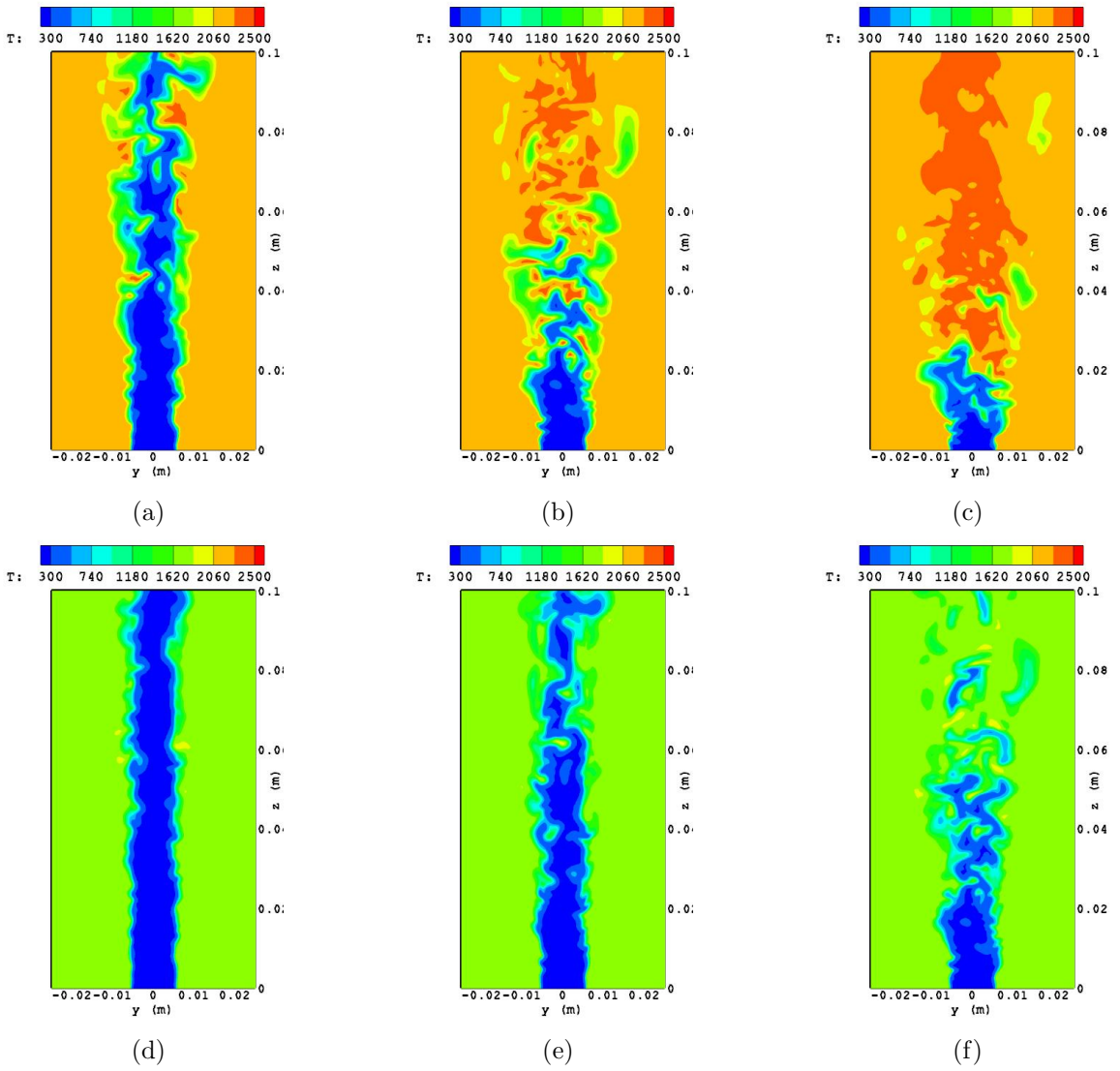

Figure 5.27: Predicted contours of the temperature at y-z plane for stoichiometric cases with turbulence intensities at $t = 9$ ms: (a) $u'/s_{\mathrm{L}} = 3.3$ (case H), (b) $u'/s_{\mathrm{L}} = 7.25$ (case I), (c) $u'/s_{\mathrm{L}} = 14.38$ (case J), and lean cases with turbulence intensities: (d) $u'/s_{\mathrm{L}} = 3.3$ (case L), (e) $u'/s_{\mathrm{L}} = 6.55$ (case M), (f) $u'/s_{\mathrm{L}} = 14.38$ (case N).

where T is the instantaneous temperature at each pixel of the experimental image or LES computational cell, T_{b} is the burnt temperature and T_{u} is the unburnt gas temperature. Values taken for T_{b} and T_{u} were the peak values of the probability density functions (PDFs) of the temperature distribution for each two-dimensional image. In what follows, the progress variable is based on the reduced temperature

field, unless otherwise specified.

Gradients of the progress variable, $\vec{\nabla}c$, are estimated for each image or distribution of c by using:

$$\vec{\nabla}c(x,y) = \sqrt{\left[\frac{c(x+\Delta x) - c(x-\Delta x)}{2\Delta x}\right]^2 + \left[\frac{c(y+\Delta y) - c(y-\Delta y)}{2\Delta y}\right]^2}, \qquad (5.4)$$

where x and y are the coordinates of the pixels or cells and Δx and Δy are the distance between the pixels or cells. An interpolation procedure is also then used to locate the position of the flame front for different values of c (e.g., the $c=0.5$ contour corresponds to the middle of the flame). The corresponding values of $\vec{\nabla}c$ along the flame front are also evaluated.

Having defined the progress variable for the image, the average value of the progress variable, $\bar{c}$, based on all of the flame images can be obtained. In the case of the experimental results, 300 images of the progress variable distribution within the flame are averaged to determine the distributions of $\bar{c}$. For each LES simulation, the two-dimensional cross-sectional slices were extracted from 19 instantaneous snapshots of the numerical solution separated by 0.25 ms taken from the quasi-steady phase of the flame simulations. The averaging procedure was applied to these numerical images to determine the corresponding $\bar{c}$-maps. The experimental and numerical $\bar{c}$-maps can then be used to define average flame height and the extent of the flame brush for each case.

For the analysis of the flame surface area or FSD, the individual distributions of c and $\vec{\nabla}c$, as well as the cumulative distribution for $\bar{c}$, are used. Two different techniques for the analysis of the FSD data are considered. One of approach uses the gradient of the progress variable along the flame front to estimate values for the flame surface density. The other method uses the ratio of the flame front length, $L(\bar{c})$, to the flame zone area, $A(\bar{c})$. In the gradient of c method, components of $\vec{\nabla}c$ in x and y directions are extracted along the flame from (paths of constant c) for $c=0.1$ to $c=0.9$. The distribution of the instantaneous local values of the FSD, Σ, along the flame front is then calculated using the following definition:

$$\Sigma = |\vec{\nabla}c|\delta(c-c^*), \qquad (5.5)$$

where $\delta(c - c^*)$ is the Kronecker delta function and $c = c^*$ defines the instantaneous flame front location. The instantaneous flame fronts are then averaged to obtain PDFs of FSD and values of the FSD as a function of the progress variable. Note that the resolution of the two-dimensional numerical images is much less than that of the experimental images. In the current simulation results, there are about 50,000 cells along the flame fronts, whereas, the experimental images have about 2,000,000 pixels along each front.

The second method for estimating the FSD from the two-dimensional planar distributions of the progress variable is due to Shepherd [168] and follows from direct measures of the flame front length, L, and the flame zone area, A, as functions of the mean progress variable, $(\bar{c})$. Although the true definition of FSD is the flame surface area per unit volume, a two-dimensional estimate based on the ratio $L(\bar{c})/A(\bar{c})$ has been shown to provide reasonable estimates of the FSD. The flame zone area, $A(\bar{c})$, is determined from maps of $\bar{c}$. Values for $A(\bar{c})$ values are calculated from the distribution of $\bar{c}$ and the known area of each image pixel or cell. As for flame front length, $L(\bar{c})$, each instantaneous flame front edge defined by $c = 0.5$ is divided into equal segments of one pixel or one lengths. The flame front edge is then superimposed onto the core $\bar{c}$-map and each segment of the flame front segment is assigned a value of $\bar{c}$. From this, $L(\bar{c})$ is found in a similar manner to $A(\bar{c})$ and then the ratio $L(\bar{c})/A(\bar{c})$ is calculated to determines values for $\Sigma(\bar{c})$.

Finally, the local flame curvature, h, at each pixel or cell along the flame front can be calculated using the expression

$$h = \frac{\dot{x}\ddot{y} - \dot{y}\ddot{x}}{(\dot{x}^2 + \dot{y}^2)^{3/2}}, \tag{5.6}$$

where $\dot{x} = \mathrm{d}x/\mathrm{d}s$ and $\ddot{x} = \mathrm{d}^2x/\mathrm{d}^2s$ are the first and second derivatives with respect to s which is a path length coordinate along the flame front measured from a fixed origin on the flame front. For each experimental or numerical image, instantaneous values for the local flame curvature are calculated along the flame front defined by $c = 0.5$ and these values are then grouped to form a probability density function of the curvature. This procedure is similar to the method described by Pavé [169].

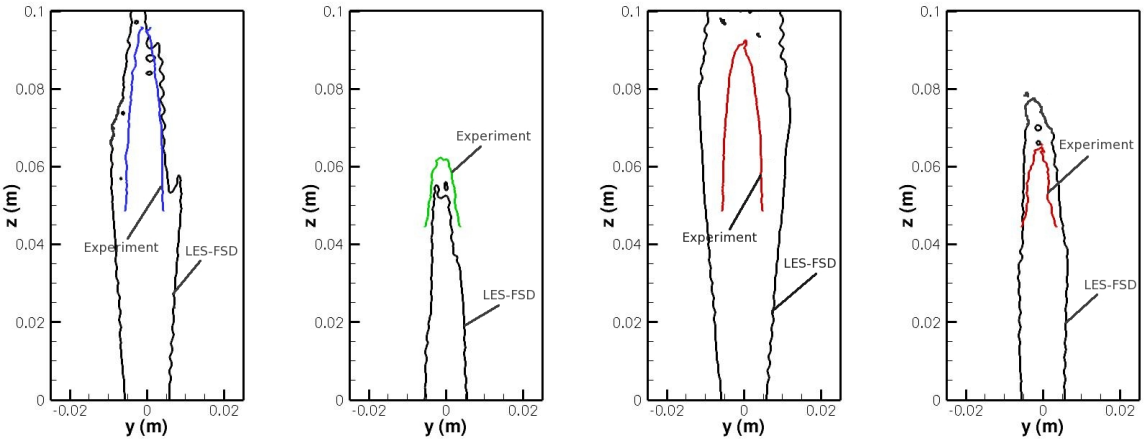

Figure 5.28: Comparison of the measurement and LES predictions of the location or map of the $\bar{c} = 0.5$ contour line in the y-z plane for the stoichiometric methane-air Bunsen flames with turbulence intensities: (a) $u'/s_L = 3.3$ (case H) and (b) $u'/s_L = 7.25$ (case I); and lean methane-air Bunsen flames with turbulence intensities: (c) $u'/s_L = 6.55$ (case M) and (d) $u'/s_L = 14.38$ (case N). Experimental measurements taken from Yuen and Gülder [4, 5].

5.4.4 Quantitative Comparisons of LES and Experimentally Estimated Values of Flame Height

Figure 5.28 shows a comparison of the experimental measurements and LES solution of the location or map of the $\bar{c} = 0.5$ contour line in the y-z plane for the stoichiometric Bunsen flames with turbulence intensities $u'/s_L = 3.3$ (case H, Figure 5.28(a)) and $u'/s_L = 7.25$ (case I, Figure 5.28(b)) and lean Bunsen flames with turbulence intensities $u'/s_L = 6.55$ (case M, Figure 5.28(c)) and $u'/s_L = 14.38$ (case N, Figure 5.28(d)). The measured $\bar{c} = 0.5$ contour lines were obtained from the Rayleigh scattering images of Yuen and Gülder [4, 5] and the LES solution results were obtained using the LES-FSD computational framework developed as part of this thesis. It should be pointed out that, due to reflections from the burner rim, the Rayleigh scattering images could not be obtained below a height of 40 mm above the burner rim and so the experimental $\bar{c}$-maps are cut off below this height.

It is apparent from the results of Figure 5.28 that the FSD subfilter-scale model

yields flame heights that agree very well with the experimental values in most cases. The experimental flame heights for the stoichiometric flames (cases H and I) are 9.5 cm and 6.5 cm, respectively, and the present LES-FSD modelling predicts flame heights of about 10 cm and 6 cm for these two cases. For the lean flame with $u'/s_L = 14.38$ (case N), the FSD model slightly over predicts the flame height as compared with the experimental value (8 cm is predicted by the LES-FSD modelling compared to the measure value of about 7 cm). It is only for the lean flame with $u'/s_L = 6.55$ (case M) that the quantitative agreement between the numerical predictions and experiment is not as strong. The experimental flame height in this case is about 9.5 cm and the LES-FSD values is clearly well in excess of 10 cm.

5.4.5 Quantitative Comparisons of LES and Experimentally Measured Values of Flame Surface Density

Figure 5.29 depicts comparisons of the predicted and measured histograms representing the PDFs of the FSD through flame as determined using the gradient of c method described above for stoichiometric and lean premixed methane-air Bunsen flames with turbulence intensities of $u'/s_L = 3.3$ (case H), $u'/s_L = 7.25$ (case I), $u'/s_L = 6.55$ (case M), $u'/s_L = 14.38$ (case N). The experimental and numerical PDFs of the FSD are clearly in good agreement for both the stoichiometric and lean cases. The peak values for the experimental and numerical PDFs occur at similar values for the FSD and the general trends and behaviour of the experimental and numerical PDFs are similar. As further evidence of the good agreement between predicted flame area and experiment, Figure 5.30 provides comparisons of the predicted and measured variation of the FSD as a function of progress variable, c, through the same four flames as determined using the gradient of c method. The figure clearly demonstrates similar qualitative and quantitative agreement between the experimental and numerical results. In all the flame surface area profiles, the maximum FSD value is found to be near $c = 0.5$.

Additional comparisons of the predicted and measured variation of the FSD, this time as a function of the mean progress variable, $\bar{c}$, as computed using the $L(\bar{c})/A(\bar{c})$

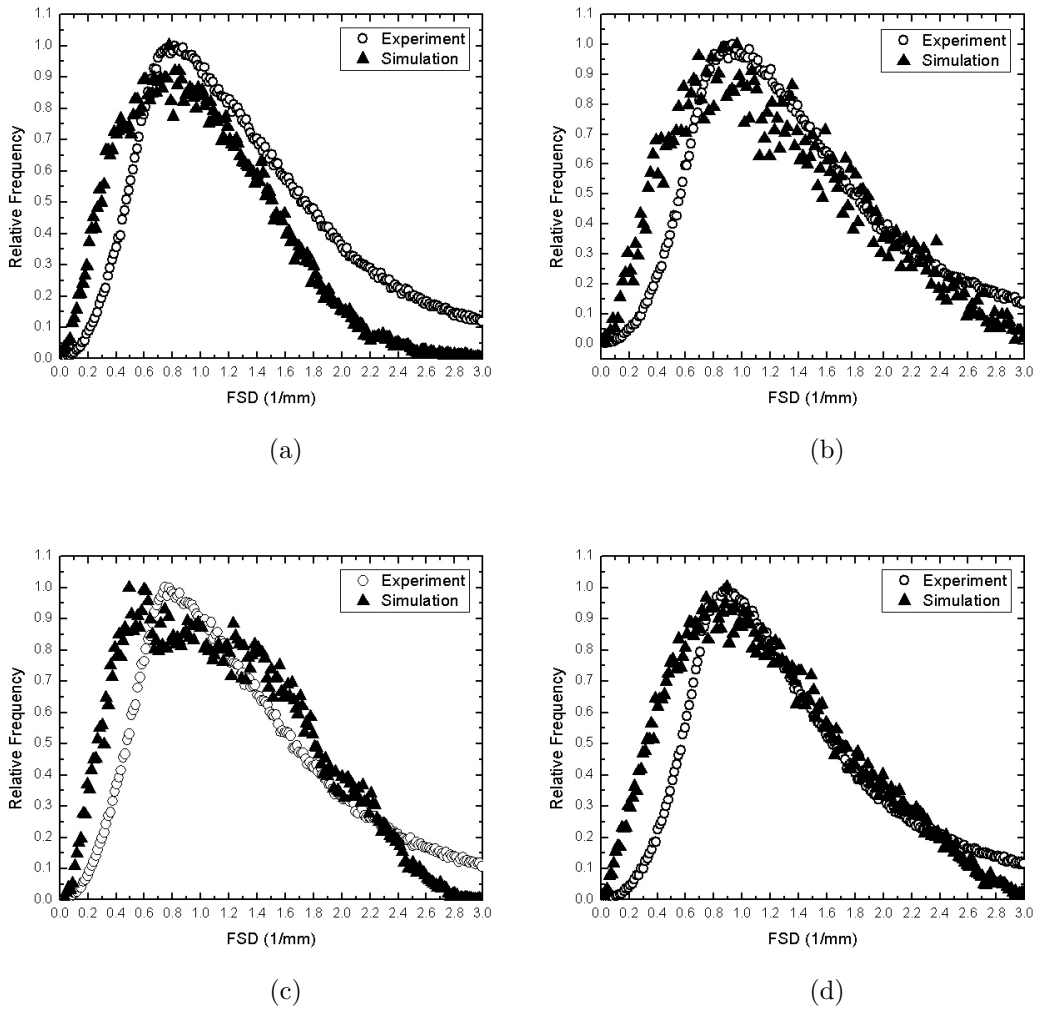

Figure 5.29: Comparisons of the predicted and measured histograms representing the probability density functions (PDFs) of the FSD through flame as determined using the gradient of c method for stoichiometric and lean premixed methane-air Bunsen flames with turbulence intensities: (a) $u'/s_{\mathrm{L}} = 3.3$ (case H), (b) $u'/s_{\mathrm{L}} = 7.25$ (case I), (c) $u'/s_{\mathrm{L}} = 6.55$ (case M), (d) $u'/s_{\mathrm{L}} = 14.38$ (case N). Experimental measurements taken from Yuen and Gülder [4, 5].

method are shown in Figure 5.31. While the agreement between the LES results and measured flame surface as determined by this alternative approach is not as good as was obtained for the reduction technique based on the gradient of c, the agreement is still quite reasonable. Moreover, it would seem that the FSD subfilter-scale model

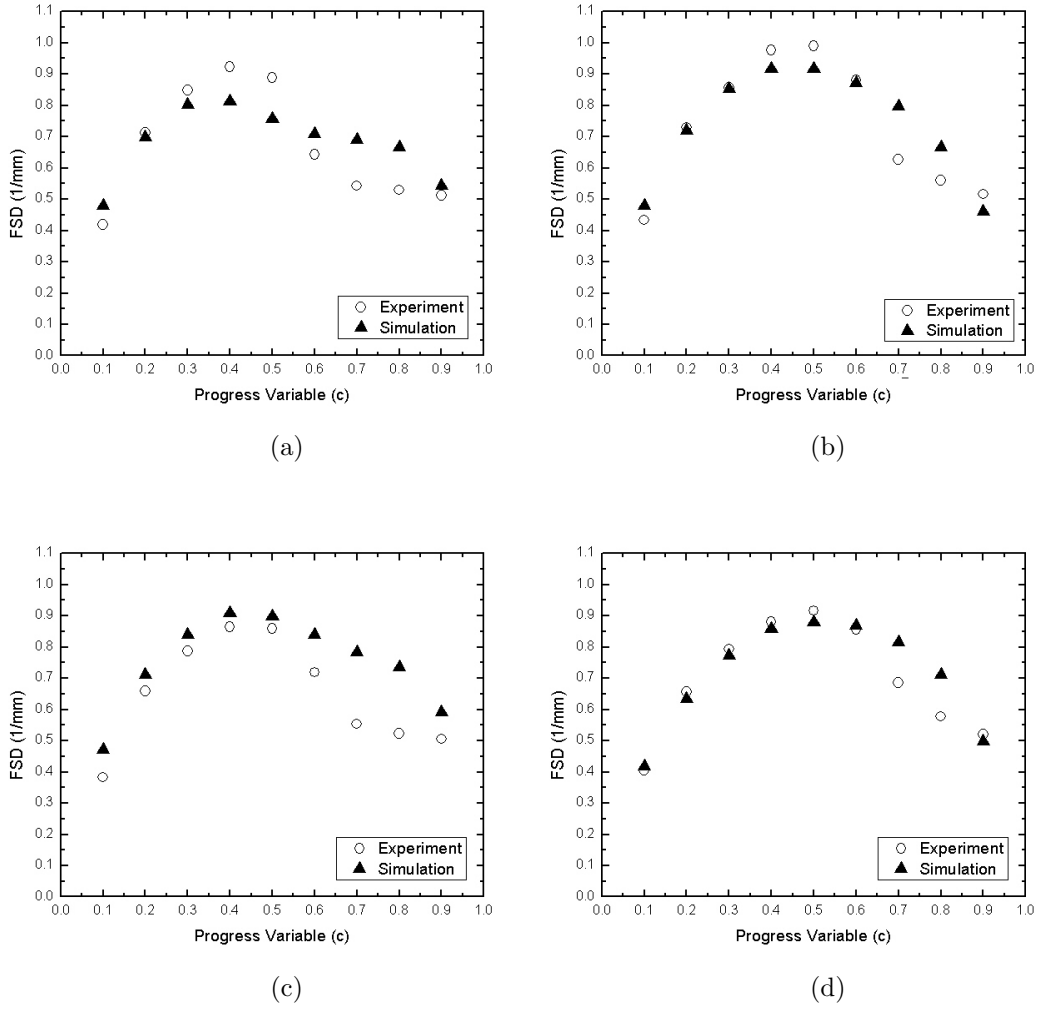

Figure 5.30: Comparisons of the predicted and measured variation of the FSD, Σ, as a function of progress variable, c, as determined using the gradient of c method for stoichiometric and lean premixed methane-air Bunsen flames with turbulence intensities: (a) $u'/s_{\mathrm{L}} = 3.3$ (case H), (b) $u'/s_{\mathrm{L}} = 7.25$ (case I), (c) $u'/s_{\mathrm{L}} = 6.55$ (case M), (d) $u'/s_{\mathrm{L}} = 14.38$ (case N). Experimental measurements taken from Yuen and Gülder [4, 5].

is well suited to describing the evolution and dynamics of the flame front and surface area, yielding surprisingly good predictions of the FSD distributions for the premixed Bunsen flames of interest here.

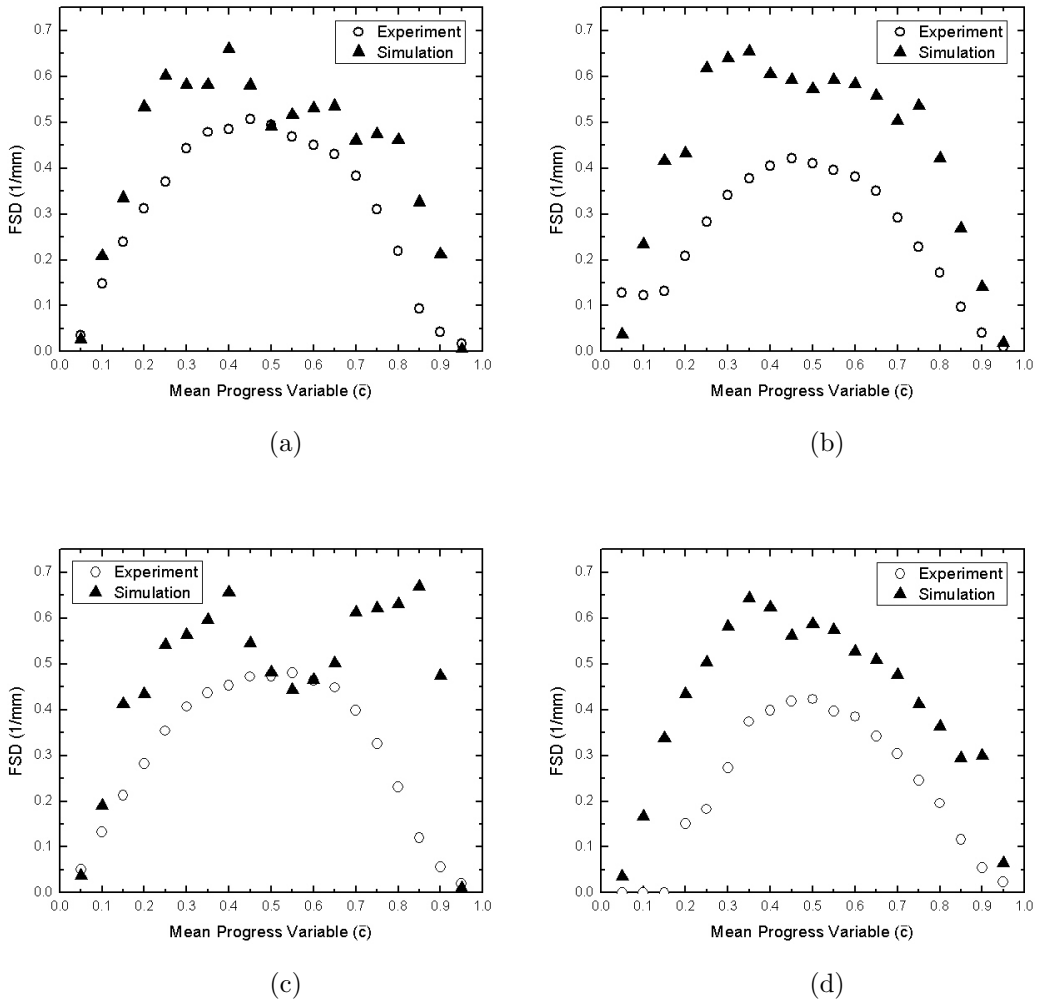

Figure 5.31: Comparisons of the predicted and measured variation of the FSD, Σ, as a function of mean progress variable, $\bar{c}$, as determined using the $L(\bar{c})/A(\bar{c})$ method stoichiometric and lean premixed methane-air Bunsen flames with turbulence intensities: (a) $u'/s_{\mathrm{L}} = 3.3$ (case H), (b) $u'/s_{\mathrm{L}} = 7.25$ (case I), (c) $u'/s_{\mathrm{L}} = 6.55$ (case M), (d) $u'/s_{\mathrm{L}} = 14.38$ (case N). Experimental measurements taken from Yuen and Gülder [4, 5].

5.4.6 Quantitative Comparisons of LES and Experimentally Measured Values of Flame Curvature

Comparisons of the predicted and measured histograms representing the PDFs of the flame front curvature through the flame for the two stoichiometric flames (cases H

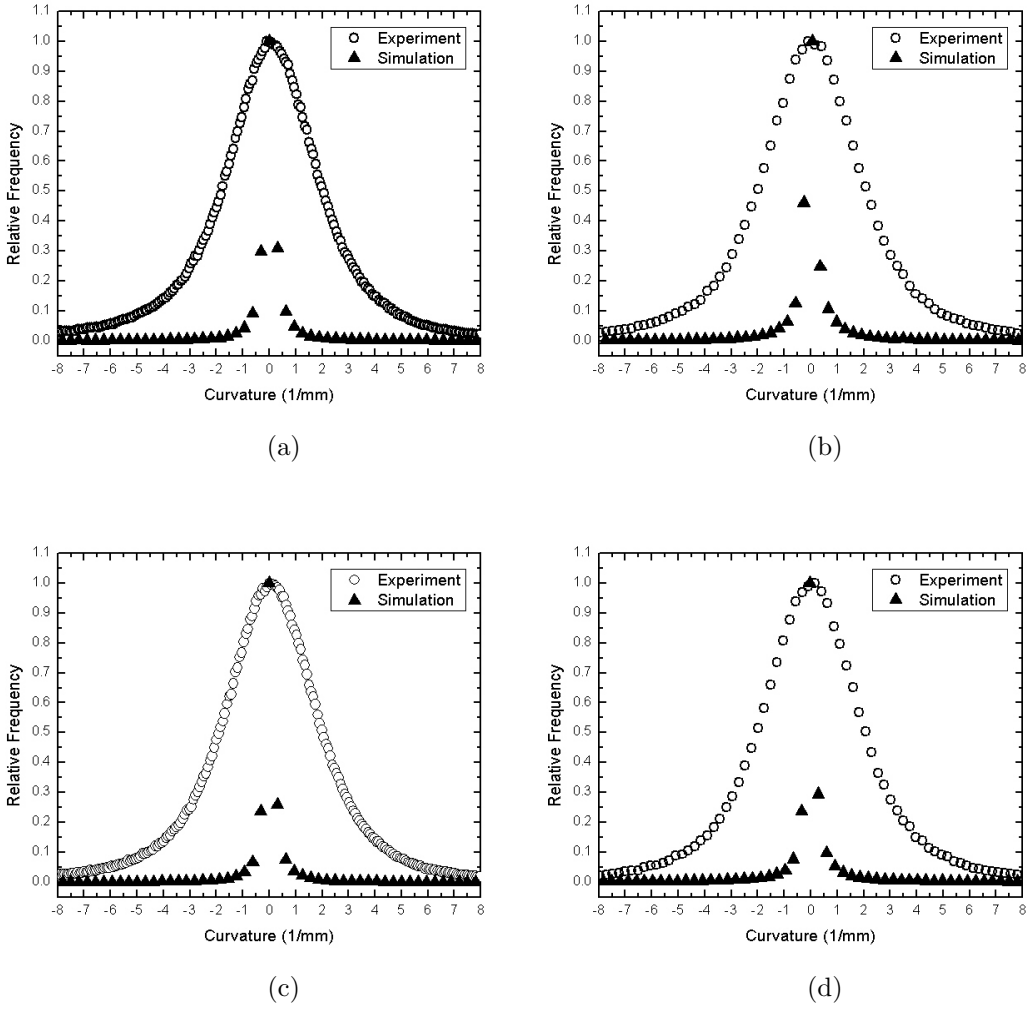

Figure 5.32: Comparisons of the predicted and measured histograms representing the probability density functions (PDFs) of the flame curvature through flame for stoichiometric and lean premixed methane-air Bunsen flames with turbulence intensities: (a) $u'/s_{\mathrm{L}} = 3.3$ (case H), (b) $u'/s_{\mathrm{L}} = 7.25$ (case I), (c) $u'/s_{\mathrm{L}} = 6.55$ (case M), (d) $u'/s_{\mathrm{L}} = 14.38$ (case N). Experimental measurements taken from Yuen and Gülder [4, 5].

and I) and the two lean premixed flames (cases M and N) are displayed in Figure 5.32. It is quite apparent from the results that the experimental PDFs of flame curvature are both symmetric and Gaussian-like distributions for all four turbulent intensities. Similar trends for flame curvature were found in other previous experimental studies

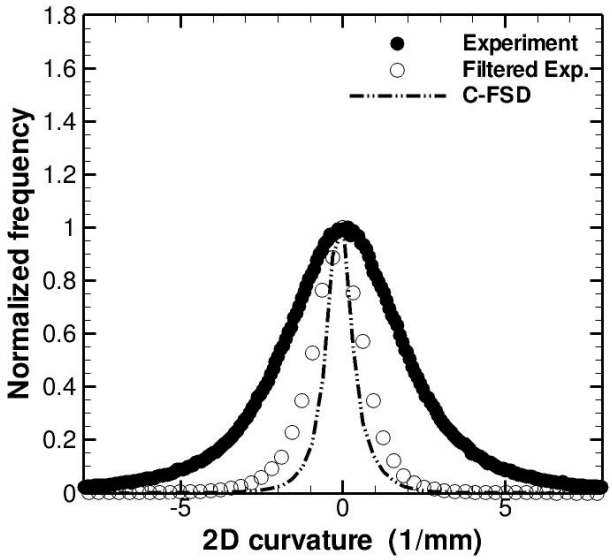

Figure 5.33: Comparison of the predicted and measured histograms representing the probability density functions (PDFs) of the flame curvature through flame for lean premixed methane-air Bunsen flame with turbulence intensity $u'/s_{\mathrm{L}} = 14.38$ (case N). Original and filtered experimental results are both shown with latter based on top-hat spatial filtering of Rayleigh scattering images of Yuen and Gülder [4, 5].

of premixed turbulent flames by Shepherd [161]. While the numerical PDFs of flame curvature also appear to be symmetric Gaussian-like distributions, there are clear differences between the LES and measured distributions. In particular, all of the LES solutions exhibit narrower PDFs as compared to the experimental ones with the range of curvatures present in numerical solution being significantly reduced compared to that detected by the experimental measurements (e.g., curvatures between ± 1 mm^{-1} are prevalent in the LES results whereas the curvature typically falls in the range $\pm$5-6 mm^{-1} for the four experimental flames). Remembering that the resolution of the Rayleigh scattering imaging used in the experiments is much higher than that of the LES (refer to Subsection 5.4.3 above), it is argued that the LES filtering effectively removes all of the small-scale wrinkled structures, having high curvature, from the numerical solutions. As LES provides solutions for filtered flow variables, it would seem more appropriate to compare the LES results with filtered experimental data.

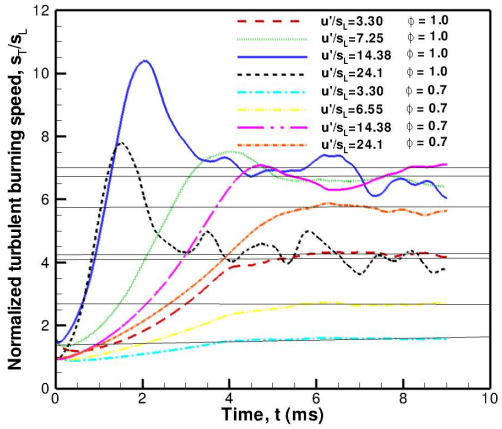

(a) Time histories of predicted turbulent burning rates as determined from the LES-FSD simulations for $0 \leq t \leq 9$ ms for lean and stoichiometric premixed Bunsen flames, cases H–P.

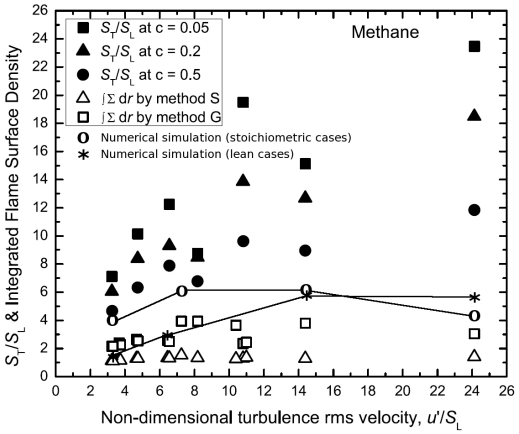

(b) Comparison of predicted and measured values of the normalized turbulent burning rates as a function of turbulence intensity for lean and stoichiometric premixed Bunsen flames, cases H–P. The experimental results are due to Yuen and Gülder [4, 5] and include estimated burning rates for three different values of the progress variable, c, and estimates of the integrated flame area.

Figure 5.34: Time histories of predicted turbulent burning rates as determined from LES-FSD simulations and comparisons of predicted and measured values of the turbulent burning rates as a function of turbulence intensity for lean and stoichiometric premixed methane-air Bunsen flames, cases H–P.

Support for the preceding argument is provided by the results of Figure 5.33 which shows a comparison of the curvature PDFs of the original experimental data, filtered experimental data, LES solution for the lean premixed methane-air Bunsen flame with $u'/s_L = 14.38$ (case N). The experimental temperature images were filtered with a top-hat filter having a characteristic size of two times the average cell size of the LES computational grid. It would seem that there is quite good agreement between the filtered experimental distribution of flame curvature and numerical results for this case.

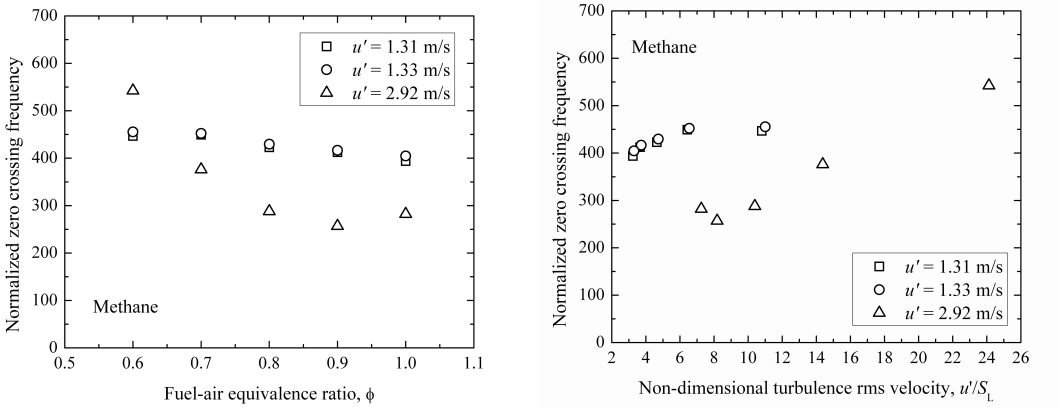

(a) Normalized zero crossing (curvature) frequency (averaged zero crossings per flame) for instantaneous surfaces of constant progress variable as a function of equivalence ratio.

(b) Normalized zero crossing (curvature) frequency (averaged zero crossings per flame) for instantaneous surfaces of constant progress variable as a function of turbulence intensity.

Figure 5.35: Experimental measurements of normalized zero crossing (curvature) frequency, a measure of the degree of wrinkling of flame surface, for lean and stoichiometric premixed methane-air Bunsen flames due to Yuen and Gülder [4–6].

5.4.7 Quantitative Comparisons of LES and Experimentally Measured Values of Turbulent Burning Rate

The predicted turbulent burning rates may be calculated from the LES-FSD results by using the integrated FSD as follows:

$$\frac{s_{\mathrm{T}}}{s_{\mathrm{L}}} \propto \int_V \bar{\rho}\tilde{\Sigma}\mathrm{d}V. \tag{5.7}$$

where the integration is performed over the entire computational domain. Figure 5.34 shows the predicted normalized turbulent burning rates for the four stoichiometric (cases H, I, J, and K) and four lean cases (cases L, M, N, and P) obtained using Eq. (5.7). In particular, Figure 5.34(a) depicts the complete time histories of the predicted turbulent burning rates and Figure 5.34(b) shows a comparison of the predicted quasi-steady normalized turbulent burning rates for the eight flames to estimated values of the burning rates and integrated flame surface area obtained by Yuen and Gülder [4, 5] from analyses of the measured flame structure. Note that, as discussed in Chapter 2, according to the flamelet assumption of Damköhler for

premixed flames it is expected that the turbulent burning rates and integrated flame areas should be strongly correlated with each other, with both quantities increasing with increasing turbulence intensity.

The first observation that can be made from Figure 5.34(a) is that, sometime between 5 ms and 6 ms after initialization of the flame in all eight of the LES calculations, a relatively stable and constant value of turbulent burning rate is achieved. This is indicative of the fact that the transient features associated with the initialization of the simulations are no longer present and a quasi-steady flame has been established for the last 3-4 ms of the computations. It is the average of these "quasi-steady" values for the burning rate that are reported along with the experimental results in Figure 5.34(b). Note that the somewhat unphysical flame solution content associated with the computation initialization is transported out of the domain during the first 5-6 ms of the simulation.

It is also quite clear from Figure 5.34, that while showing a gradual increase for low relative turbulence intensities, the LES-FSD predictions of the burning rates do not continue to increase with increasing turbulence intensity and a maximum value appears to be achieved for $u'/s_{\mathrm{L}} > 6$-8, for both lean and stoichiometric flames. The plateaus in the predicted burning rates are directly related, through the flamelet approximation, to a lack of an increase in the predicted flame surface area by the FSD model. It seems that flame area does not continue to increase with increasing turbulence intensity (i.e., there appears to be an upper limit to the degree of wrinkling of the flame front that can be induced by the turbulence). While the experimental measurements of burning rate continue to increase with turbulence intensity, the LES predictions of burning rate and flame area are strongly supported by and agree with both qualitatively and quantitatively with the integrated values of the measured FSD. The latter also appear to reach a maximum for $u'/s_{\mathrm{L}} > 6$-8 and thereafter remain relatively insensitive to turbulence intensity. From this and the previous comparisons of the LES and experimental results, it would seem that the modelled transport equation for the FSD can in fact quite accurately represent the degree of wrinkling of the flame surface and increases in flame surface area produced by the turbulent field. Nevertheless, it would appear that it is not entirely correct to infer

a direct relationship between turbulent burning rate and flame area. The results of Figure 5.34 cast some doubt on the flamelet concept, at least for higher turbulence intensities (i.e., $u'/s_L > 6$-8). Note that while the flamelet concept originally due to Damköhler is formally only correct in the wrinkled and corrugated flamelet regimes, in which the laminar flame thickness, δ_L, is smaller than the smaller turbulent scales (i.e., the Kolmogorov scale), it has been speculated that the flamelet approach remains valid throughout the thin reaction zones regime. For the latter, the smallest scales of the turbulence are generally smaller than the flame front thickness but larger than the width of the reaction or heat-release zone and therefore leave the latter intact. The LES and experimental results of Figure 5.34 strongly suggest that the range of validity of the flamelet concept does not in fact to extend very far into the thin reaction zones regime.

A final observation that can be made from Figure 5.34(a) pertains to the influence of stoichiometry on flame wrinkling and burning rates. For LES-FSD predictions of the freely-propagating methane-air flames discussed in the previous section above, it was found that the flame front of the lean flame exhibited a higher degree of wrinkling than the stoichiometric cases and this, in turn, resulted in higher predicted normalized turbulent burning rates. For the premixed methane-air Bunsen flames of Yuen and Gülder, this trend is not quite so clear. For the flames having lower relative turbulence intensities with $u'/s_L = 3.3$ (cases H and L), $u'/s_L = 7.25$ (case I), and $u'/s_L = 6.55$ (case M), the predicted normalized turbulent burning rates provided by the LES for the stoichiometric cases are somewhat higher than those for the lean cases. However, for higher relative turbulence intensity case with $u'/s_L = 24.1$ (cases K and P), lean cases have a higher value for the normalized turbulent burning rate.

Yuen and Gülder [6] have recently performed further analysis of their experimental data for the Bunsen flames. In particular, they re-examined the flame curvature along the flame front and collected statistics on the occurrence of zero curvature points, i.e., the transition points from negative to positive curvatures along the flame. It is argued that the frequency of zero curvature (crossing) points provides the information on the degree of wrinkling of the flame front. Figures 5.35(a) and 5.35(b) summarize the results of the zero curvature statistical analysis for the methane-air flames. The

normalized frequency of zero curvature points as a function of both equivalence ratio and turbulence intensity are shown in the figures. The frequency of occurrences has been normalized by the total number of images in each flame set. The results of Figures 5.35(a) and 5.35(b) suggest that there is a mild dependence of flame wrinkling on stoichiometry for high turbulence intensity and that the lean flames seem to exhibit a greater degree of wrinkling for higher turbulence intensity. Although it is felt that further investigation of this matter is certainly warranted, this interpretation of the results of the curvature analysis would appear to match the findings noted in the LES-FSD results above.

5.4.8 Influence of Mesh Resolution

The LES studies of two-dimensional premixed turbulent flames discussed earlier in Section 5.2.1 of this chapter demonstrated the typical mesh resolution requirements for accurately representing the FSD at the flame front. All of the meshes used in the subsequent three-dimensional calculations above were selected based on this mesh resolution criteria. In an effort to assess further the influence of mesh resolution on the LES results for the three-dimensional Bunsen flames, LES of the premixed Bunsen flame have been carried out using two different grids for the lean case with a turbulence intensity of $u'/s_{\mathrm{L}} = 14.38$ (case N). The first mesh (mesh A) considered in this mesh study, was identical to the mesh used in all of the Bunsen flame simulations described above. Mesh A consisted of 1664 12×12×8 hexahedral blocks and $1,916,928$ computational cells and there were $1,024$ cells in the vertical direction, 48 cells in the azimuthal direction, and approximately 42 cells in the radial direction. The second mesh (mesh B) had the same physical solution domain as that of mesh A; however, now 6400 $8 \times 8 \times 4$ hexahedral solution blocks were used in the discretization of the cylindrical-shaped domain. Mesh B contained $1,638,400$ computational cells with $1,024$ cells in the vertical direction, and just 32 cells in the azimuthal direction, and about 52 cells in the radial direction. Mesh B has a finer mesh spacing in the radial direction than mesh A with $\Delta x_{r_A} = 0.025$ mm $= 0.054\ \lambda = 0.86\ \eta$, and $\Delta x_{r_B} = 0.032$ mm $= 0.07\ \lambda = 1.1\ \eta$, but a coarser mesh spacing in the azimuthal

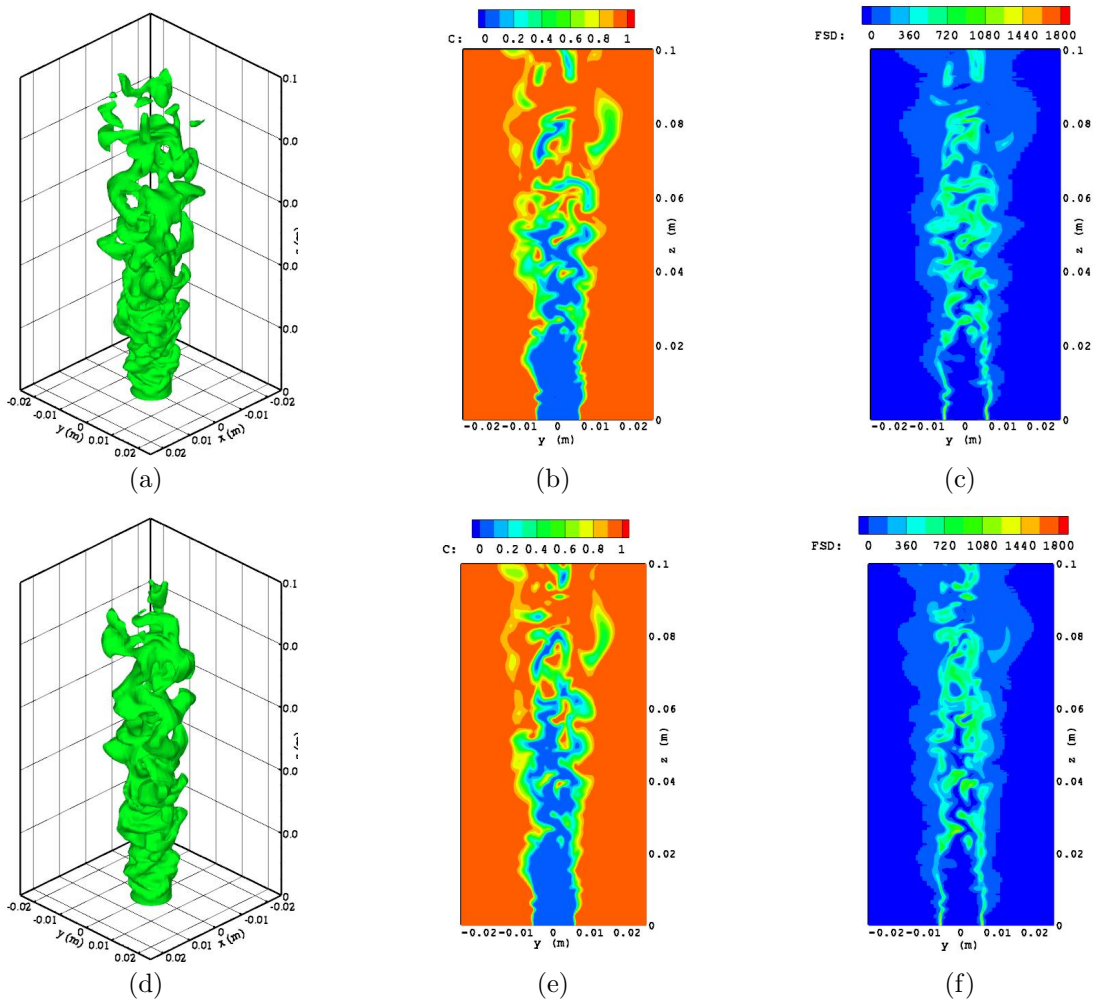

Figure 5.36: Comparison of LES predictions of the iso-surfaces of the progress variable at $c=0.5$, and contours of the progress variable, c, and FSD in the y-z plane for lean premixed methane-air Bunsen flame with turbulence intensity $u'/s_{\mathrm{L}}=14.38$ (case N) obtained using mesh A (1,916,928 cells) and mesh B (1,638,400 cells): (a) mesh A iso-surfaces of the progress variable; (b) mesh A contours of the progress variable; (c) mesh A contours of FSD; (d) mesh B iso-surfaces of the progress variable; (e) mesh B contours of the progress variable; and (f) mesh B contours of FSD.

direction with $\Delta x_{\theta_A} = 0.62$ mm $= 1.3\ \lambda = 21.5\ \eta$, than mesh B, $\Delta x_{\theta_B} = 0.41$ mm $= 0.9\ \lambda = 14.4\ \eta$. Both meshes have the same spacing in the vertical direction with $\Delta x = 0.1$ mm $= 0.002\ \lambda = 0.034\ \eta$.

Figure 5.36 shows a comparison of the LES results for case N on the two different meshes. The predicted iso-surfaces of the progress variable at $c=0.5$ and contours of

both the progress variable, c, and FSD in the y-z plane are shown. Visually, it can be seen that the LES results on the two meshes are qualitatively quite similar. Moreover, if one compares the predicted contours of FSD for these two meshes as shown in Figures 5.36(c) and 5.36(f), the predictions are quantitatively very similar indicating that the FSD seems to have been sufficiently resolved on both computational meshes. While the level resolution of meshes A and B are not dramatically different, the comparisons in Figure 5.36 do provide some further assurance of the reliability and quality of the LES results for the Bunsen flame reported herein.

Chapter 6

Conclusions and Recommendations

6.1 Conclusions

The present study has considered the application of a flame surface density model based on the modelled transport equations from Hawkes and Cant [43] to LES of turbulent premixed flames. A parallel, AMR, finite-volume scheme has been developed for the numerical solutions of the filtered Navier-Stokes equations coupled with modelled equations for the progress variable and FSD. Numerical results have been described for one-, two-, and three-dimensional turbulent premixed flames and the predicted flame structures have been investigated. In particular, comparisons were made between the predicted flame structures and turbulent burning rates as a function of turbulence intensity. For the two-dimensional flames, the LES predictions of the FSD model were compared to results obtained using a thickened flame model and qualitative agreement between the two subfilter-scale models was observed. For the three-dimensional flames, the LES-FSD results were compared to available experimental data for several turbulent premixed methane-air flames. In general, good qualitative and quantitative agreement for flame structures, in terms of predicted flame height, FSD, and flame curvature, was achieved for both stoichiometric and lean cases. The numerical results have demonstrated the capability of the LES methodology for predicting premixed combustion processes.

The key findings and contributions of the thesis can be summarized as follows:

- The current study represents the first application of the FSD model, based on a full transport equation model for the FSD, to LES of a laboratory-scale turbulent premixed flame. While previous studies (e.g. Hawkes [25]), have considered the application of the model to LES of planar flame propagation in an isotropic decaying turbulent flow, the laboratory-scale turbulent premixed methane-air Bunsen-type flames studied by Yuen and Gülder [4] are considered herein. The flames examined are all strongly turbulent and lie well within the thin-reaction zone regime. The study also provides the first detailed comparisons of the Bunsen flame data to LES predictions.

- The comparisons of the LES results of this thesis to the experimental data of Yuen and Gülder [4] provide strong support for the validity of the modelled transport equation for the FSD. As indicated by the comparisons of flame height, FSD, and flame curvature, it was found that the LES-FSD predictions can accurately represent the flame structure, degree of wrinkling of the flame surface, and increases in flame surface area produced by the turbulent fields. The FSD model would appear to be well equipped to represent the dynamics of premixed flame fronts.

- While the flame structure and area are well represented by the FSD subfilter-scale model, the LES predictions of turbulent burning rate do not match well with the experimentally measured values for the stronger turbulent cases with $u'/s_{\mathrm{L}} > 6$-8. For the premixed Bunsen flames, the LES-FSD predictions of total flame area agree both qualitatively and quantitatively with the integrated values of the measured FSD and reach a maximum for $u'/s_{\mathrm{L}} > 6$-8, thereafter remaining relatively insensitive to turbulence intensity. As the FSD model is based on the flamelet concept through which the turbulent burning rate is directly related to the flame area, unlike the measured values, the LES predictions of burning rate correspondingly also do not continue to increase with increasing turbulence intensity and maximum burning rates are achieved for $u'/s_{\mathrm{L}} > 6$-8. While seemingly correct for flames lying within the wrinkled and corrugated flamelet regimes and for lower turbulence intensities, the findings cast doubt on the

validity of the flamelet approximation for flames within the thin reaction zones regime for $u'/s_L > 6$-8.

- The influence of stoichiometry on flame wrinkling and burning rates was also examined herein. From the LES-FSD predictions of both freely-propagating and Bunsen-type premixed flames, it was found that there is a mild dependence of flame wrinkling on stoichiometry for high turbulence intensity and that the lean flames seem to exhibit a greater degree of wrinkling for higher turbulence intensity. This finding seems to be somewhat supported by the experimental data of Yuen and Gülder [6].

- Finally, the mesh resolution requirements of the FSD model was also examined as part of this thesis research and requirements for accurate LES of premixed flames were established. Moreover, for two-dimensional freely-propagating flames, the proposed block-based AMR strategy was found to be very effective in dealing with the rapid variation of the FSD through the flame front and providing more or less grid-independent solutions in an economical manner.

6.2 Recommendations for Future Research

The proposed LES framework with FSD subfilter-scale modelling based on a transported equation for the FSD would seem to be a promising approach for the simulation of turbulent premixed combustion processes. Nevertheless further research is required to make the proposed approach considered herein practical for application to more practical burner and combustor configurations. Future research may involve some of the following work among the many possible avenues:

- While providing accurate predictions of turbulent burning rate for relatively lower turbulent intensities, the FSD model does not appear to provide accurate predictions of turbulent burning rates in the thin reaction zone regime for $u'/s_L > 6$-8. It would be important to first gain a more complete understanding of the FSD model limitations related to burning rate and then explore possible

remedies. In particular, it may be possible to correct some of the deficiencies in the currently subfilter-scale model by incorporating effects of flame curvature and strain on the laminar consumption rate.

- As it has been mentioned in Section 3.2.8, The scalar fluxes of the progress variable, $\widetilde{uc} - \tilde{u}\tilde{c}$, and the flame surface density, $\overline{(u_i)_s} - \tilde{u}_i$, are found to be controlled mainly by non-gradient transport mechanisms. In the current modelled FSD transport equation, NGT has been included in modelling of the scalar flux. It would be interesting to investigate NGT effects in the scalar flux for the progress variable, c. A NGT model for the progress variable devised by Tullis and Cant [170] has been implemented in the current two-dimensional LES-FSD solver, but its affects of the predicted solutions has yet to be explored. This could be the basis for the additional future LES investigations of premixed flames and comparisons with the Bunsen-type flames. Another interesting comparison would be to compare directly the two different modelling approaches for FSD, the algebraic model of Section 3.2.4 and the transport equation approach of Section 3.2.9, for the premixed Bunsen flames. In the current research, the latter approach was used exclusively; however, an algebriac model for the FSD was also implemented in the two-dimensional LES-FSD formulation developed herein using the expression of Charlette *et al.* [79, 80] given in Eq. 3.30. This could be readily extended for use with three-dimensional premixed flames as well.

- While demonstrated for two-dimensional flames, the suitability of the block-based AMR scheme remains to be studied for LES of three-dimensional premixed flames with the FSD model. Future research should involve the investigation of adaptive mesh refinement to LES of turbulent premixed flames using the flame surface density model.

- The present LES framework makes use of an explicit time marching scheme. It would be interesting to investigate the use of parallel implicit time marching schemes based on Newton-Krylov-Schwarz (NKS) strategies for improving the

efficiency of the time integration procedure. The current explicit time-marching scheme may not be optimal and it may be possible to combine the NKS approach with block-based AMR [146] to yield a more efficient approach.

- Further improvements to the LES framework may be possible through the use of high-order finite-volume schemes, which have been proposed and evaluated recently by Ivan [171], in conjunction with high-order explicit commutative filters, which have also been studied in recent work by Deconinck [172].

Bibliography

[1] N. Peters, *Turbulent Combustion*. Cambridge University Press, 2000.

[2] R. Borghi, "Mise au point sur la structure des flammes turbulentes," *Journal de Chimie Physique*, vol. 81, pp. 361–370, 1984.

[3] X. Gao and C. P. T. Groth, "Parallel adaptive mesh refinement scheme for three-dimensional turbulent non-premixed combustion," Paper 2008-1017, AIAA, January 2008.

[4] F. Yuen, *Experimental Investigation of the Dynamics and Structure of Lean-Premixed Turbulent Combustion*. PhD thesis, University of Toronto, August 2009.

[5] F. Yuen and Ö. L. Gülder, "Premixed turbulent flame front structure investigation by rayleigh scattering in the thin reaction zone regime," *Symposium (International) on Combustion*, vol. 32, pp. 1747–1754, 2009.

[6] Ö. L. Gülder and F. T. C. Yuen, "Turbulent premixed flame front dynamics and implications for limits of flamelet hypothesis," *Unpublished Manuspcript*, 2010.

[7] D. A. Knaus, S. S. Sattler, and F. C. Gouldin, "Three-dimensional temperature gradients in premixed turbulent flamelets via cross-plane rayleigh imaging," *Combustion and Flame*, vol. 141, pp. 253–270, 2005.

[8] M. Barrère, "Modeles de combustion," *Revue Générale de Thermique*, vol. 148, pp. 295–308, 1974.

[9] K. N. C. Bray, P. A. Libby, and F. A. Williams, *Turbulent Flows with Premixed Reactants, in Turbulent Reacting Flows*. Springer Verlag, Berlin Heidelburg, New York, eds., 1980.

[10] N. Peters, "Laminar flamelet concepts in turbulent combustion," *Symposium (International) on Combustion*, vol. 21, pp. 1231–1250, 1988.

[11] F. A. Williams, *Combustion Theory*. Benjamin Cummings, Menlo Park, CA, 1985.

[12] R. G. Abdel-Gayed and D. Bradley, "Combustion regimes and the straining of turbulent premixed flames," *Combustion and Flames*, vol. 76, pp. 213–218, 1989.

[13] N. Peters, "The turbulent burning velocity for large-scale and small-scale turbulence," *Journal of Fluid Mechanics*, vol. 384, pp. 107–132, 1999.

[14] H. Pitsch and L. D. de Lageneste, "Large-eddy simulation of premixed turbulent combustion using a level-set approach," in *Proceedings of Combustion Institute*, vol. 29, pp. 2001–2008, 2002.

[15] M. Düsing, A. Sadiki, and J. Janicka, "Towards a classification of models for the numerical simulation of premixed combustion based on a generalized regime diagram," *Combustion Theory and Modelling*, vol. 10, pp. 105–132, 2006.

[16] T. Poinsot and D. Veynante, *Theoretical and Numerical Combustion*. R.T. Edwards Inc., 2001.

[17] T. Poinsot, D. Veynante, and S. Candel, "Quenching processes and premixed turbulent combustion diagrams," *Journal of Fluid Mechanics*, vol. 228, pp. 561–606, 1991.

[18] P. Libby and F. A. Williams, *Turbulent Reacting Flows*. Academic Press Inc., 1994. pp. 1–43.

[19] R. S. Cant and K. N. C. Bray, "Strained laminar flamelet calculations of premixed turbulent combustion in a closed vessel," *Symposium (International) on Combustion*, vol. 22, pp. 791–799, 1989.

[20] G. Damköhler, "Der einfluβ der turbulenz auf flammengeschwindigkeit in gasgemischen," *Z. Elektrochem*, vol. 46, pp. 601–652, 1947. English translation *NASA Technical Memorandum* 1112.

[21] K. N. C. Bray, P. A. Libby, and J. B. Moss, "Unified modelling approach for premixed turbulent combustion- part i: General formulation," *Combustion Flame*, vol. 61, pp. 87–102, 1985.

[22] K. N. C. Bray, "Studies of the turbulent burning velocity," *Proceedings of the Royal Society*, vol. 431, pp. 315–335, 1990.

[23] L. Vervisch, R. Hauguel, P. Domingo, and M. Rullaud, "Three facets of turbulent combustion modelling: Dns of premixed v-flame, les of lifted nonpremixed flame and rans of jet-flame," *Journal of Turbulence*, vol. 5, pp. 1–36, 2004.

[24] S. Cant, "High-performance computing in computational fluid dynamics: Progress and challenges," *Philosophical Transactions: Mathematical, Physical and Engineering Sciences*, vol. 360, no. 1795, pp. 1211–1225, 2002.

[25] E. R. Hawkes, *Large-Eddy Simulation of Premixed Turbulent Combustion*. PhD thesis, University of Cambridge, July 2000.

[26] L. Vervisch, "Dns and les of turbulent combustion." Computational Fluid Dynamics in Chemical Reaction Engineering IV, June 19-24, 2005, Barga, Italy.

[27] B. S. Baldwin and H. Lomax, "Thin-layer approximation and algebraic model for separated turbulent flows," Paper 91–0610, AIAA, 1978.

[28] P. R. Spalart and S. R. Allmaras, "A one-equation turbulence model for aerodynamic flows," Paper 92-0439, AIAA, 1992.

[29] B. E. Launder and D. B. Spalding, *Mathematical Models of Turbulence*. Academic Press, London, 1972.

[30] D. C. Wilcox, "Reassessment of the scale determining equation for advanced turbulence models," *AIAA Journal*, vol. 26, pp. 1299–1310, October 1988.

[31] B. E. Launder, J. G. Reece, and W. Rodi, "Progress in the development of a reynolds-stress turbulence closure," *Journal of Fluid Mechanics*, vol. 68, pp. 537–566, 1975.

[32] H. Lomax, T. H. Pulliam, and D. W. Zingg, *Fundamentals of Computational Fluid Dynamics*. Springer-Verlag Berlin Heidelberg, 2001.

[33] U. Piomelli, "Large-eddy simulation: Achievements and challenges," *Prog. Aerospace Sci.*, vol. 35, pp. 335–362, 1999.

[34] H. Pitsch, "Large-eddy simulation of turbulent combustion," *Annual Review of Fluid Mechanics*, vol. 38, pp. 453–482, 2006.

[35] P. Sagaut, *Large-Eddy Simulation for Incompressible Flows*. Springer, 2002.

[36] C. Wanger, T. Hüttl, and P. Sagaut, eds., *Large-Eddy Simulation for Acoustics*. Cambridge University Press, 2006.

[37] P. Möller, E. Lundgren, and C. Fureby, "Large-eddy simulation of unsteady combustion," *Symposium (International) on Combustion*, vol. 26, pp. 241–248, 1996.

[38] S. Menon and W. H. Jou, "Large-eddy simulation of combustion instability in an axisymmetric ramjet combustor," *Combustion Science and Technology*, vol. 75, pp. 53–72, 1996.

[39] W. W. Kim and S. Menon, "A new dynamic one equation sub grid scale model for large-eddy simulations," Paper 95–0356, AIAA, 1995.

[40] H. G. Weller, G. Tabor, A. D. Gosman, and C. Fureby, "Application of a flame-wrinking les combustion model to a turbulent mixing layer," *Symposium (International) on Combustion*, vol. 27, pp. 899–907, 1998.

[41] C. Angelberger, D. Veynante, F. Egolfopoulos, and T. Poinsot, "Large-eddy simulation of combustion instabilities in turbulent premixed flames," in *Proceedings of the Summer Program of Center for Turbulence Research, Stanford*, pp. 61–82, 1998.

[42] D. Veynante and T. Poinsot, "Large-eddy simulation of combustion instabilities in turbulent premixed burners," Annual Research Briefs 253–274, Center for Turbulence Research, NASA Ames/Stanford Univ., 2000.

[43] E. R. Hawkes and R. S. Cant, "A flame surface density approach to large-eddy simulation of premixed turbulent combustion," *Symposium (International) on Combustion*, vol. 28, pp. 51–58, 2000.

[44] S. Pope, "The evolution of surfaces in turbulence," *International Journal of Engineering Science*, vol. 26, pp. 445–469, 1988.

[45] D. Veynante and L. Vervisch, "Turbulent combustion modeling," *Progress in Energy and Combustion Science*, vol. 28, pp. 193–266, 2002.

[46] U. Schumann, "Large-eddy simulation of turbulent diffusion with chemical reactions in the convective boundary layer," *Atmospheric Environment*, vol. 23, pp. 1713–1727, 1989.

[47] M. Germano, *Direct and Large-Eddy Simulation III.* Kluwer Academic Publishers, Dordrecht, 1999.

[48] J. Gullbrand, "Grid-independent large-eddy simulation in turbulent channel flow using three-dimensional explicit filtering," Annual Research Briefs 331–342, Center for Turbulence Research, NASA Ames/Stanford Univ., 2003.

[49] F. K. Chow and P. Moin, "A further study of numerical errors in large-eddy simulations," *Journal of Computational Physics*, vol. 184, no. 2, pp. 366–380, 2003.

[50] B. Vreman, B. Geurts, and H. Kuerten, "A priori tests of large-eddy simulation of the compressible plane mixing layer," *Journal of Engineering Mathematics*, vol. 29, pp. 299–327, 1995.

[51] M. P. Martin, U. Piomelli, and G. V. Candler, "Subgrid-scale models for compressible large-eddy simulations," *Theoretical and Computational Fluid Dynamics*, vol. 13, pp. 361–376, 2000.

[52] D. Carati, G. Winckelmans, and H. Jeanmart, "On the modelling of the subgrid-scale and filtered-scale stress tensors in large-eddy simulation," *Journal of Fluid Mechanics*, vol. 441, pp. 119–138, 2001.

[53] J. Smagorinsky, "General circulation experiments with the primitive equations," *Monthly Weather Review*, vol. 91, no. 3, pp. 99–165, 1963.

[54] A. Yoshizawa, "Statistical theory for compressible turbulent shear flows, with the application to subgrid modeling," *Physics of Fluids*, vol. 29, pp. 2152–2164, 1986.

[55] E. van Driest, "On turbulent flow near a wall," *Journal of Aeronautical Science*, vol. 23, pp. 1007–1011, 1956.

[56] C. Speziale, "Turbulence modelling for time-dependent rans and vles: A review," *AIAA Journal*, vol. 36, no. 2, pp. 173–184, 1998.

[57] C. Fureby, "Towards large-eddy simulation of flows in complex geometries," Paper 98–2006, AIAA, 1998.

[58] C. Fureby, G. Tabor, H. G. Weller, and A. D. Gosman, "A comparitive study of subgrid scale models in homogeneous isotropic turbulence," *Physics of Fluids*, vol. 9, pp. 1416–1429, 1997.

[59] J. H. Ferziger, *Sub-Grid Scale Modelling.* Cambridge University Press, 1993.

[60] M. Germano, U. Piomelli, P. Moin, and W. H. Cabot, "A dynamic sub-grid scale eddy viscosity model," *Physics of Fluids*, vol. 3, pp. 1760–1765, 1991.

[61] P. Moin, K. Squires, W. Cabot, and S. Lee, "A dynamic subgrid-scale model for compressible turbulence and scalar transport," *Physics of Fluids*, vol. 3, pp. 2746–2757, 1991.

[62] D. K. Lilly, "A proposed modification of the germano subgrid-scale closure method," *Physics of Fluids*, vol. 4, pp. 633–635, 1992.

[63] F. A. Jaberi and S. James, "A dynamic similarity model for large-eddy simulation of turbulent combustion," *Physics of Fluids*, vol. 10, pp. 1775–1777, 1998.

[64] U. Schumann, "Sub-grid scale model for finite difference simulations of turbulent flows in plane channels and annuli," *Journal of Computational Physics*, vol. 18, pp. 376–404, 1975.

[65] H. Schmidt and U. Schumann, "Coherent structure of the convective boundary layer derived from large-eddy simulation," *Journal of Fluid Mechanics*, vol. 200, pp. 511–562, 1989.

[66] A. Yoshizawa, "A statistically derived subgrid model for the large-eddy simulation of turbulence," *Physics of Fluids*, vol. 25, pp. 1532–1538, 1982.

[67] A. Yoshizawa, "Subgrid-scale modelling suggested by a two-scale dia," *Journal of Wind Eng. and Indust. Aerodynamics*, vol. 46, pp. 69–79, 1993.

[68] M. Germano, "Turbulence: the filtering approach," *Journal of Fluid Mechanics*, vol. 238, pp. 325–336, 1992.

[69] S. Ghosal, "Analysis of the discretization errors in les," Annual Research Briefs 3–24, Center for Turbulence Research, NASA Ames/Stanford Univ., 1995.

[70] J. P. Chollet and M. Lesieur, "Parameterization of small scales of three dimensional isotropic turbulence utilizing apectral closures," *Journal of Atmospheric Science*, vol. 38, pp. 2747–2757, 1981.

[71] J. Bardina, J. H. Ferziger, and W. C. Reynolds, "Improved sub-grid model for large-eddy simulation," Paper 80–1357, AIAA, 1980.

[72] S. Métais and M. Lesieur, "Spectral large-eddy simulations of istropic and stably stratified turbulence," *Computers and Fluids*, vol. 239, pp. 157–194, 1992.

[73] D. Knight, G. Zhou, N. Okong'o, and V. Shukla, "Compressible large-eddy simulation using unstructured grids," Paper 98–0585, AIAA, 1998.

[74] O. Colin, F. Ducros, D. Veynante, and T. Poinsot, "A thickened flame model for large-eddy simulations of turbulent premixed combustion," *Physics of Fluids*, vol. 12, no. 7, pp. 1843–1863, 2000.

[75] T. D. Butler and P. J. O'Rourke, "A numerical method for two dimensional unsteady reacting flows," *Symposium (International) on Combustion*, vol. 16, pp. 1503–1515, 1977.

[76] D. Thibaut and S. Candel, "Numerical study of unsteady turbulent premixed combustion application to flashback simulation," *Combustion and Flame*, vol. 115, pp. 53–65, 1998.

[77] D. Veynante and T. Poinsot, "Large-eddy simulation of combustion instabilities in turbulent premixed burners," Annual Research Briefs 253–275, Center for Turbulence Research, NASA Ames/Stanford Univ., 1997.

[78] P. J. O'Rourke and F. V. Bracco, "Two scaling transformations for the numerical computation of multidimensional unsteady laminar flames," *Journal of Computational Physics*, vol. 33, pp. 185–203, 1979.

[79] F. Charlette, C. Meneveau, and D. Veynante, "A power-law flame wrinkling model for LES of premixed turbulent combustion, part I: Non-dynamic formulation and initial tests," *Combustion and Flame*, vol. 131, pp. 159–180, 2002.

[80] F. Charlette, C. Meneveau, and D. Veynante, "A power-law flame wrinkling model for LES of premixed turbulent combustion, part II: Non-dynamic formulation and initial tests," *Combustion and Flame*, vol. 131, pp. 181–197, 2002.

[81] G. H. Markstein, *Nonsteady Flame Propagation*. Pergamon Press, 1964.

[82] V. Yakhot, "Propagation velocity of premixed turbulent flames," *Combustion Science and Technology*, vol. 60, pp. 191–214, 1988.

[83] A. R. Kerstein, W. Ashurst, and F. A. Williams, "Field equation for interface propagation in an unsteady homogeneous flow field," *Physics Review*, vol. 37, pp. 2728–2731, 1988.

[84] H. G. Im, T. S. Lund, and J. H. Ferziger, "Large-eddy simulation of turbulent front propagation wiht dynamic subgrid models," *Physics of Fluids*, vol. 9, pp. 3826–3833, 1997.

[85] V. Smiljanovski, V. Moser, and R. Klein, "A capturing-tracking hybrid scheme for deflagration discontinuities," *Combustion Theory and Modelling*, vol. 1(2), pp. 183–215, 1997.

[86] S. Menon, C. Stone, and N. Patel, "Multi scale modeling for les of engineering designs of large-scale combustors," *42nd AIAA Aerospace Sciences Meeting 2004–0157, Reno*, pp. 1–15, 2004.

[87] M. Freitag and J. Janicka, "Investigation of a strongly swirled unconfined premixed flame using les," in *Proceedings of Combustion Institute*, vol. 31, pp. 1477–1485, 2006.

[88] F. E. Marble and J. E. Broadwell, "The coherent flame model of non-premixed turbulent combustion," *Project Squid Report TRW-9-PU*, 1977.

[89] S. M. Candel and T. J. Poinsot, "Flame stretch and the balance equation for the flame area," *Combustion Science and Technology*, vol. 70, pp. 1–15, 1990.

[90] R. S. Cant, S. B. Pope, and K. N. C. Bray, "Modelling of flamelet surface to volume ratio in turbulent premixed combustion," *Symposium (International) on Combustion*, vol. 23, pp. 809–815, 1990.

[91] E. Maistret, E. Darahiba, T. Poinsot, D. Veynante, F. Lacas, S. Candel, and E. Esposito, *Numerical Combustion*. Springer Verlag, London, 1989.

[92] S. Candel, D. Veynante, F. Lacas, E. Maistret, N. Darahiba, and T. Poinsot, *Recent Advances in Combustion Modelling*. World Scientific, Singapore, 1990.

[93] W. K. Cheng and J. A. Diringer, "Numerical modelling of si engine combustion with a flame sheet model," Tech. Rep. 910268, SAE Technical Paper, 1991.

[94] R. O. S. Prasad and J. P. Gore, "An evaluation of flame surface density models for turbulent premixed jet flames," *Combustion and Flame*, vol. 116, pp. 1–14, 1999.

[95] T. Mantel and R. Borghi, "New model of premixed wrinkled flame propagation based on a scalar dissipation equation," *Combustion and Flame*, vol. 94, pp. 443–457, 1994.

[96] A. Trouvé and T. Poinsot, "The evolution equation for flame surface density in turbulent premixed combustion," *Journal of Fluid Mechanics*, vol. 278, pp. 1–31, 1994.

[97] D. C. Haworth and T. J. Poinsot, "Numerical simulations of lewis number effects in turbulent premixed flames," *Journal of Fluid Mechanics*, vol. 244, pp. 405–436, 1992.

[98] A. Trouvé, "The production of premixed flame surface area in a turbulent shear flow," *Combustion and Flame*, vol. 99, pp. 687–696, 1994.

[99] T. Poinsot, D. C. Haworth, and G. Bruneaux, "Direct simulation and modelling of flame-wall interaction for premixed turbulent combustion," *Combustion and Flame*, vol. 95, pp. 118–132, 1993.

[100] T. Poinsot, S. Candel, and A. Trouvé, "Applications of direct numerical simulation to premixed turbulent combustion," *Progress in Energy and Combustion Science*, vol. 21, pp. 531–576, 1996.

[101] G. Bruneaux, T. Poinsot, and J. H. Ferziger, "Premixed flame-wall interaction in a turbulent channel flow: Budget for the flame surface density evolution equation and modelling," *Journal of Fluid Mechanics*, vol. 349, pp. 191–219, 1997.

[102] W. Kollmann and J. H. Chen, "Pocket formation and the flame surface density equation," *Symposium (International) on Combustion*, vol. 27, pp. 927–934, 1998.

[103] P. K. Yeung, S. S. Girimaji, and S. B. Pope, "Straining and scalar dissipation on material surfaces in turbulence: Implications for flamelets," *Combustion and Flame*, vol. 79, pp. 340–365, 1990.

[104] S. B. Pope, P. K. Yeung, and S. S. Girimaji, "The curvature of material surface in isotropic turbulence," *Physics of Fluids*, vol. 1, pp. 2010–2018, 1989.

[105] D. Veynante, J. M. Duclos, and J. Piana, "Experimental analysis of flamelet models for premixed turbulent combustion," *Symposium (International) on Combustion*, vol. 25, pp. 1249–1256, 1994.

[106] D. Veynante, J. Piana, J. M. Duclos, and C. Martel, "Experimental analysis of flamelet models for premixed turbulent combustion," *Symposium (International) on Combustion*, vol. 26, pp. 413–420, 1996.

[107] F. A. Tap, R. Hilbert, D. Thévenin, and D. Veynante, "A generalized flame surface density modelling approach for the auto-ignition of a turbulent non-premixed system," *Combustion Theory and Modelling*, vol. 8, pp. 165–193, 2004.

[108] M. Boger, D. Veynante, H. Boughanem, and A. Trouvé, "Direct numerical simulation analysis of flame surface density concept for large-eddy simulation of turbulent premixed combustion," *Symposium (International) on Combustion*, vol. 28, pp. 917–925, 1998.

[109] K. N. C. Bray, M. Champion, and P. A. Libby, "The interaction between turbulence and chemistry in premixed turbulent flames," *Turbulent Reacting Flows*, pp. 541–563, 1989.

[110] L. Vervisch, E. Bidaux, K. N. C. Bray, and W. Kollmann, "Surface density function in premixed turbulent combustion modelling, similarities between probability density function and flame surface approach," *Physics of Fluids*, vol. 7, pp. 2496–2503, 1995.

[111] C. Meneveau and T. Poinsot, "Stretching and quenching of flamelets in premixed turbulent combustion," *Combustion and Flame*, vol. 85, pp. 311–332, 1991.

[112] J. M. Duclos and T. Poinsot, "A comparison of flamelet models for turbulent premixed combustion," *Combustion and Flame*, vol. 95, pp. 101–117, 1993.

[113] D. Veynante, A. Trouvè, K. N. C. Bray, and T. Mantel, "Gradient and countergrsdient scalar transport in turbulent premixed flames," *Journal of Fliud Mechanics*, vol. 332, pp. 263–293, 1997.

[114] S. K. Godunov, "Finite-difference method for numerical computations of discontinuous solutions of the equations of fluid dynamics," *Matematicheskii Sbornik*, vol. 47, pp. 271–306, 1959.

[115] J. J. Gottlieb and C. P. T. Groth, "Assessment of Riemann solvers for unsteady one-dimensional inviscid flows of perfect gases," *Journal of Computational Physics*, vol. 78, pp. 437–458, 1988.

[116] P. L. Roe, "Approximate Riemann solvers, parameter vectors, and difference schemes," *Journal of Computational Physics*, vol. 43, pp. 357–372, 1981.

[117] B. Einfeldt, "On Godunov-type methods for gas dynamics," *SIAM Journal on Numerical Analysis*, vol. 25, pp. 294–318, 1988.

[118] M. S. Liou, "A sequel to AUSM, part ii: AUSM$^+$-up for all apeeds," *Journal of Computational Physics*, vol. 214, pp. 137–170, 2006.

[119] T. J. Barth, "Recent developments in high order k-exact reconstruction on unstructured meshes," Paper 93-0668, AIAA, January 1993.

[120] N. Waterson and H. Deconinck, "Design principles for bounded hight-order convection schemes–a unified approach," *Journal of Computational Physics*, vol. 224, pp. 128–207, 2007.

[121] T. J. Barth and D. C. Jespersen, "The design and application of upwind schemes on unstructured meshes," Paper 89-0366, AIAA, January 1989.

[122] S. Osher and F. Solomon, "Upwind difference schemes for hyperbolic systems of conservation laws," *Mathematics of Computation*, vol. 38, no. 158, pp. 339–374, 1982.

[123] B. van Leer, "On the relation between the upwind-difference schemes of Godunov's engquist osher and roe," *SIAM Journal for Scientific and Statistical Computing*, vol. 5, pp. 1–20, 1984.

[124] A. Harten, P. D. Lax, and B. van Leer, "On upstream differencing and Godunov-type schemes for hyperbolic conservation laws," *SIAM Review*, vol. 25, no. 1, pp. 35–61, 1983.

[125] J. Sachdev, *Parallel Solution-Adaptive Method for Predicting Solid Propellant Rocket Motor Core Flows*. PhD thesis, University of Toronto, March 2007.

[126] X. Gao, *A Parallel Solution-Adaptive Method for Turbulent Non-Premixed Combusting Flows*. PhD thesis, University of Toronto, August 2008.

[127] A. Harten, "On a class of high resolution total-variation-stable finite-difference schemes," *SIAM Journal on Numerical Analysis*, vol. 21, pp. 1–23, 1984.

[128] M. S. Liou and C. J. Steffen, "A new flux splitting scheme," *Journal of Computational Physics*, vol. 107, pp. 23–39, 1993.

[129] S. R. Mathur and J. Y. Murthy, "A pressure-based method for unstructured meshes," *Numerical Heat Transfer*, vol. 31, pp. 191–215, 1997.

[130] C. Hirsch, *Numerical Computation of Internal and External Flows, Volume 1, Fundamentals of Numerical Discretization*. Toronto: John Wiley & Sons, 1989.

[131] C. Hirsch, *Numerical Computation of Internal and External Flows, Volume 2, Computational Methods for Inviscid and Viscous Flows*. Toronto: John Wiley & Sons, 1990.

[132] M. J. Berger and J. Oliger, "Adaptive mesh refinement for hyperbolic partial differential equations," *Journal of Computational Physics*, vol. 53, pp. 484–512, 1984.

[133] M. J. Berger and P. Colella, "Local adaptive mesh refinement for shock hydrodynamics," *Journal of Computational Physics*, vol. 82, pp. 67–84, 1989.

[134] K. G. Powell, P. L. Roe, and J. Quirk, "Adaptive-mesh algorithms for computational fluid dynamics," in *Algorithmic Trends in Computational Fluid Dynmaics* (M. Y. Hussaini, A. Kumar, and M. D. Salas, eds.), pp. 303–337, New York: Springer-Verlag, 1993.

[135] M. J. Berger and R. J. LeVeque, "An adaptive Cartesian mesh algorithm for the Euler equations in arbitrary geometries," Paper 89-1930, AIAA, June 1989.

[136] M. J. Berger and J. S. Saltzman, "AMR on the CM-2," *Applied Numerical Mathematics*, vol. 14, pp. 239–253, 1994.

[137] M. J. Aftomis, M. J. Berger, and J. E. Melton, "Robust and efficient Cartesian mesh generation for component-base geometry," *AIAA Journal*, vol. 36, no. 6, pp. 952–960, 1998.

[138] J. J. Quirk, *An Adaptive Grid Algorithm for Computational Shock Hydrodynamics*. PhD thesis, Cranfield Institute of Technology, January 1991.

[139] J. J. Quirk and U. R. Hanebutte, "A parallel adaptive mesh refinement algorithm," Report 93-63, ICASE, August 1993.

[140] D. De Zeeuw and K. G. Powell, "An adaptively refined Cartesian mesh solver for the Euler equations," *Journal of Computational Physics*, vol. 104, pp. 56–68, 1993.

[141] B. van der Holst and R. Keppens, "Hybrid block-amr in cartesian and curvilinear coordinates:mhd applications," *Journal of Computational Physics*, vol. 226, pp. 925–946, 2007.

[142] R. L. Davis and J. F. Dannenhoffer, "Decomposition and parallelization strategies for adaptive grid-embedding techniques," *International Journal of Computational Fluid Dynamics*, vol. 1, pp. 79–93, 1993.

[143] M. Sun and K. Takayama, "Conservative smoothing on an adaptive quadrilateral grid," *Journal of Computational Physics*, vol. 150, pp. 143–180, 1999.

[144] C. P. T. Groth, D. L. D. Zeeuw, K. G. Powell, T. I. Gombosi, and Q. F. Stout, "A parallel solution-adaptive scheme for ideal magnetohydrodynamics," Paper 99-3273, AIAA, June 1999.

[145] C. P. T. Groth, D. L. De Zeeuw, T. I. Gombosi, and K. G. Powell, "Global three-dimensional MHD simulation of a space weather event: CME formation, interplanetary propagation, and and interaction with the magnetosphere," *Journal of Geophysical Research*, vol. 105, no. A11, pp. 25053–25078, 2000.

[146] S. A. Northrup and C. P. T. Groth, "Prediction of unsteady laminar flames using a parallel implicit aaptive mesh refinement algorithm," in *Proceedings of the 6th U.S. National Combustion Meeting, Ann Arbor, MI, USA*, May 18–21, 2009.

[147] J. Sachdev, C. Groth, and J. Gottlieb, "A parallel solution-adaptive scheme for predicting multi-phase core flows in solid propellant rocket motors," *International Journal of Computational Fluid Dynamics*, vol. 19, no. 2, pp. 159–177, 2005.

[148] W. Gropp, E. Lusk, and A. Skjellum, *Using MPI*. Cambridge, Massachussets: MIT Press, 1999.

[149] S. A. Northrup, "A parallel adaptive-mesh refinement scheme for predicting laminar diffusion flames," Master's thesis, University of Toronto, 2004.

[150] H. K. Moffat and D. Goodwin, "Cantera – object-oriented software for reacting flow." http://cantera.googlecode.com, August 2009.

[151] B. Hakberg and A. D. Gosman, "Analytical determination of turbulent flame speed from combustion models," *Symposium (International) on Combustion*, vol. 20, pp. 225–232, 1985.

[152] F. Fichot, F. Lacas, D. Veynante, and S. M. Candel, "One-dimensional propagation of a premixed turbulent flame with coherent flame model," *Combustion Science and Technology*, vol. 90, pp. 25–60, 1993.

[153] R. S. Cant, C. J. Rutland, and A. Trouvé, "Statistics for laminar flamelet modelling," in *Proceedings of the Summer Program of Center for Turbulence Research, Stanford*, pp. 271–279, 1990.

[154] S. S. Girimaji and S. B. Pope, "Propagating surfaces in isotropic turbulence," *Journal of Fluid Mechanics*, vol. 234, pp. 247–277, 1992.

[155] R. S. Rogallo, "Numerical experiments in homogeneous turbulence." NASA Technical Memorandum 81315, 1981.

[156] F. E. Hernandez-Perez, F. T. C. Yuen, C. P. T. Groth, and Ö. L. Gülder, "Les of a laboratory-scale turbulent premixed bunsen flame using fsd, pcm-fdi and thickened flame models," in *Proceedings of Combustion Institute (In Press)*, vol. 33, 2010.

[157] E. R. Hawkes and J. H. Chen, "Direct numerical simulation of hydrogen-enriched lean premixed methane-air flames," *Combustion and Flame*, vol. 138, pp. 405–436, 2004.

[158] T. Echekki and J. H. Chen, "Unsteady strain rate and curvature effects in turbulent premixed methane-air flames," *Journal of Computational Physics*, vol. 118, pp. 24–37, 1996.

[159] C. F. Kaminski, X. S. Bai, J. Hult, A. Dreizler, S. Lindenmaier, and L. Fuchs, "Flame growth and wrinkling in a turbulent flow," *Applied Physics B: Lasers and Optics*, vol. 71, pp. 711–716, 2000.

[160] S. S. Sattler, D. A. Kanus, and F. C. Gouldin, "Determination of three-dimensional flamelet orientation distributions in turbulent v-flames from two-dimensional image data," in *Proceedings of Combustion Institute*, vol. 29, pp. 1785–1792, 2002.

[161] I. G. Shepherd, R. K. Cheng, T. Plessing, C. Kortschik, and N. Peters, "Premixed flame front structure in intense turbulence," in *Proceedings of Combustion Institute*, vol. 29, pp. 1833–1840, 2002.

[162] D. Most, F. Dinkelacker, and A. Leipertz, "Lifted reaction zones in premixed turbulent bluff-body sstabilized flames," in *Proceedings of Combustion Institute*, vol. 29, pp. 1801–1808, 2002.

[163] Y. C. Chen, P. A. M. Kalt, R. W. Bilger, and N. Swaminathan, "Effects of mean flow divergence on turbulent scalar flux and local flame structure in premixed turbulent combustion," in *Proceedings of Combustion Institute*, vol. 29, pp. 1863–1871, 2002.

[164] S. A. Filatyev, J. F. Driscoll, C. D. Carter, and J. M. Donbar, "Measured properties of turbulent premixed flames for model assessment, including burning velocities, strech rates, and surface densities," *Combustion and Flame*, vol. 141, pp. 1–21, 2005.

[165] J. B. Bell, M. S. Day, J. F. Grcar, M. J. Lijewski, J. F. Driscoll, and S. A. Filatyev, "Numerical simulation of a laboratory-scale turbulent slot flame," in *Proceedings of Combustion Institute*, vol. 31, pp. 1299–1307, 2007.

[166] J. B. Bell, M. S. Day, I. G. Shepherd, M. R. Johnson, R. K. Cheng, and J. F. G. *et. al*, "Numerical simulation of a laboratory-scale turbulent v-flame," in *Proceedings of National Academy of Sciences*, vol. 102, pp. 10006–100011, 2005.

[167] R. Sankaran, E. R. Hamkes, and J. H. Chen, "Structure of a spatially developing turbulent lean methane-air bunsen flame," in *Proceedings of Combustion Institute*, vol. 31, pp. 1291–1298, 2007.

[168] I. G. Shepherd and W. M. T. Ashurst, "Flame front geometry in premixed turbulent flames," in *Proceedings of Combustion Institute*, vol. 24, pp. 485–491, 1992.

[169] D. Pavé, *Contribution á l'étude de la Structure des Flammes Turbulentes de Preémélanges Pauvres de Méthane-Air*. PhD thesis, University of Orléans, France, October 2002.

[170] S. Tullis and R. S. Cant, "Scalar transport modeling in large eddy simulation of turbulent premixed flames," in *Proceedings of Combustion Institute*, vol. 29, pp. 2097–2104, 2002.

[171] L. Ivan and C. P. T. Groth, "High-order central eno finite-volume scheme with adaptive mesh refinement," Paper 2007-4323, AIAA, June 2007.

[172] W. Deconinck, "Design and application of discrete explicit filters for large-eddy simulation of compressible turbulent flows," Master's thesis, University of Toronto, March 2008.

Appendix A

Eigensystem of the Inviscid Jacobian

The Favre-filtered conservation equations for LES of premixed turbulent flames with FSD model can be written as follows:

$$\frac{\partial \mathbf{U}}{\partial t} + \frac{\partial(\mathbf{F}_\mathrm{I} + \mathbf{F}_\mathrm{V})}{\partial x} + \frac{\partial(\mathbf{G}_\mathrm{I} + \mathbf{G}_\mathrm{V})}{\partial y} + \frac{\partial(\mathbf{H}_\mathrm{I} + \mathbf{H}_\mathrm{V})}{\partial z} = \mathbf{S}, \tag{A.1}$$

where $\mathbf{F}_\mathrm{I}$, $\mathbf{G}_\mathrm{I}$, and $\mathbf{H}_\mathrm{I}$ are inviscid fluxes, $\mathbf{F}_\mathrm{V}$, $\mathbf{G}_\mathrm{V}$, and $\mathbf{H}_\mathrm{V}$ are viscous fluxes, and $\mathbf{U}$ is the conservative vector. The inviscid fluxes and conservative variable vector can be expressed as

$$\mathbf{U} = [\bar{\rho}, \bar{\rho}\tilde{u}, \bar{\rho}\tilde{v}, \bar{\rho}\tilde{w}, \bar{\rho}\tilde{E}, \bar{\rho}\tilde{c}, \bar{\rho}\tilde{\Sigma}, \bar{\rho}\tilde{k}]^\mathrm{T}, \tag{A.2}$$

$$\mathbf{F}_\mathrm{I} = [\bar{\rho}\tilde{u}, \bar{\rho}\tilde{u}\tilde{u} + \bar{p}_\mathrm{t}, \bar{\rho}\tilde{u}\tilde{v}, \bar{\rho}\tilde{u}\tilde{w}, (\bar{\rho}\tilde{E} + \bar{p}_\mathrm{t})\tilde{u}, \bar{\rho}\tilde{c}\tilde{u}, \bar{\rho}\tilde{\Sigma}\tilde{u}, \bar{\rho}\tilde{k}\tilde{u}]^\mathrm{T}, \tag{A.3}$$

$$\mathbf{G}_\mathrm{I} = [\bar{\rho}\tilde{v}, \bar{\rho}\tilde{u}\tilde{v}, \bar{\rho}\tilde{v}\tilde{v} + \bar{p}_\mathrm{t}, \bar{\rho}\tilde{v}\tilde{w}, (\bar{\rho}\tilde{E} + \bar{p}_\mathrm{t})\tilde{v}, \bar{\rho}\tilde{c}\tilde{v}, \bar{\rho}\tilde{\Sigma}\tilde{v}, \bar{\rho}\tilde{k}\tilde{v}]^\mathrm{T}, \tag{A.4}$$

$$\mathbf{H}_\mathrm{I} = [\bar{\rho}\tilde{w}, \bar{\rho}\tilde{u}\tilde{w}, \bar{\rho}\tilde{v}\tilde{w}, \bar{\rho}\tilde{w}\tilde{w} + \bar{p}_\mathrm{t}, (\bar{\rho}\tilde{E} + \bar{p}_\mathrm{t})\tilde{w}, \bar{\rho}\tilde{c}\tilde{w}, \bar{\rho}\tilde{\Sigma}\tilde{w}, \bar{\rho}\tilde{k}\tilde{w}]^\mathrm{T}, \tag{A.5}$$

where the total energy is defined as

$$\tilde{E} = \check{h} + \frac{1}{2}(\tilde{u}^2 + \tilde{v}^2 + \tilde{w}^2) + \tilde{k} - \frac{\bar{p}_\mathrm{t}}{\bar{\rho}}, \tag{A.6}$$

and the Favre-filtered enthalpy, $\check{h}$, and the turbulence pressure, $\bar{p}_\mathrm{t}$, have the form as

$$\check{h} = \check{h}_\mathrm{s} + \sum_{n=1}^{N_\mathrm{s}} \tilde{Y}_n \Delta h^0_{\mathrm{f},n}, \tag{A.7}$$

$$\bar{p}_\mathrm{t} = \bar{p} + \frac{2\bar{\rho}\tilde{k}}{3}. \tag{A.8}$$

Rewriting the above equation system A.1 in terms of primitive parameters, it becomes

$$\frac{\partial \mathbf{W}}{\partial t} + \mathbf{A}_\mathrm{I}\frac{\partial \mathbf{W}}{\partial x} + \mathbf{B}_\mathrm{I}\frac{\partial \mathbf{W}}{\partial y} + \mathbf{C}_\mathrm{I}\frac{\partial \mathbf{W}}{\partial z} = \mathbf{A}_\mathrm{V}\frac{\partial \mathbf{W}}{\partial x} + \mathbf{B}_\mathrm{V}\frac{\partial \mathbf{W}}{\partial y} + \mathbf{C}_\mathrm{V}\frac{\partial \mathbf{W}}{\partial z} + \mathbf{S}, \tag{A.9}$$

where $\mathbf{A}_\mathrm{I}$, $\mathbf{B}_\mathrm{I}$, and $\mathbf{C}_\mathrm{I}$ are the inviscid flux Jacobian matrices, $\mathbf{A}_\mathrm{V}$, $\mathbf{B}_\mathrm{V}$, and $\mathbf{C}_\mathrm{V}$ are the viscous flux Jacobian matrices, and $\mathbf{W}$ is the primitive vector. They are defined as

$$\mathbf{A}_\mathrm{I} = \frac{\partial \mathbf{F}_\mathrm{I}}{\partial \mathbf{W}}, \quad \mathbf{B}_\mathrm{I} = \frac{\partial \mathbf{G}_\mathrm{I}}{\partial \mathbf{W}}, \quad \mathbf{C}_\mathrm{I} = \frac{\partial \mathbf{H}_\mathrm{I}}{\partial \mathbf{W}}, \tag{A.10}$$

$$\mathbf{W} = [\bar{\rho}, \tilde{u}, \tilde{v}, \tilde{w}, \bar{p}_\mathrm{t}, \tilde{c}, \tilde{\Sigma}, \tilde{k}]^\mathrm{T}. \tag{A.11}$$

The Roe's approximate Riemann solver used in this research requires knowledge of the inviscid flux Jacobian matrices, $\mathbf{A}_\mathrm{I}$, $\mathbf{B}_\mathrm{I}$, and $\mathbf{C}_\mathrm{I}$, and their associated eigenvalues and eigenvectors.

The Jacobian of the inviscid flux in x-direction, $\frac{\partial \mathbf{F}}{\partial \mathbf{U}}$, is

$$\frac{\partial \mathbf{F}}{\partial \mathbf{U}} = \begin{bmatrix} 0 & 1 & 0 & 0 & 0 & 0 & 0 & 0 \\ A_{21} & \tilde{u}(2-\alpha) & -\tilde{v}\alpha & -\tilde{w}\alpha & \alpha & -\check{\eta}\alpha & 0 & -\alpha \\ -\tilde{u}\tilde{v} & \tilde{v} & \tilde{u} & 0 & 0 & 0 & 0 & 0 \\ -\tilde{u}\tilde{w} & \tilde{w} & 0 & \tilde{u} & 0 & 0 & 0 & 0 \\ A_{51} & A_{52} & -\tilde{u}\tilde{v}\alpha & -\tilde{u}\tilde{w}\alpha & -\frac{\tilde{u}C_\mathrm{p}}{\alpha R} & -\tilde{u}\check{\eta}\alpha & 0 & -\tilde{u}\alpha \\ -\tilde{u}\tilde{c} & \tilde{c} & 0 & 0 & 0 & \tilde{u} & 0 & 0 \\ -\tilde{u}\tilde{\Sigma} & \tilde{\Sigma} & 0 & 0 & 0 & 0 & \tilde{u} & 0 \\ -\tilde{u}\tilde{k} & \tilde{k} & 0 & 0 & 0 & 0 & 0 & \tilde{u} \end{bmatrix}, \tag{A.12}$$

where

$$\alpha = \frac{R}{C_\mathrm{p} - R}, \tag{A.13}$$

$$\check{\eta} = \sum_{n=1}^{N_s} (\check{h}_i - C_\mathrm{p}\frac{R_i}{R})\frac{\partial \tilde{Y}_i}{\partial \tilde{c}}, \tag{A.14}$$

$$A_{21} = \frac{1}{2}\alpha\tilde{V}^2 - \tilde{u} - \alpha\check{h} + a_\mathrm{t}^2 + \alpha\tilde{c}\check{\eta}, \tag{A.15}$$

$$A_{51} = \tilde{u}[\frac{1}{2}(\alpha-1)\tilde{V}^2 - \frac{C_\mathrm{p}\alpha}{R}\check{h} - \tilde{k} + a_\mathrm{t}^2 + \alpha\tilde{c}\check{\eta}], \tag{A.16}$$

$$A_{52} = \check{H} - \alpha\tilde{u}^2, \tag{A.17}$$

and $\tilde{V}^2 = \tilde{u}^2 + \tilde{v}^2 + \tilde{w}^2$, $\check{H} = \check{h} + \tilde{V}^2/2 + \tilde{k}$, and $a_\mathrm{t} = \sqrt{\frac{C_\mathrm{p}\bar{p}_\mathrm{t}}{\bar{\rho}(C_\mathrm{p}-R)}}$.

The eigenvalues for the Jacobian matrix $\frac{\partial \mathbf{F}}{\partial \mathbf{U}}$ are as follows:

$$\lambda_1 = \tilde{u} - a_\mathrm{t}, \quad \lambda_2 = \tilde{u}, \quad \lambda_3 = \tilde{u}, \quad \lambda_4 = \tilde{u} + a_\mathrm{t}, \quad \lambda_5 = \tilde{u}, \quad \lambda_6 = \tilde{u}, \quad \lambda_7 = \tilde{u}, \quad \lambda_8 = \tilde{u},$$

where the turbulence sound of speed, a_t, is

$$a_\mathrm{t} = \sqrt{\frac{C_\mathrm{p}\bar{p}_\mathrm{t}}{\bar{\rho}(C_\mathrm{p} - R)}}. \tag{A.18}$$

The left primitive eigenvector matrix in x-direction, L_{px}, corresponding to the eigenvalues given above is

$$L_{px} = \begin{bmatrix} 0 & -\frac{\bar{\rho}}{2a_t} & 0 & 0 & -\frac{1}{2a_t^2} & 0 & 0 & 0 \\ 1 & 0 & 0 & 0 & -\frac{1}{a_t^2} & 0 & 0 & 0 \\ 0 & 0 & 1 & 0 & 0 & 0 & 0 & 0 \\ 0 & 0 & 0 & 1 & 0 & 0 & 0 & 0 \\ 0 & \frac{\bar{\rho}}{2a_t} & 0 & 0 & \frac{1}{2a_t^2} & 0 & 0 & 0 \\ 0 & 0 & 0 & 0 & 0 & 1 & 0 & 0 \\ 0 & 0 & 0 & 0 & 0 & 0 & 1 & 0 \\ 0 & 0 & 0 & 0 & 0 & 0 & 0 & 1 \end{bmatrix}. \tag{A.19}$$

The right conservative eigenvector matrix in x-direction, R_{cx}, corresponding to the eigenvalues given above is

$$R_{cx} = \begin{bmatrix} 1 & 1 & 0 & 0 & 1 & 0 & 0 & 0 \\ \tilde{u} - a_t & \tilde{u} & 0 & 0 & \tilde{u} + a_t & 0 & 0 & 0 \\ \tilde{v} & \tilde{v} & \bar{\rho} & 0 & \tilde{v} & 0 & 0 & 0 \\ \tilde{w} & \tilde{w} & 0 & \bar{\rho} & \tilde{w} & 0 & 0 & 0 \\ \check{H} - \tilde{u}a_t & \check{H} - a_t^2 & \bar{\rho}\bar{v} & \bar{\rho}\bar{w} & \check{H} + \tilde{u}a_t & \bar{\rho}\check{\eta} & 0 & \bar{\rho} \\ \tilde{c} & \tilde{c} & 0 & 0 & \tilde{c} & \bar{\rho} & 0 & 0 \\ \tilde{\Sigma} & \tilde{\Sigma} & 0 & 0 & \tilde{\Sigma} & 0 & \bar{\rho} & 0 \\ \tilde{k} & \tilde{k} & 0 & 0 & \tilde{k} & 0 & 0 & \bar{\rho} \end{bmatrix}. \tag{A.20}$$

Appendix B

Summary of Filtered Governing Equations for Cartesian Frame

The filtered Navier-Stokes equations for a three-dimensional compressible fluid using the subfilter models can be summarized as

$$\frac{\partial \mathbf{U}}{\partial t} + \frac{\partial \mathbf{F_I}}{\partial x} + \frac{\partial \mathbf{G_I}}{\partial y} + \frac{\partial \mathbf{H_I}}{\partial z} = \frac{\partial \mathbf{F_V}}{\partial x} + \frac{\partial \mathbf{G_V}}{\partial y} + \frac{\partial \mathbf{H_V}}{\partial z} + \mathbf{S}, \tag{B.1}$$

where

$$\mathbf{U} = \begin{pmatrix} \bar{\rho} \\ \bar{\rho}\tilde{u} \\ \bar{\rho}\tilde{v} \\ \bar{\rho}\tilde{w} \\ \bar{\rho}\tilde{E} \\ \bar{\rho}\tilde{c} \\ \bar{\rho}\tilde{\Sigma} \\ \bar{\rho}\tilde{k} \end{pmatrix}, \tag{B.2}$$

$$\mathbf{F_I} = \begin{pmatrix} \bar{\rho}\tilde{u} \\ \bar{\rho}\tilde{u}\tilde{u} + \bar{p} \\ \bar{\rho}\tilde{u}\tilde{v} \\ \bar{\rho}\tilde{u}\tilde{w} \\ (\bar{\rho}\tilde{E} + \bar{p})\tilde{u} \\ \bar{\rho}\tilde{c}\tilde{u} \\ \bar{\rho}\tilde{\Sigma}\tilde{u} \\ \bar{\rho}\tilde{k}\tilde{u} \end{pmatrix}, \qquad \mathbf{G_I} = \begin{pmatrix} \bar{\rho}\tilde{v} \\ \bar{\rho}\tilde{u}\tilde{v} \\ \bar{\rho}\tilde{v}\tilde{v} + \bar{p} \\ \bar{\rho}\tilde{v}\tilde{w} \\ (\bar{\rho}\tilde{E} + \bar{p})\tilde{v} \\ \bar{\rho}\tilde{c}\tilde{v} \\ \bar{\rho}\tilde{\Sigma}\tilde{v} \\ \bar{\rho}\tilde{k}\tilde{v} \end{pmatrix}, \qquad \mathbf{H_I} = \begin{pmatrix} \bar{\rho}\tilde{w} \\ \bar{\rho}\tilde{u}\tilde{w} \\ \bar{\rho}\tilde{v}\tilde{w} \\ \bar{\rho}\tilde{w}\tilde{w} + \bar{p} \\ (\bar{\rho}\tilde{E} + \bar{p})\tilde{w} \\ \bar{\rho}\tilde{c}\tilde{w} \\ \bar{\rho}\tilde{\Sigma}\tilde{w} \\ \bar{\rho}\tilde{k}\tilde{w} \end{pmatrix}, \tag{B.3}$$

$$\mathbf{F_V} = \begin{pmatrix} 0 \\ \check{\tau}_{xx} + \sigma_{xx} \\ \check{\tau}_{xy} + \sigma_{xy} \\ \check{\tau}_{xz} + \sigma_{xz} \\ \tilde{u}(\check{\tau}_{xx} + \sigma_{xx}) + \tilde{v}(\check{\tau}_{xy} + \sigma_{xy}) + \tilde{w}(\check{\tau}_{xz} + \sigma_{xz}) - (\check{q}_x + \vartheta_x) \\ \tilde{A}_x \\ \tilde{B}_x \\ \tilde{C}_x \end{pmatrix}, \tag{B.4}$$

$$\mathbf{G_V} = \begin{pmatrix} 0 \\ \check{\tau}_{xy} + \sigma_{xy} \\ \check{\tau}_{yy} + \sigma_{yy} \\ \check{\tau}_{yz} + \sigma_{yz} \\ \tilde{u}(\check{\tau}_{xy} + \sigma_{xy}) + \tilde{v}(\check{\tau}_{yy} + \sigma_{yy}) + \tilde{w}(\check{\tau}_{yz} + \sigma_{yz}) - (\check{q}_y + \vartheta_y) \\ \tilde{A}_y \\ \tilde{B}_y \\ \tilde{C}_y \end{pmatrix}, \tag{B.5}$$

$$\mathbf{H_V} = \begin{pmatrix} 0 \\ \check{\tau}_{xz} + \sigma_{xz} \\ \check{\tau}_{yz} + \sigma_{yz} \\ \check{\tau}_{zz} + \sigma_{zz} \\ \tilde{u}(\check{\tau}_{xz} + \sigma_{xz}) + \tilde{v}(\check{\tau}_{yz} + \sigma_{yz}) + \tilde{w}(\check{\tau}_{zz} + \sigma_{zz}) - (\check{q}_z + \vartheta_z) \\ \tilde{A}_z \\ \tilde{B}_z \\ \tilde{C}_z \end{pmatrix}, \tag{B.6}$$

$$\mathbf{S} = \begin{pmatrix} 0 \\ 0 \\ 0 \\ 0 \\ 0 \\ \bar{\dot{\omega}} \\ \tilde{S}_{\Sigma 1} + \tilde{S}_{\Sigma 2} + \tilde{S}_{\Sigma 3} + \tilde{S}_{\Sigma 4} + \tilde{S}_{\Sigma 5} \\ \tilde{S}_k \end{pmatrix}, \tag{B.7}$$

$$\check{\tau}_{xx} = \frac{2}{3}\check{\mu}\big(2\frac{\partial \tilde{u}}{\partial x} - \frac{\partial \tilde{v}}{\partial y} - \frac{\partial \tilde{w}}{\partial z}\big), \qquad \sigma_{xx} = -\bar{\rho}(\widetilde{uu} - \tilde{u}\tilde{u}), \tag{B.8}$$

$$\check{\tau}_{yy} = \frac{2}{3}\check{\mu}\big(2\frac{\partial \tilde{v}}{\partial y} - \frac{\partial \tilde{u}}{\partial x} - \frac{\partial \tilde{w}}{\partial z}\big), \qquad \sigma_{yy} = -\bar{\rho}(\widetilde{vv} - \tilde{v}\tilde{v}), \tag{B.9}$$

$$\check{\tau}_{zz} = \frac{2}{3}\check{\mu}\big(2\frac{\partial \tilde{w}}{\partial z} - \frac{\partial \tilde{u}}{\partial x} - \frac{\partial \tilde{v}}{\partial y}\big), \qquad \sigma_{zz} = -\bar{\rho}(\widetilde{ww} - \tilde{w}\tilde{w}), \tag{B.10}$$

$$\check{\tau}_{xy} = \check{\mu}\Big(\frac{\partial \tilde{u}}{\partial y} + \frac{\partial \tilde{v}}{\partial x}\Big), \qquad \sigma_{xy} = -\bar{\rho}(\widetilde{uv} - \tilde{u}\tilde{v}), \tag{B.11}$$

$$\check{\tau}_{xz} = \check{\mu}\Big(\frac{\partial \tilde{u}}{\partial z} + \frac{\partial \tilde{w}}{\partial x}\Big), \qquad \sigma_{xz} = -\bar{\rho}(\widetilde{uw} - \tilde{u}\tilde{w}), \tag{B.12}$$

$$\check{\tau}_{yz} = \check{\mu}\Big(\frac{\partial \tilde{v}}{\partial z} + \frac{\partial \tilde{w}}{\partial y}\Big), \qquad \sigma_{yz} = -\bar{\rho}(\widetilde{vw} - \tilde{v}\tilde{w}), \tag{B.13}$$

$$\check{q}_x = -\bar{\lambda}\frac{\partial \tilde{T}}{\partial x}, \qquad \vartheta_x = \widetilde{uT} - \tilde{u}\tilde{T}, \tag{B.14}$$

$$\check{q}_y = -\bar{\lambda}\frac{\partial \tilde{T}}{\partial y}, \qquad \vartheta_y = \widetilde{vT} - \tilde{v}\tilde{T}, \tag{B.15}$$

$$\check{q}_z = -\bar{\lambda}\frac{\partial \tilde{T}}{\partial z}, \qquad \vartheta_z = \widetilde{wT} - \tilde{w}\tilde{T}. \tag{B.16}$$

Models for subfilter-scale terms are:

- Subfilter stress term which is modeled by eddy-viscosity model as

$$\sigma_{ij} = 2\bar{\rho}\nu_{\mathrm{t}}(\check{S}_{ij} - \frac{1}{3}\check{S}_{kk}\delta_{ij}) + \frac{1}{3}\sigma_{kk}\delta_{ij}. \tag{B.17}$$

  It can be expressed in three-space dimensions as

$$\sigma_{xx} = 2\bar{\rho}\nu_{\mathrm{t}}(\check{S}_{xx} - \frac{1}{3}\check{S}_{kk}) + \frac{1}{3}\sigma_{kk}, \tag{B.18}$$

$$\sigma_{yy} = 2\bar{\rho}\nu_{\mathrm{t}}(\check{S}_{yy} - \frac{1}{3}\check{S}_{kk}) + \frac{1}{3}\sigma_{kk}, \tag{B.19}$$

$$\sigma_{zz} = 2\bar{\rho}\nu_{\mathrm{t}}(\check{S}_{zz} - \frac{1}{3}\check{S}_{kk}) + \frac{1}{3}\sigma_{kk}, \tag{B.20}$$

$$\sigma_{xy} = 2\bar{\rho}\nu_{\mathrm{t}}\check{S}_{xy}, \qquad \sigma_{xz} = 2\bar{\rho}\nu_{\mathrm{t}}\check{S}_{xz}, \qquad \sigma_{yz} = 2\bar{\rho}\nu_{\mathrm{t}}\check{S}_{yz}, \tag{B.21}$$

  where

$$\check{S}_{xx} = \frac{\partial \tilde{u}}{\partial x}, \qquad \check{S}_{yy} = \frac{\partial \tilde{v}}{\partial y}, \qquad \check{S}_{zz} = \frac{\partial \tilde{w}}{\partial z}, \tag{B.22}$$

$$\check{S}_{xy} = \frac{1}{2}\Big(\frac{\partial \tilde{u}}{\partial y} + \frac{\partial \tilde{v}}{\partial x}\Big), \qquad \check{S}_{xz} = \frac{1}{2}\Big(\frac{\partial \tilde{u}}{\partial z} + \frac{\partial \tilde{w}}{\partial x}\Big), \qquad \check{S}_{yz} = \frac{1}{2}\Big(\frac{\partial \tilde{v}}{\partial z} + \frac{\partial \tilde{w}}{\partial y}\Big). \tag{B.23}$$

  There are two models for eddy-viscosity given by

(a) Smagorinsky model for compressible flow as

$$\nu_{\mathrm{t}} = C_s\Delta^2|\check{S}|, \qquad \sigma_{kk} = -2C_I\bar{\rho}\Delta^2|\check{S}|^2, \qquad \mathcal{C}_I = 0.09, \tag{B.24}$$

where

$$C_s = 0.16, \qquad |\check{S}| = \sqrt{2\check{S}_{ij}\check{S}_{ij}}, \qquad \check{S}_{ij} = \frac{1}{2}\Big(\frac{\partial\tilde{u}_i}{\partial x_j} + \frac{\partial\tilde{u}_j}{\partial x_i}\Big). \tag{B.25}$$

In three dimensions, the strain rate tensor, $\check{S}_{ij}$ becomes

$$|\check{S}_{xx}| = \sqrt{2}\frac{\partial\tilde{u}}{\partial x}, \qquad |\check{S}_{yy}| = \sqrt{2}\frac{\partial\tilde{v}}{\partial y}, \qquad |\check{S}_{zz}| = \sqrt{2}\frac{\partial\tilde{w}}{\partial z}, \tag{B.26}$$

$$|\check{S}_{xy}| = \sqrt{\frac{1}{2}}\Big(\frac{\partial\tilde{u}}{\partial y}+\frac{\partial\tilde{v}}{\partial x}\Big), \qquad |\check{S}_{xz}| = \sqrt{\frac{1}{2}}\Big(\frac{\partial\tilde{u}}{\partial z}+\frac{\partial\tilde{w}}{\partial x}\Big), \qquad |\check{S}_{yz}| = \sqrt{\frac{1}{2}}\Big(\frac{\partial\tilde{v}}{\partial z}+\frac{\partial\tilde{w}}{\partial y}\Big). \tag{B.27}$$

(b) Subfilter kinetic energy one-equation model as

$$\nu_{\mathrm{t}} = C_\nu\sqrt{\tilde{k}}\Delta, \qquad \sigma_{kk} = -2\bar{\rho}\tilde{k}, \qquad C_\nu \approx 0.086 - 0.09. \tag{B.28}$$

- Heat flux term is modelled by an eddy-diffusivity model given by

$$\vartheta_x = -\check{C}_p\frac{\bar{\rho}\nu_{\mathrm{t}}}{\mathrm{Pr}_{\mathrm{t}}}\frac{\partial\tilde{T}}{\partial x}, \qquad \vartheta_y = -\check{C}_p\frac{\bar{\rho}\nu_{\mathrm{t}}}{\mathrm{Pr}_{\mathrm{t}}}\frac{\partial\tilde{T}}{\partial y}, \qquad \vartheta_z = -\check{C}_p\frac{\bar{\rho}\nu_{\mathrm{t}}}{\mathrm{Pr}_{\mathrm{t}}}\frac{\partial\tilde{T}}{\partial z}. \tag{B.29}$$

- Subfilter transport term for progress variable is modelled by gradient transport model as

$$\tilde{A}_x = -\frac{\bar{\rho}\nu_{\mathrm{t}}}{\mathrm{Sc}_{\mathrm{t}}}\frac{\partial\tilde{c}}{\partial x}, \qquad \tilde{A}_y = -\frac{\bar{\rho}\nu_{\mathrm{t}}}{\mathrm{Sc}_{\mathrm{t}}}\frac{\partial\tilde{c}}{\partial y}, \qquad \tilde{A}_z = -\frac{\bar{\rho}\nu_{\mathrm{t}}}{\mathrm{Sc}_{\mathrm{t}}}\frac{\partial\tilde{c}}{\partial z}. \tag{B.30}$$

- Subfilter transport term for flame surface density is modelled by gradient transport model as

$$\tilde{B}_x = \frac{\bar{\rho}\nu_{\mathrm{t}}}{\mathrm{Sc}_{\mathrm{t}}}\frac{\partial\tilde{\Sigma}}{\partial x}, \qquad \tilde{B}_y = \frac{\bar{\rho}\nu_{\mathrm{t}}}{\mathrm{Sc}_{\mathrm{t}}}\frac{\partial\tilde{\Sigma}}{\partial y}, \qquad \tilde{B}_z = \frac{\bar{\rho}\nu_{\mathrm{t}}}{\mathrm{Sc}_{\mathrm{t}}}\frac{\partial\tilde{\Sigma}}{\partial z}. \tag{B.31}$$

- Subfilter transport term for for subfilter kinetic energy is modelled by gradient transport model as

$$\tilde{C}_x = \bar{\rho}\Big(\frac{\nu_{\mathrm{t}}}{\mathrm{Pr}_{\mathrm{t}}}+\nu\Big)\frac{\partial\tilde{k}}{\partial x}, \qquad \tilde{C}_y = \bar{\rho}\Big(\frac{\nu_{\mathrm{t}}}{\mathrm{Pr}_{\mathrm{t}}}+\nu\Big)\frac{\partial\tilde{k}}{\partial y}, \qquad \tilde{C}_z = \bar{\rho}\Big(\frac{\nu_{\mathrm{t}}}{\mathrm{Pr}_{\mathrm{t}}}+\nu\Big)\frac{\partial\tilde{k}}{\partial z}. \tag{B.32}$$

- Source term of progress variable equation as

$$\bar{\dot{\omega}} = \rho_r s_{\mathrm{L}} \bar{\rho} \tilde{\Sigma}. \tag{B.33}$$

- The source terms appearing in flame surface density equation are as follows:
  (a) the mean strain term

$$\begin{aligned} \tilde{S}_{\Sigma 1x} &= (\delta_{xx} - n_{xx})\bar{\rho}\tilde{\Sigma}\frac{\partial \tilde{u}}{\partial x} + (\delta_{xy} - n_{xy})\bar{\rho}\tilde{\Sigma}\frac{\partial \tilde{u}}{\partial y} + (\delta_{xz} - n_{xz})\bar{\rho}\tilde{\Sigma}\frac{\partial \tilde{u}}{\partial z} \\ &= (1 - n_{xx})\bar{\rho}\tilde{\Sigma}\frac{\partial \tilde{u}}{\partial x} - n_{xy}\bar{\rho}\tilde{\Sigma}\frac{\partial \tilde{u}}{\partial y} - n_{xz}\bar{\rho}\tilde{\Sigma}\frac{\partial \tilde{u}}{\partial z}, \end{aligned} \tag{B.34}$$

$$\begin{aligned} \tilde{S}_{\Sigma 1y} &= (\delta_{xy} - n_{xy})\bar{\rho}\tilde{\Sigma}\frac{\partial \tilde{v}}{\partial x} + (\delta_{yy} - n_{yy})\bar{\rho}\tilde{\Sigma}\frac{\partial \tilde{v}}{\partial y} + (\delta_{xz} - n_{xz})\bar{\rho}\tilde{\Sigma}\frac{\partial \tilde{u}}{\partial z} \\ &= (1 - n_{yy})\bar{\rho}\tilde{\Sigma}\frac{\partial \tilde{v}}{\partial y} - n_{xy}\bar{\rho}\tilde{\Sigma}\frac{\partial \tilde{v}}{\partial x} - n_{xz}\bar{\rho}\tilde{\Sigma}\frac{\partial \tilde{v}}{\partial z}, \end{aligned} \tag{B.35}$$

$$\begin{aligned} \tilde{S}_{\Sigma 1z} &= (\delta_{xz} - n_{xz})\bar{\rho}\tilde{\Sigma}\frac{\partial \tilde{w}}{\partial x} + (\delta_{yz} - n_{yz})\bar{\rho}\tilde{\Sigma}\frac{\partial \tilde{w}}{\partial y} + (\delta_{zz} - n_{zz})\bar{\rho}\tilde{\Sigma}\frac{\partial \tilde{w}}{\partial z} \\ &= (1 - n_{zz})\bar{\rho}\tilde{\Sigma}\frac{\partial \tilde{w}}{\partial z} - n_{xz}\bar{\rho}\tilde{\Sigma}\frac{\partial \tilde{w}}{\partial x} - n_{yz}\bar{\rho}\tilde{\Sigma}\frac{\partial \tilde{w}}{\partial y}. \end{aligned} \tag{B.36}$$

  (b) the mean planar propagation term

$$\tilde{S}_{\Sigma 2} = -s_{\mathrm{L}}(1 + \tau\tilde{c})\big[N_x\frac{\partial(\bar{\rho}\tilde{\Sigma})}{\partial x} + N_y\frac{\partial(\bar{\rho}\tilde{\Sigma})}{\partial y} + N_z\frac{\partial(\bar{\rho}\tilde{\Sigma})}{\partial z}\big]. \tag{B.37}$$

  (c) the mean curvature term

$$\tilde{S}_{\Sigma 3} = -s_{\mathrm{L}}\bar{\rho}\tilde{\Sigma}\big[N_x\frac{\partial \tilde{c}}{\partial x} + N_y\frac{\partial \tilde{c}}{\partial y} + N_z\frac{\partial \tilde{c}}{\partial z}\big]. \tag{B.38}$$

  (d) the subfilter strain term

$$\tilde{S}_{\Sigma 4} = \Gamma_k\frac{\sqrt{\tilde{k}}}{\Delta}\bar{\rho}\tilde{\Sigma}. \tag{B.39}$$

  (e) the subfilter curvature term

$$\tilde{S}_{\Sigma 5} = -\beta s_{\mathrm{L}}\frac{(\bar{\rho}\tilde{\Sigma})^2}{1 - \tilde{c}}. \tag{B.40}$$

As

$$\mathrm{N} = -\frac{\nabla \bar{c}}{\bar{\rho}\tilde{\Sigma}}, \qquad n_{ij} = N_i N_j + \frac{1}{3}\alpha\delta_{ij}, \qquad \bar{c} = \frac{(1+\tau)\tilde{c}}{1+\tau\tilde{c}}, \tag{B.41}$$

we have

$$N_x = -\frac{1+\tau}{\bar{\rho}\tilde{\Sigma}(1+\tau\tilde{c})^2}\frac{\partial \tilde{c}}{\partial x}, \qquad N_y = -\frac{1+\tau}{\bar{\rho}\tilde{\Sigma}(1+\tau\tilde{c})^2}\frac{\partial \tilde{c}}{\partial y}, \qquad N_z = -\frac{1+\tau}{\bar{\rho}\tilde{\Sigma}(1+\tau\tilde{c})^2}\frac{\partial \tilde{c}}{\partial z}, \tag{B.42}$$

$$n_{xx} = \frac{1}{3}\alpha + \frac{(1+\tau)^2}{(\bar{\rho}\tilde{\Sigma})^2(1+\tau\tilde{c})^4}\frac{\partial^2 \tilde{c}}{\partial x^2}, \tag{B.43}$$

$$n_{yy} = \frac{1}{3}\alpha + \frac{(1+\tau)^2}{(\bar{\rho}\tilde{\Sigma})^2(1+\tau\tilde{c})^4}\frac{\partial^2 \tilde{c}}{\partial y^2}, \tag{B.44}$$

$$n_{zz} = \frac{1}{3}\alpha + \frac{(1+\tau)^2}{(\bar{\rho}\tilde{\Sigma})^2(1+\tau\tilde{c})^4}\frac{\partial^2 \tilde{c}}{\partial z^2}, \tag{B.45}$$

$$n_{xy} = \frac{(1+\tau)^2}{(\bar{\rho}\tilde{\Sigma})^2(1+\tau\tilde{c})^4}\frac{\partial \tilde{c}}{\partial x}\frac{\partial \tilde{c}}{\partial y}, \tag{B.46}$$

$$n_{xz} = \frac{(1+\tau)^2}{(\bar{\rho}\tilde{\Sigma})^2(1+\tau\tilde{c})^4}\frac{\partial \tilde{c}}{\partial x}\frac{\partial \tilde{c}}{\partial z}, \tag{B.47}$$

$$n_{yz} = \frac{(1+\tau)^2}{(\bar{\rho}\tilde{\Sigma})^2(1+\tau\tilde{c})^4}\frac{\partial \tilde{c}}{\partial y}\frac{\partial \tilde{c}}{\partial z}. \tag{B.48}$$

- The source term of subfilter kinetic energy equation is given by

$$\tilde{S}_k = -(\sigma_{xx}\tilde{S}_{xx} + \sigma_{yy}\tilde{S}_{yy} + \sigma_{zz}\tilde{S}_{zz} + \sigma_{xy}\tilde{S}_{xy} + \sigma_{xz}\tilde{S}_{xz} + \sigma_{yz}\tilde{S}_{yz}) - \bar{\rho}C_\epsilon\frac{\tilde{k}^{\frac{3}{2}}}{\Delta}. \tag{B.49}$$

Appendix C

Kolmogorov-Petrovski-Piskunov (KPP) Flame Speed Analysis

This chapter presents a simple theoretical tool to analyze turbulent combustion models. LES of turbulence is by nature three-dimensional due to the need to resolve turbulent structure. But if chosen the LES filter size larger than the flame brush thickness, the LES turbulence will have a one-dimensional character. The Kolmogorov-Petrovski-Piskunov (KPP) flame speed analysis for LES considers this situation. There are some other restrictions to the KPP analysis as well. It only applies to a steady frozen turbulence in which the turbulence kinetic energy remains constant. More details for KPP analysis may be found in Hakberg and Gosman [151], Fichot *et al.* [152] or Duclos *et al.* [112].

From progress variable and flame surface density transport equations, Eq. 3.50 and Eq. 3.60, considering a steady one-dimensional propagation in the negative x-direction at speed s_T in the fresh gases, one obtains:

$$\rho_\mathrm{r} s_\mathrm{T} \frac{\mathrm{d}\tilde{c}}{\mathrm{d}x} = \frac{\mathrm{d}}{\mathrm{d}x}\Big(\frac{\bar{\rho}\nu_\mathrm{t}}{\mathrm{Sc}_\mathrm{t}}\frac{\mathrm{d}\tilde{c}}{\mathrm{d}x}\Big) + \rho_\mathrm{r} s_\mathrm{L}\tilde{\Sigma}, \tag{C.1}$$

$$\begin{aligned}\frac{\rho_\mathrm{r} s_\mathrm{T}}{\bar{\rho}}\frac{\mathrm{d}\tilde{\Sigma}}{\mathrm{d}x} = {} & \frac{\mathrm{d}}{\mathrm{d}x}\Big(\frac{\bar{\rho}\nu_\mathrm{t}}{\mathrm{Sc}_\mathrm{t}}\frac{\mathrm{d}\tilde{\Sigma}}{\mathrm{d}x}\Big) + \Big(\frac{2}{3}\alpha - 1\Big)\frac{\mathrm{d}\tilde{u}}{\mathrm{d}x}\tilde{\Sigma} \\ & - \frac{\mathrm{d}}{\mathrm{d}x}(s_\mathrm{L}(1+\tau\tilde{c})N\tilde{\Sigma}) + s_\mathrm{L}(1+\tau\tilde{c})\frac{\mathrm{d}N}{\mathrm{d}x}\tilde{\Sigma} \\ & + \mathrm{S}_\mathrm{sfs}\tilde{\Sigma} - \alpha\beta s_\mathrm{L}\frac{\tilde{\Sigma}^2}{1-\tilde{c}}.\end{aligned} \tag{C.2}$$

Using the expression for the density $\bar{\rho} = \rho_\mathrm{r}/(1+\tau\tilde{c})$, assuming constant eddy diffusivities, it may be shown that

$$\frac{\mathrm{d}}{\mathrm{d}x}\Big(\frac{\bar{\rho}\nu_\mathrm{t}}{\mathrm{Sc}_\mathrm{t}}\frac{\mathrm{d}\tilde{c}}{\mathrm{d}x}\Big) = \frac{\bar{\rho}\nu_\mathrm{t}}{\mathrm{Sc}_\mathrm{t}}\frac{\mathrm{d}^2\tilde{c}}{\mathrm{d}x^2} + \frac{\bar{\rho}\nu_\mathrm{t}}{\mathrm{Sc}_\mathrm{t}}\frac{\tau}{1+\tau\tilde{c}}\Big(\frac{\mathrm{d}\tilde{c}}{\mathrm{d}x}\Big)^2, \tag{C.3}$$

$$\begin{aligned}\frac{\mathrm{d}}{\mathrm{d}x}\Big(\frac{\bar{\rho}\nu_\mathrm{t}}{\mathrm{Sc_t}}\frac{\mathrm{d}\tilde{\Sigma}}{\mathrm{d}x}\Big) &= \frac{\bar{\rho}\nu_\mathrm{t}}{\mathrm{Sc_t}}\frac{\mathrm{d}^2\tilde{\Sigma}}{\mathrm{d}x^2} - \frac{\bar{\rho}\nu_\mathrm{t}}{\mathrm{Sc_t}}\frac{\mathrm{d}}{\mathrm{d}x}\Big(\frac{\tau\tilde{\Sigma}}{1+\tau\tilde{c}}\frac{\mathrm{d}\tilde{c}}{\mathrm{d}x}\Big) \\ &= \frac{\bar{\rho}\nu_\mathrm{t}}{\mathrm{Sc_t}}\frac{\mathrm{d}^2\tilde{\Sigma}}{\mathrm{d}x^2} - \frac{\bar{\rho}\nu_\mathrm{t}}{\mathrm{Sc_t}}\frac{\tau}{1+\tau\tilde{c}}\Big[\frac{\tau\tilde{\Sigma}}{1+\tau\tilde{c}}\Big(\frac{\mathrm{d}\tilde{c}}{\mathrm{d}x}\Big)^2 + \frac{\mathrm{d}\tilde{c}}{\mathrm{d}x}\frac{\mathrm{d}\tilde{\Sigma}}{\mathrm{d}x} + \Sigma\frac{\mathrm{d}^2\tilde{c}}{\mathrm{d}x^2}\Big]. \quad \text{(C.4)}\end{aligned}$$

The propagation terms may be simplified for the case of constant s_L as follows:

$$-\frac{\mathrm{d}}{\mathrm{d}x}(s_\mathrm{L}(1+\tau\tilde{c})N\tilde{\Sigma}) + s_\mathrm{L}\tilde{\Sigma}(1+\tau\tilde{c})\frac{\mathrm{d}N}{\mathrm{d}x} = -s_\mathrm{L}N(1+\tau\tilde{c})\frac{\mathrm{d}\tilde{\Sigma}}{\mathrm{d}x} - \tau s_\mathrm{L}N\tilde{\Sigma}\frac{\mathrm{d}\tilde{c}}{\mathrm{d}x}. \quad \text{(C.5)}$$

Assuming a steady flow, the continuity gives $\tilde{u} = \rho_\mathrm{r}s_\mathrm{T}/\bar{\rho}$, then we have

$$\frac{\mathrm{d}\tilde{u}}{\mathrm{d}x} = \frac{\mathrm{d}(1+\tau\tilde{c})s_\mathrm{T}}{\mathrm{d}x} = \tau s_\mathrm{T}\frac{\mathrm{d}\tilde{c}}{\mathrm{d}x}. \quad \text{(C.6)}$$

Now, following the approach of Hakberg and Gosman [151], let

$$P = \frac{\mathrm{d}\tilde{c}}{\mathrm{d}x}, \quad \text{(C.7)}$$

and

$$Q = \frac{\mathrm{d}\tilde{\Sigma}}{\mathrm{d}x}, \quad \text{(C.8)}$$

and it can be shown that

$$s_\mathrm{T}(1+\tau\tilde{c})P = \frac{\nu_\mathrm{t}}{\mathrm{Sc_t}}P\frac{\mathrm{d}P}{\mathrm{d}\tilde{c}} + \frac{\nu_\mathrm{t}}{\mathrm{Sc_t}}\frac{\tau}{(1+\tau\tilde{c})}P^2 + s_\mathrm{L}(1+\tau\tilde{c})\tilde{\Sigma}, \quad \text{(C.9)}$$

$$\begin{aligned}s_\mathrm{T}(1+\tau\tilde{c})Q &= \frac{\nu_\mathrm{t}}{\mathrm{Sc_t}}Q\frac{\mathrm{d}Q}{\mathrm{d}\tilde{\Sigma}} + \mathrm{S_{sfs}}\tilde{\Sigma} \\ &\quad -\frac{\nu_\mathrm{t}}{\mathrm{Sc_t}}\frac{\tau}{(1+\tau\tilde{c})}\Big(\frac{\tau}{1+\tau\tilde{c}}P^2\tilde{\Sigma} + PQ + P\frac{\mathrm{d}P}{\mathrm{d}\tilde{c}}\tilde{\Sigma}\Big) \\ &\quad +\Big(\frac{2}{3}\alpha - 1\Big)s_\mathrm{T}\tau P\tilde{\Sigma} - \alpha\beta s_\mathrm{L}\frac{\tilde{\Sigma}^2}{1-\tilde{c}} \\ &\quad -s_\mathrm{L}(1+\tau\tilde{c})NQ - \tau s_\mathrm{L}N\tilde{\Sigma}P. \quad \text{(C.10)}\end{aligned}$$

In the fresh gases, $\tilde{\Sigma}, \tilde{c}, \frac{\mathrm{d}\tilde{c}}{\mathrm{d}x}$, and $\frac{\mathrm{d}\tilde{\Sigma}}{\mathrm{d}x}$ are all small. The variables $\tilde{\Sigma}, P$, and Q are extended as functions of $\tilde{c}$ and $\tilde{\Sigma}$ as follows:

$$P = a_1\tilde{c} + a_2\tilde{c}^2 + \cdots, \quad \text{(C.11)}$$

$$Q = b_1\tilde{\Sigma} + b_2\tilde{\Sigma}^2 + \cdots, \quad \text{(C.12)}$$

$$\tilde{\Sigma} = d_1\tilde{c} + d_2\tilde{c}^2 + \cdots. \quad \text{(C.13)}$$

In the limit of small c and $\tilde{\Sigma}$, second and higher order terms may be neglected. Eq. C.9 and Eq. C.10 become

$$s_\mathrm{T}a_1\tilde{c} = \frac{\nu_\mathrm{t}}{\mathrm{Sc_t}}a_1^2\tilde{c} + s_\mathrm{L}d_1\tilde{c}, \quad \text{(C.14)}$$

$$(s_\mathrm{T} + Ns_\mathrm{L})b_1\tilde{\Sigma} = \frac{\nu_\mathrm{t}}{\mathrm{Sc_t}}b_1^2\tilde{\Sigma} + \mathrm{S_{sfs}}\tilde{\Sigma}. \quad \text{(C.15)}$$

For there to be real solutions for b_1, s_T must obey

$$s_\mathrm{T} \geq -N s_\mathrm{L} + 2\sqrt{\frac{\mathrm{S_{sfs}}}{\nu_\mathrm{t}\mathrm{Sc_t}}}. \tag{C.16}$$

The KPP theorem indicates that the flame propagation speed corresponds to the minimum solution for s_T (Hakberg and Gosman [151]), therefore

$$s_\mathrm{T} = -N s_\mathrm{L} + 2\sqrt{\frac{\mathrm{S_{sfs}}}{\nu_\mathrm{t}\mathrm{Sc_t}}}. \tag{C.17}$$